

The design and simulation of a new experimental set up to measure nuclear level lifetimes



Bhivek Singh

Faculty of Natural Sciences

Department of Physics & Astronomy

University of the Western Cape

A thesis submitted in partial fulfillment for the degree of

Master of Science

2016

Declaration

I declare that THE DESIGN AND SIMULATION OF A NEW EXPERIMENTAL SET UP TO MEASURE NUCLEAR LEVEL LIFETIMES is my own work, that it has not been submitted for any degree or examination in any other university, and that all sources I have used or quoted have been indicated and acknowledged by complete references.



Bhivek Singh

August 2016

Signature:

Acknowledgements

I am truly grateful to all who assisted me in the completion of this work. I would especially like to thank my supervisor Smarajit Triambak who provided me with this wonderful opportunity to take part in an amazing and unique project and who provided untold support and motivation, and also my co-supervisor Nico Orce for his excellent advice and motivational talks. I am particularly grateful for the many hours they have put into improving both this thesis and my abilities in general. A special thanks to Bernadette Rebeiro, Johannes Broodryk, Zaid Dyers, and Rob McAllister for all their help and advice during the project.

I must also thank Angela Adams and Shirese Spannenberg at the Department of Physics and Astronomy at the University of the Western Cape, without whom work in the department would be impossible.

I would also like to thank all my past teachers, coaches, classmates and colleagues, especially Vage Evetts, Dantin Broodryk and Karen Uys for setting an excellent standard to live up to.

Lastly, I would like thank the National Research Foundation of South Africa for all the financial support they provided during the course of my studies.

Abstract

Measurements of nuclear level lifetimes are an important aspect of experimental nuclear physics. Such measurements determine transition matrix elements for nuclear structure research and also provide the widths of relevant excited states in nuclei that are of astrophysical interest. In the latter, the measured widths are used to obtain reaction rates in main sequence stars such as the Sun and in binary-star systems where the accretion of material from one star to another provides an opportunity to study extreme stellar environments such as novae and x-ray bursts.

This thesis work describes the design and simulation of a new experimental set up at iThemba LABS that will allow for high-precision femtosecond-level lifetime measurements of nuclear states using the Doppler Shift Attenuation Method (DSAM). We use the Solid Edge computer-aided design (CAD) software to design a new scattering chamber with a cooled target ladder specifically for such measurements using inverse-kinematic transfer reactions with ion implanted targets. The light charged ejectiles from the reaction will be detected with a $\Delta E - E$ silicon telescope, while Doppler shifted γ rays will be registered using a high-purity and 100% efficient germanium (HPGe) detector. We also describe preliminary Monte Carlo simulation codes that are being developed

in a relativistically invariant framework to optimize the experimental set up and to obtain predicted lineshapes of γ rays from several astrophysically relevant states in nuclei using this experimental set up.



Contents

1	Introduction	1
2	Nuclear Lifetimes I - Nuclear Structure	4
2.1	Introduction	4
2.1.1	The Strong Force	5
2.1.2	The Nuclear Shell Model	8
2.1.3	Deformation in Nuclei	12
2.2	Multipole Moments for a Charge Distribution	18
2.3	Fermi's Golden Rule	23
2.4	The Relation Between Lifetime Measurements and Coulomb Excitation	27
3	Nuclear Lifetimes II - Astrophysics	32
3.1	Introduction	32
3.1.1	Life Cycles of Stars	32
3.1.2	Equilibrium Conditions in the Stellar Interior	36
3.1.3	Nuclear Reactions	39
3.2	Reaction Rates	39
3.3	Resonances	44
3.3.1	Astrophysical S-factor	48

3.4	Hydrogen Burning	51
3.4.1	PP-chains	51
3.4.2	CNO cycles	53
3.5	The $^{14}\text{N}(p, \gamma)^{15}\text{O}$ Reaction	55
3.6	Direct Nuclear Reactions	58
3.6.1	Scattering Theory	59
3.6.2	Born approximation	61
3.6.3	Partial Waves	63
3.6.4	Direct Nuclear Reactions for Experiments	65
4	Apparatus and Design Specifications	67
4.1	Techniques	69
4.1.1	Fast Electronic Timing	69
4.1.2	Recoil Distance Doppler Shift	69
4.1.3	Doppler Shift Attenuation Method	71
4.2	Design specifications	72
4.2.1	Vacuum System	73
4.2.2	Pumps and Gauges	75
4.2.3	Target Holder and Cooling Arrangement	76
4.2.4	Target Heating	77
4.2.5	Beam Tuning	78
5	Monte Carlo Simulations	80
5.1	Monte Carlo Methods	81
5.2	Simulations for $^3\text{He}(^{16}\text{O}, ^{15}\text{O})^4\text{He}$	83
5.2.1	Reaction Kinematics	83
5.2.2	DSAM Lineshape Code for $^3\text{He}(^{16}\text{O}, ^{15}\text{O})^4\text{He}$	88
	The use of randomized variables in the simulations	89

5.2.3	Geant4 Simulations	97
	Structure of a Geant4 Application	97
5.2.4	Lineshape and Efficiency Determination from Geant4	99
	Results	104
	Efficiencies	115
6	Conclusions	119
A	Cross sections	120
A.1	Scattering Theory	120
A.2	Resonant Scattering	122
B	Cubic Splines	125
C	Relativistic Kinematics Code	127
D	Monte Carlo Doppler Shift Code	143
E	The Primary Action Generator from the Geant Code	148
	Bibliography	155

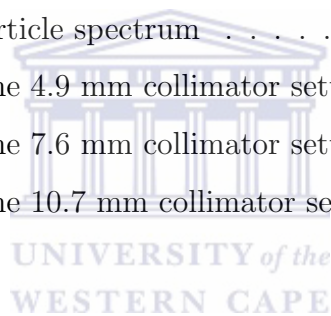


List of Figures

2.1	Graph of binding energy per nucleon	6
2.2	Single ionization energies for various elements	8
2.3	Charge densities for various nuclei	9
2.4	Diagram showing the effects of adding the spin orbit interaction	11
2.5	Nuclear shapes described by different deformation parameters.	13
2.6	Graphic representation of the different projections of angular momentum.	14
2.7	Nilsson diagram shows the effect of deformation	17
2.8	An arbitrary continuous charge distribution	19
2.9	Plot of the transition matrix element as a function of the di- agonal matrix element	31
3.1	A Hertzsprung-Russell diagram	35
3.2	The Gamow window	50
3.3	The CNO cycle	54
3.4	R-matrix fit	56
3.5	^{15}O level scheme	57
3.6	Plane wave scattering	60
4.1	Floor plan of iThemba LABS	68
4.2	The separated sector cyclotron (SSC) from above.	68

4.3	Schematic of the Recoil Distance Doppler Shift method	70
4.4	Schematic of a DSAM experiment	71
4.5	Full design done in Solid Edge (ST6)	74
4.6	Close up view of the design	76
4.7	Heat transfer simulation performed in Solid Edge.	78
5.1	Gaussian probability density function	82
5.2	The sum of the momenta in the centre of mass frame is always 0, which greatly simplifies analysis.	84
5.3	Schematic of the DSAM set up	89
5.4	Outline of the flow through the Monte Carlo code.	92
5.5	The effects of introducing a collimator (setting $\theta_{\alpha max} = 8^\circ$) on lineshape. A clearly asymmetric peak arises on using a collimator.	93
5.6	The effect of detector distance on lineshape.	95
5.7	Effect of detector angle on line shape	96
5.8	General outline of the flow through the Geant code while the simulation runs.	99
5.9	Visualization of the detector set up in the Geant code. The beam is assumed to be in the $+\hat{z}$ direction.	101
5.10	Ion ranges for a 40 keV ^3He beam on a Au target.	102
5.11	The effects of different collimator sizes for a germanium de- tector placed 85 mm from the target	105
5.12	Photopeaks from the individual spectra in figure 5.11	106
5.13	The effects of different collimator sizes for a germanium de- tector placed 145 mm from the target	107
5.14	Photopeaks from the individual spectra in figure 5.13	108

5.15	The effects of moving the germanium detector to different distances	109
5.16	Photopeaks from the individual spectra in figure 5.15	110
5.17	The effects of moving the germanium detector to different distances	111
5.18	Photopeaks from the individual spectra in figure 5.17	112
5.19	Spectra from the $\Delta E - E$ detector for different collimators. . .	113
5.20	Comparison between a raw γ spectrum and one obtained by gating on the particle spectrum	114
5.21	Comparison between a raw γ spectrum and one obtained by gating on the particle spectrum	114
5.22	Efficiencies for the 4.9 mm collimator setting	117
5.23	Efficiencies for the 7.6 mm collimator setting	117
5.24	Efficiencies for the 10.7 mm collimator setting	118



Chapter 1

Introduction

Measurements of nuclear level lifetimes play an important role in experimental nuclear physics research. In studies of nuclear structure, measured lifetimes can be used to determine transition matrix elements and provide useful information to test nuclear models, make inferences about nuclear shapes and for other studies of collective excitation modes in nuclei [1, 2].

Lifetime measurements are also relevant for studies in nuclear astrophysics. Such measurements provide experimental widths of resonance reactions that are related to reaction rates in stars via the astrophysical S -factor. This is important for studies of reaction rates in main sequence stars such as the Sun as well as explosive events such as classical novae. In the former, energy generation is a result of fusion reactions in stellar cores. In such stellar environments, the pp-chains and cold CNO-cycle are important for the quiescent burning that occurs over long periods of time; while the hot CNO-cycle, occurring mainly in giant helium burning stars, is an important precursor to the explosive burning in novae and X-ray bursts [3]. These explosive phenomena are a result of runaway burning processes near the end of a star's life and are responsible for both creating the heavy elements (iron

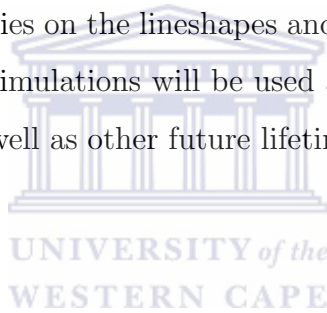
and beyond) and dispersing reaction products in the universe. Break-out reactions from the hot CNO-cycle are believed to lead to the rp-process where β^+ -decays and (p, γ) reactions compete to form reaction networks that take the seed nuclei from the CNO-cycle up into the closed SnSbTe cycle [3]. The specifics of these networks are not very well known and are still an active area of research. Here lifetime measurements can offer important information for characterizing many reactions in these networks.

This thesis relates to the cold CNO-cycle, where the $^{14}\text{N}(p, \gamma)$ reaction forms a bottleneck and affects the overall rate of energy production in the main sequence. This reaction rate is the least well known of the entire cycle and direct measurements of the reaction rate prove challenging due to low cross sections and high background rates at thermal energies. Lifetime measurements of excited states in ^{15}O could remedy this situation by allowing an indirect measurement using an R-matrix fit [4, 5].

The $^{14}\text{N}(p, \gamma)$ reaction rate is affected by a broad subthreshold resonance caused by a $\frac{3}{2}^+$ excited state in ^{15}O at 6.79 MeV, which has a lifetime < 1.8 fs [6]. There have been several attempts to measure the lifetime of this state [6, 7, 8, 9], out of which the only conclusive direct measurement of $1.60^{+0.75}_{-0.72}$ fs was carried out by Bertone *et al.* [8]. The other measurements agree poorly or have only placed limits on the lifetime of this state. Bertone *et al.* made their measurement at a low beam energy of 300 keV in direct kinematics using the Doppler Shift Attenuation Method. This beam energy leads to low recoil energies in the range where the stopping powers are not very well known.

The main aim of this project is to design and simulate an experimental set up capable of making lifetime measurements down to the 1 fs level with maximal sensitivity to lineshapes. In an anticipated future experiment, excited

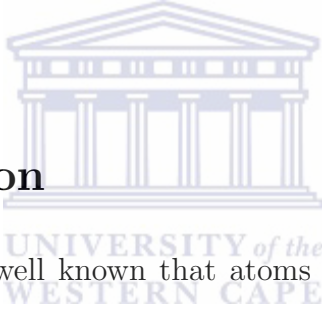
states in ^{15}O will be produced with the $^{16}\text{O}(^3\text{He}, \alpha)$ transfer reaction in inverse kinematics using a ^3He implanted target. This will allow us to measure the lifetime of interest in ^{15}O using the Doppler Shift Attenuation Method with the lineshape analysis technique and with minimal uncertainties from known stopping powers. To do this, the full set up of a high vacuum scattering chamber was designed using the Solid Edge computer aided design (CAD) software package. Particular attention was paid to the cryogenics of the vacuum system and beam tuning. We also developed a computer program using the Geant4 toolkit to simulate the lineshapes and γ -ray efficiencies. Data from these simulations were used to investigate the effects of different detector geometries on the lineshapes and efficiencies and helped to refine the design. These simulations will be used as a guide to plan the ^{15}O lifetime measurement as well as other future lifetime measurements that use the same method.



Chapter 2

Nuclear Lifetimes I - Nuclear Structure

2.1 Introduction



By the year 1910 it was well known that atoms are the basic constituents of bulk materials. What was still open to investigation and not well understood then was the internal structure of the atom. At the time of Ernest Rutherford's famous gold leaf experiment [10, 11] the proposed model for the atom was Thomson's plum pudding model, which was based on the idea that the electrons of an atom floated around in a sea of positive charge almost like the raisins in a plum pudding. By firing α particles at a thin gold foil, Rutherford, Geiger and Marsden discovered that while most of the α particles went straight through the foil, a small percentage of the α particles would be scattered off the foil at extreme angles (greater than 90 degrees with respect to the beam axis). From this experiment Rutherford concluded that the plum pudding model was wrong. He postulated that the positive charge in an atom is highly concentrated in a region far smaller than the atom itself

(called the nucleus), and that almost all the mass of an atom resides in the nucleus. This discovery marked the beginning of nuclear physics as a field of research.

2.1.1 The Strong Force

The discovery of the atomic nucleus prompted further investigation into what its constituents might be. Thomson had already discovered the existence of isotopes with the use of his mass spectrometer. Rutherford's later discovery of the proton and Chadwick's discovery of the neutron raised new questions. At the time it was thought that only two fundamental forces existed in nature; gravity and electromagnetism. If this was true, nuclei containing more than one proton should not exist, as the Coulomb repulsion would drive them apart. Clearly, a previously unknown force must exist that is significantly stronger than the electromagnetic force and is short ranged, so that it binds the protons and neutrons in nuclei. This is now known to be the strong force, which confines nucleons (protons and neutrons) inside a potential well much the same way as the Coulomb interaction binds electrons inside atoms. Solutions to the Schrödinger equation for this many-body system results in the emergence of discrete states in nuclei, with particular energy spacings. It should be noted here that even after more than 100 years of study of nuclear physics, the strong force is still not well understood.

The depth of the potential well is a measure of the binding energy, denoted B , of the nucleus. The binding energy can be obtained from the mass deficit with the well known formula

$$(Zm_p + Nm_n) - M = \frac{B}{c^2}, \quad (2.1)$$

where M is the nuclear mass, Z is the number of protons, N is the number

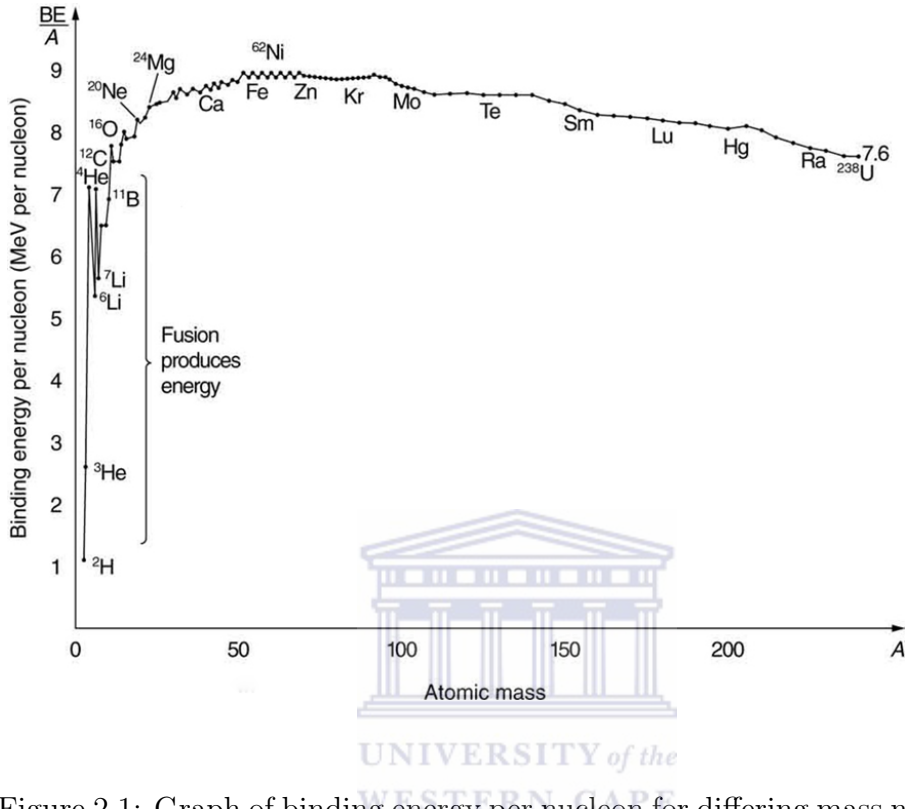


Figure 2.1: Graph of binding energy per nucleon for differing mass number A .

of neutrons, m_p is the mass of a free proton and m_n is the mass of a free neutron. An often used quantity is the binding energy per nucleon ($\frac{B}{A}$), which is a gross measure of the energy required to remove one nucleon from a nucleus. Figure 2.1 shows a plot of $\frac{B}{A}$ against the mass number A . The graph shows a rapid rise in $\frac{B}{A}$ at low mass ($A < 20$) after which it begins to flatten out, peaking at about 9 MeV per nucleon in the region of ^{56}Fe and ^{62}Ni , and dropping steadily at higher masses ($A > 100$). The flattening of the curve in the region between $A \approx 40$ and $A \approx 100$ can be understood as a result of the short range of the strong force and the fact that nuclear matter is incompressible. Similarly, the drop at higher masses can be explained due to the effect of Coulomb repulsion between protons.

The curve shown in figure 2.1 can be described by a semi-empirical mass formula, which was developed by assuming the atomic nucleus to be similar to a liquid drop of an incompressible fluid. Thereby, in the model the nuclear binding energy was proportional to the volume of the nucleus and, by implication, the mass number A . Other corrections corresponding to different phenomenological effects need to be added to the ‘volume term’ so that the features of figure 2.1 can be described adequately [12],

$$B = a_{vol}A - a_{surf}A^{\frac{2}{3}} - \frac{1}{2}a_{sym}\frac{(N - Z)^2}{A} - a_cZ(Z - 1)A^{-\frac{1}{3}} + \delta. \quad (2.2)$$

In the above, the second term is due to the fact that nucleons on the surface are less bound as they have fewer neighbours. The next term, called the symmetry term, is particularly relevant for light nuclei. This term arises from Pauli’s exclusion principle for fermions and accounts for the fact that light nuclei along the $N = Z$ line are more stable. Eventually, at higher masses the Coulomb repulsion between protons begins to dominate. The fourth term represents the energy associated with the Coulomb repulsion; this term favours neutron rich nuclei and in competition with the symmetry term reproduces the trend that heavier stable nuclei are neutron rich. Last is the pairing term which vanishes for odd A nuclei and accounts for the fact that even-even nuclei have a higher binding energy than odd-odd nuclei.

The semi-empirical mass formula does well to reproduce the binding energy per nucleon curve, but gives little information of the internal structure of the nucleus. Several sophisticated nuclear models have been developed since the semi-empirical mass formula was first proposed. I discuss two of the most important and fundamental models below.

2.1.2 The Nuclear Shell Model

The shell model was developed in the study of atoms, after it was noticed that certain electronic configurations are particularly stable (the noble gases). This is made apparent by plotting the single ionisation energies of various elements as function of atomic number, which clearly shows various peaks (*c.f.* figure 2.2). These tightly bound configurations were labeled with the so called “magic numbers”. The phenomenon was explained in the context of the occurrence of various shells of electron orbitals, with explicit shell gaps. Later on, the study of nuclei revealed a similar phenomenon of magic numbers in nuclei corresponding to peaks in proton and neutron separation energies.

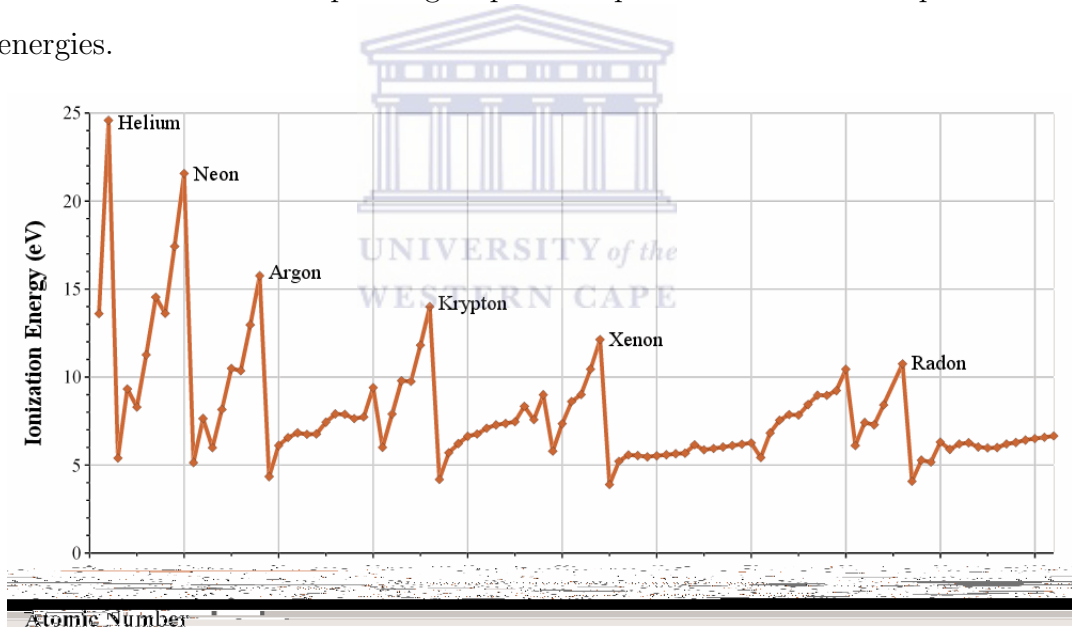


Figure 2.2: Single ionization energies for various elements. Note the peaks at each noble gas [13].

For studies of nuclear structure along similar lines the nuclear shell model is introduced. Since the exact form of the potential is not known (unlike the Coulomb potential in atomic physics), it is essential that one acquires a rea-

sonable first approximation of the residual strong interaction potential that binds the nucleons. It is known that the nucleus is not a point object, and has a finite size and distribution of charge and mass. Studies of isobaric nuclei and low energy nucleon-nucleon scattering experiments also suggest that the strong interaction binds nucleons with similar strength independent of their electric charge [14]. Further, experimental data from electron scattering show that the nuclear density distribution appears to be roughly constant throughout its volume and that nuclei do not have sharp boundaries. Instead, as shown in figure 2.3, the nuclear surface appears diffuse.

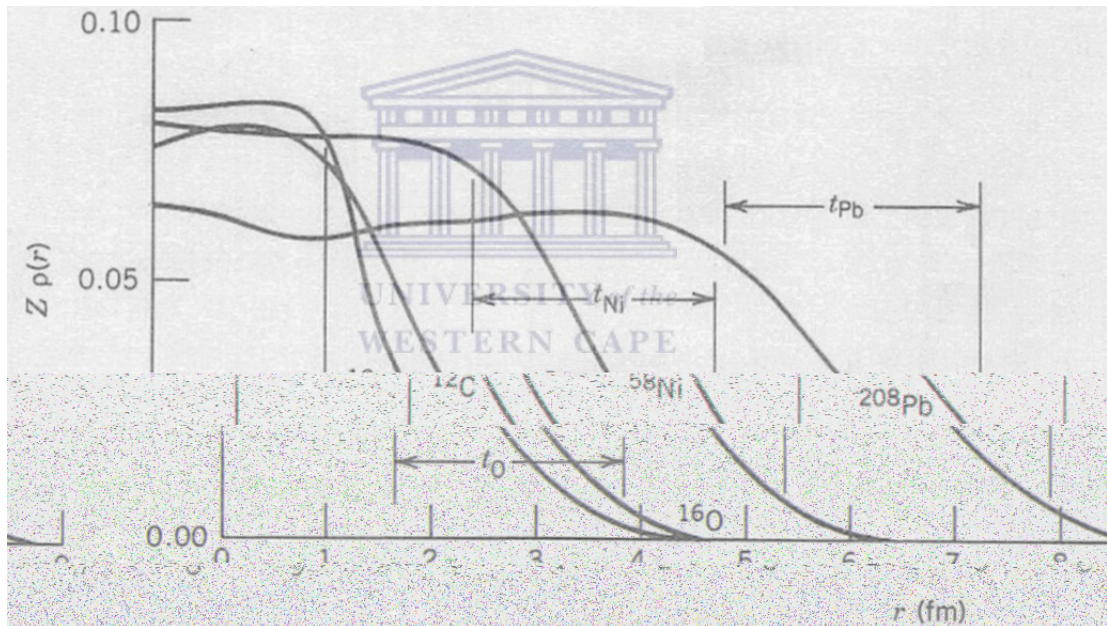


Figure 2.3: Charge densities for various nuclei as a function of radius, obtained from various electron scattering experiments [15].

All of the above indicates a short-ranged nuclear potential which is similar in shape for all nuclei. Based on the observed charge density distributions from electron scattering experiments, a commonly used guess for the nuclear

potential is the spherically symmetric Woods-Saxon potential [12],

$$V(r) = \frac{-V_0}{1 - e^{(r-R)/a}}, \quad (2.3)$$

where V_0 is an estimate of the depth of the well, R is an estimate of the nuclear radius, and a is the diffuseness parameter which is related to the skin depth t in figure 2.3. Unfortunately the Schrödinger equation for the Woods-Saxon potential can not be solved analytically. The potential, however, has a useful approximation between two potentials that do have analytical solutions; the harmonic oscillator and the finite square well. As an alternative, one could also use a 3-dimensional harmonic oscillator potential,



$$V(r) = \frac{1}{2}M\omega^2\mathbf{r}^2, \quad (2.4)$$

and add various modifications. The harmonic oscillator potential by itself produces degenerate solutions due to rotational symmetry in three dimensions. For example, the second $\ell = 0$ state and the first $\ell = 2$ state are degenerate, and so on [12]. For this reason, an ℓ^2 term is added to the single particle Hamiltonian in order to break the degeneracy of the s, p, d -states etc. in the three dimensional isotropic harmonic oscillator problem,

$$\hat{H} = \underbrace{\frac{-\hbar^2}{2M}\nabla^2 + \frac{1}{2}M\omega^2\mathbf{r}}_{H_0} + D\ell^2, \quad (2.5)$$

with $D < 0$. This term has the effect of displacing the ℓ states slightly so that they are separated and the high- ℓ states lie below the low- ℓ states [14]. Nonetheless, the potentials of Eqs. (2.3) and (2.4) by themselves do not reproduce the experimentally observed magic numbers and shell gaps. The solution to the problem is in the spin-orbit coupling as suggested by Goepfert-

Mayer, Jensen and others [14]. The interaction is known to be

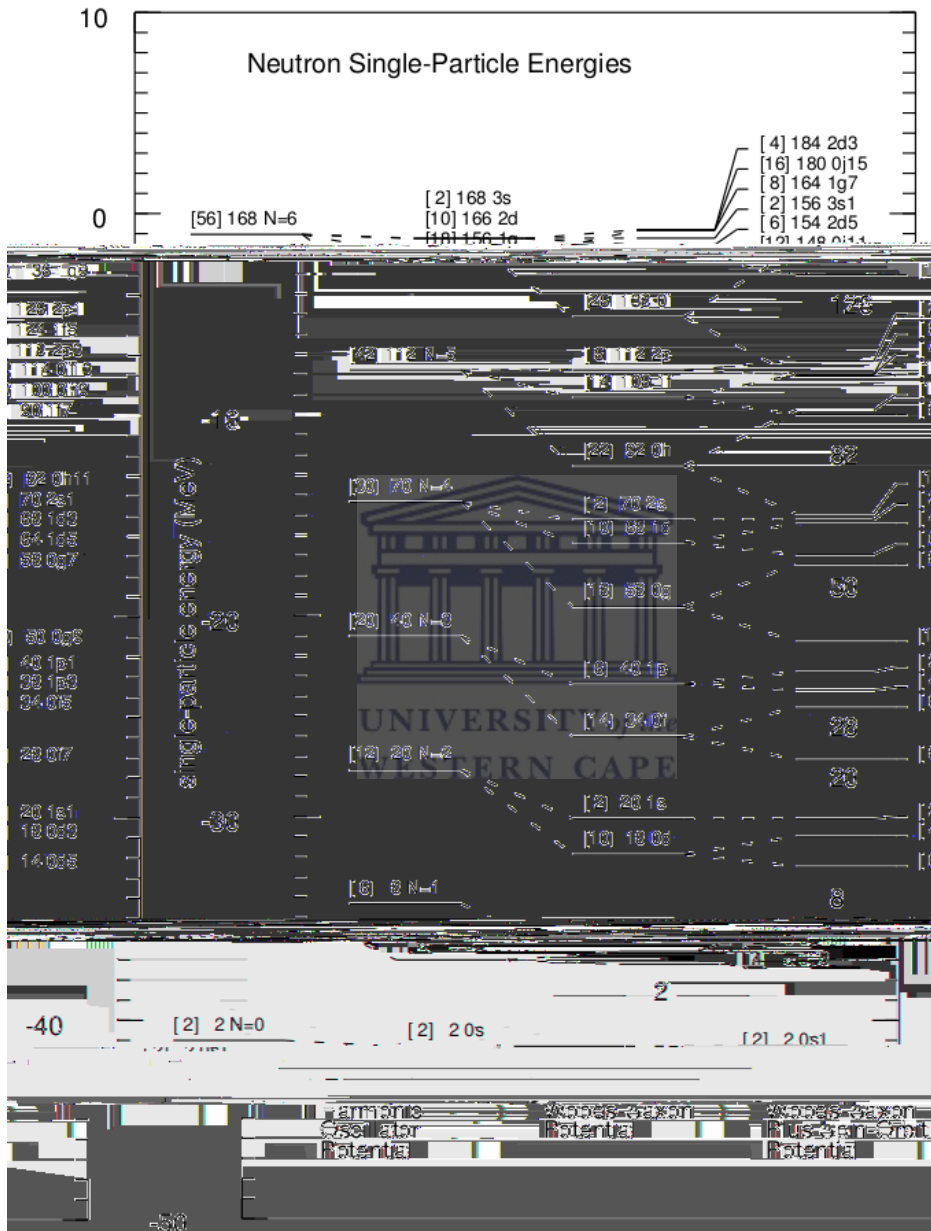


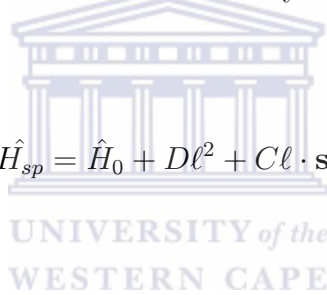
Figure 2.4: Diagram showing the effects of adding the spin orbit interaction to a potential. In this case the spin orbit term is added to the Woods-Saxon, but the effect remains a splitting of the states with $l > 0$ [16].

$$\langle \ell \cdot \mathbf{s} \rangle = \langle \frac{1}{2}(\mathbf{j}^2 - \ell^2 - \mathbf{s}^2) \rangle, \quad (2.6)$$

which has no effect on the $\ell = 0$ states, but splits higher ℓ states depending on whether the spin is aligned parallel or anti-parallel to the orbital angular momentum. The magnitude of the splitting is proportional to $(2\ell + 1)$ and increases with ℓ . As shown in figure 2.4, once the spin-orbit term is introduced, the experimental shell gaps and magic numbers are reproduced exactly up to $N = 126$. The inclusion of this term to the Hamiltonian in Eq. (2.5) yields a Hamiltonian that is usually used in the spherical shell model,

$$\hat{H}_{sp} = \hat{H}_0 + D\ell^2 + C\ell \cdot \mathbf{s}, \quad (2.7)$$

with $C < 0$.



2.1.3 Deformation in Nuclei

The spherical shell model predicts the magic numbers and ground state spins and parities in most nuclei quite well. It also does a good job at reproducing the single particle excitation energies for nuclei that have a magic number of either protons or neutrons, and particularly those with magic numbers for both (doubly magic nuclei). However, when looking at nuclei far from closed shells, where large deviations from spherical symmetry are expected in the potential, one has to look beyond the spherical shell model.

In general, the radial distance of a deformed nuclear surface can be de-

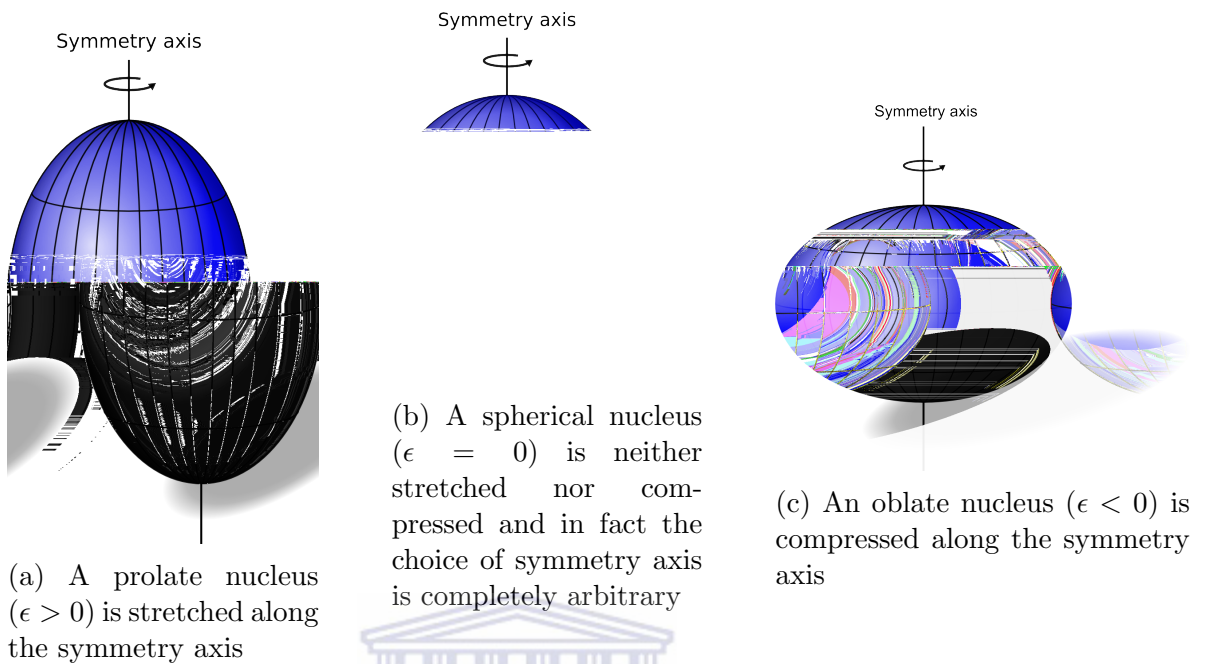


Figure 2.5: Nuclear shapes described by different deformation parameters.

scribed as an expansion in terms of the spherical harmonics

$$R(\theta, \phi) = R_0 \left[1 + \sum_{\lambda} \sum_{\mu} a_{\lambda\mu} Y_{\lambda\mu} \right] \quad (2.8)$$

where the time dependent coefficients $a_{\lambda\mu}$ represent the collective ‘co-ordinates’, and R_0 is the radius of a sphere of equivalent volume. The lowest order term of importance in the above is the quadrupole term. This is used in a generalized phenomenological shell model, called the Nilsson model which allows for the lowest order deformed spheroidal potentials shown in figure 2.5. Within the deformed shell model, the Hamiltonian is modified to be axially symmetric, with an additional deformation parameter ϵ so that

$$\hat{H}(\epsilon) = \hat{H}_0(\epsilon) + Cl \cdot \mathbf{s} + D\ell^2, \quad (2.9)$$

where,

$$\hat{H}_0(\epsilon) = -\frac{\hbar^2}{2M}\nabla^2 + \frac{1}{2}M\omega_0^2(\epsilon)[(x^2 + y^2)(1 + \frac{1}{3}\epsilon)^2 + z^2(1 - \frac{2}{3}\epsilon)^2]. \quad (2.10)$$

Importantly the oscillator frequency becomes a function of the deformation parameter in such a way that the volume of the nucleus is independent of the deformation. This means the following condition must be imposed [17]

$$\omega_x\omega_y\omega_z = \text{const.} \quad (2.11)$$

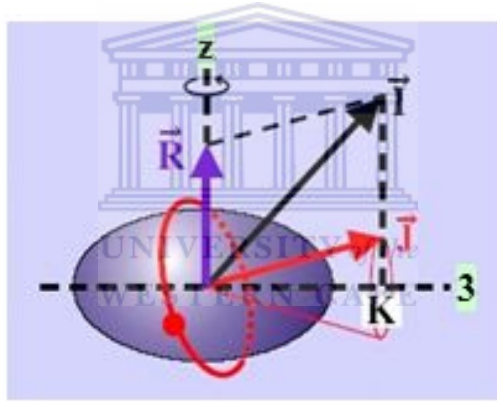


Figure 2.6: Graphic representation of the different projections of angular momentum.

An important consequence of the deformed shape of the nucleus is that we can now talk about spatial orientation for single particle wave functions. However, they can not have a fixed orientation in space and are forced to precess. The interpretation of this is that the single particle wave functions, having aligned with each other along the symmetry axis, now begin to precess around an axis perpendicular to the symmetry axis and so the nucleus

appears to spin. This means that the intrinsic total angular momentum is no longer a good quantum number, but can be coupled with the angular momentum arising from the collective motion to produce a total angular momentum that is a good quantum number as shown in figure 2.6 [17]. The rotation due the collective motion can be described by the quantum mechanical rigid rotor, which has the following Hamiltonian

$$\hat{H}_{rot} = \frac{\hbar^2}{2} \sum_{i=1}^3 \frac{\hat{R}_i}{\mathcal{I}_i}, \quad (2.12)$$

where the \mathcal{I}_i are the moments of inertia relative to the body-fixed frame and the \hat{R}_i are components of the rotational angular momentum and the 3-axis is chosen to be aligned with the symmetry axis as shown in figure 2.6. The total angular momentum of the nucleus can now be written as



$$\hat{\mathbf{I}} = \hat{\mathbf{R}} + \hat{\mathbf{J}}, \quad (2.13)$$

where $\hat{\mathbf{J}}$ is the intrinsic total angular momentum. Thus \hat{H}_{rot} can be rewritten as

$$\hat{H}_{rot} = \frac{\hbar^2}{2} \sum_i \frac{(\hat{I}_i - \hat{J}_i)^2}{\mathcal{I}_i} = \frac{\hbar^2}{2} \left[\sum_i \frac{\hat{I}_i^2}{\mathcal{I}_i} - \sum_i \frac{2\hat{I}_i \hat{J}_i}{\mathcal{I}_i} + \sum_i \frac{\hat{J}_i^2}{\mathcal{I}_i} \right]. \quad (2.14)$$

Since the last term in Eq. (2.14) acts only on intrinsic degrees of freedom it can be absorbed into the intrinsic part of the total Hamiltonian which is

$$\hat{H} = \hat{H}'_{rot} - \sum_i \frac{\hbar^2}{\mathcal{I}_i} \hat{I}_i \hat{J}_i + \hat{H}_{intr}. \quad (2.15)$$

In Eq. (2.15) the term containing $\hat{I}_i \hat{J}_i$ produces a Coriolis interaction that can be ignored in a simplistic model under the condition that single particle

excitations are much larger than rotational excitations. This is usually the case for the low spin structure of light nuclei.

In general the rotor Hamiltonian \hat{H}'_{rot} does not have analytical solutions, except in the special case where the nucleus is axially symmetric

$$\mathcal{I}_1 = \mathcal{I}_2 = \mathcal{I}, \quad (2.16)$$

where some progress can be made analytically [14]. By making the above substitution, \hat{H}'_{rot} can be rewritten as

$$\hat{H}'_{rot} = \frac{\hbar^2}{2} \left[\frac{\hat{\mathbf{I}}^2}{\mathcal{I}} + \left(\frac{1}{\mathcal{I}_3} - \frac{1}{\mathcal{I}} \right) \hat{I}_3^2 \right], \quad (2.17)$$

with eigenvalues

$$E'_{KI} = \frac{\hbar^2}{2} \left[\frac{I(I+1)}{\mathcal{I}} + \left(\frac{1}{\mathcal{I}_3} - \frac{1}{\mathcal{I}} \right) K^2 \right]. \quad (2.18)$$

The eigenvectors for \hat{H}'_{rot} can now be written as $|KIM\rangle$ and satisfy the following eigenvalue relations

$$\hat{\mathbf{I}}^2 |KIM\rangle = I(I+1) |KIM\rangle \quad (2.19)$$

$$\hat{I}_z |KIM\rangle = M |KIM\rangle \quad (2.20)$$

$$\hat{I}_3 |KIM\rangle = K |KIM\rangle. \quad (2.21)$$

In the above, K and M are the projections of angular momentum I onto the body-fixed 3-axis and laboratory-fixed \hat{z} -axis respectively. Eq. (2.18) defines bands of excited states for different values of K

$$E_{\alpha KI} = E_{\alpha K} + \frac{\hbar^2}{2\mathcal{I}_\alpha} I(I+1), \quad (2.22)$$

where $E_{\alpha K}$ (the energy of the intrinsic configuration) and \mathcal{I}_α (the moment of inertia) are parameters to be fitted to experimental data [14]. The emergence of these bands is a feature similar to what is observed in the study of rigid molecules having axial symmetry.

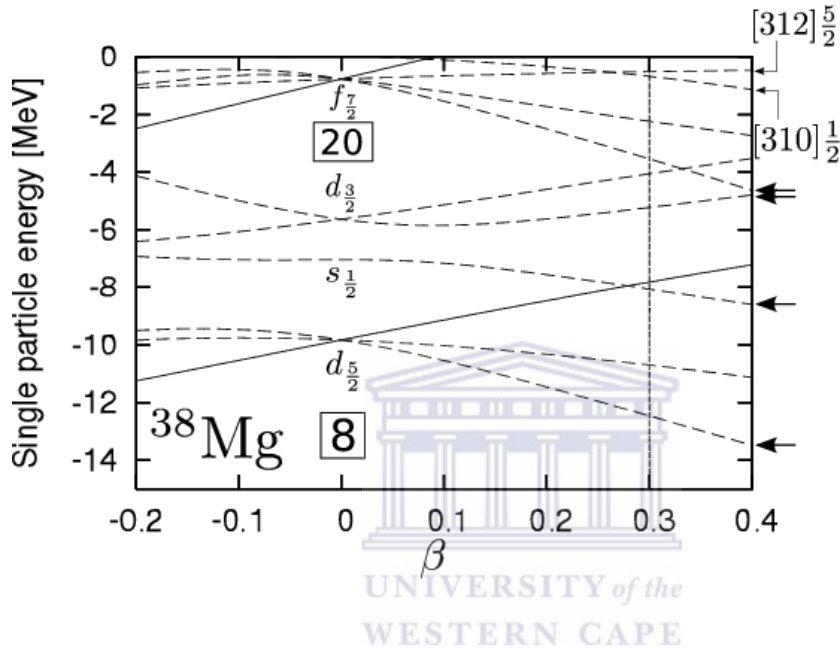


Figure 2.7: Nilsson diagram shows the effect of quadrupole deformation on the single particle states. The quadrupole deformation is labeled here as β [18].

Another important consequence of the deformed shape is that states with differing spatial orientations are exposed to different potentials depending on the shape of the nucleus. For axially symmetric deformations, when ϵ is positive, the equipotential surfaces elongate along the \hat{z} -axis and the nucleus becomes a prolate spheroid (see figure 2.5a). Hence states with high K sit further from the nuclear surface and are less bound, while the opposite is true for low K states. When ϵ is negative, the equipotential surfaces shrink along the \hat{z} -axis, the nucleus becomes an oblate spheroid (see figure 2.5c). Here the situation is reversed (high K states are more bound and low K

states are less bound). This is often represented in a Nilsson diagram shown in figure 2.7 and is a consequence of the short range of the nuclear force. It is important to note that, up to this point, deformation of the nucleus has been discussed in the context of the body-fixed frame. In other words, at the lowest-order, the shape of a rotating nucleus is characterized by its intrinsic quadrupole moment Q_0 in its rest frame. However, this is not what is measured experimentally. Instead what is measured in the laboratory is the spectroscopic quadrupole moment Q_s , which depends on the nuclear spin in the lab frame. These two quantities are not in general identical and it is possible for a nucleus to have some intrinsic deformation which does not appear in the spectroscopic quadrupole moment. The spectroscopic quadrupole moment is related to the body-fixed quadrupole moment via

$$Q_s(I, K) = \frac{3K^2 - I(I + 1)}{(I + 1)(2I + 3)} Q_0. \quad (2.23)$$

It is important to note that by convention states in the Nilsson model are labeled by the total number of harmonic oscillator quanta usually labeled N , the number oscillator quanta along the 3-axis n_3 , and the projections of intrinsic orbital and total angular momentum onto the 3-axis which often carry labels of Λ and Ω . This Ω is the same as K from fig.2.6

2.2 Multipole Moments for a Charge Distribution

As mentioned previously, in nuclear structure studies it is often the case that we are interested in leading order charge and current distributions in nuclei. This is where the multipole expansions become a powerful tool. Simplisti-

cally, the multipole expansion of an electromagnetic field is in fact a Taylor expansion where the lowest order terms are dominant and higher order moments can be neglected without sacrificing too much accuracy.

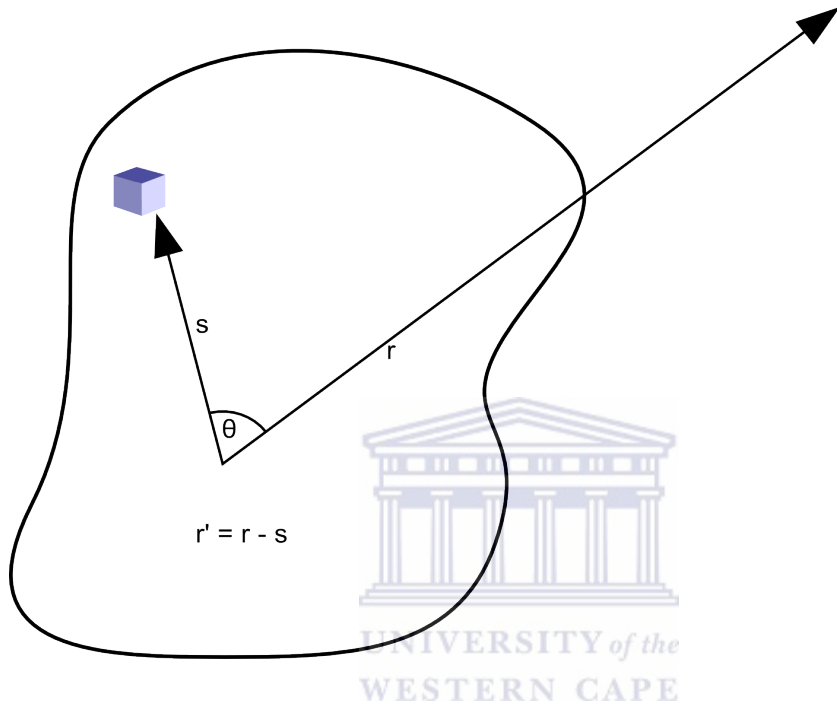


Figure 2.8: An arbitrary continuous charge distribution with \mathbf{s} as the displacement of a small charge element and \mathbf{r} being the displacement vector to the point at which we want to approximate the potential.

Let us begin by looking at the scalar potential,

$$V(\mathbf{r}) = \frac{1}{4\pi\epsilon_0} \int_0^\tau \frac{1}{r'} \rho(\mathbf{s}) d\tau'. \quad (2.24)$$

Using the cosine law, r' can be expressed, as shown in figure 2.8 in terms of r and s

$$r'^2 = r^2 + s^2 - 2rs \cos(\theta) = r^2 \left[1 + \left(\frac{s}{r}\right)^2 - \left(\frac{s}{r}\right) 2 \cos(\theta) \right] \quad (2.25)$$

which can also be written as

$$r' = r\sqrt{1 + \delta} \quad (2.26)$$

with

$$\delta = \left(\frac{s}{r}\right) \left(\frac{s}{r} - 2 \cos(\theta)\right). \quad (2.27)$$

Thus, Eq.(2.24) now becomes

$$V(\mathbf{r}) = \frac{1}{4\pi\epsilon_0} \int_0^\tau \frac{1}{r\sqrt{1 + \delta}} \rho(\mathbf{s}) d\tau'. \quad (2.28)$$

Now, in the limit $r \gg s$ implies $\delta \ll 1$ and so we apply a binomial expansion to the $\frac{1}{\sqrt{1+\delta}}$ term giving

$$\frac{1}{r\sqrt{1 + \delta}} = \frac{1}{r} \left[1 - \frac{1}{2}\delta + \frac{3}{8}\delta^2 - \frac{5}{16}\delta^3 + \dots \right]. \quad (2.29)$$

Therefore, more explicitly,

$$\begin{aligned} \frac{1}{r'} = \frac{1}{r} & \left[1 - \frac{1}{2} \left(\frac{s}{r}\right) \left(\frac{s}{r} - 2 \cos(\theta)\right) \right. \\ & \left. + \frac{3}{8} \left(\frac{s}{r}\right)^2 \left(\frac{s}{r} - 2 \cos(\theta)\right)^2 - \frac{5}{16} \left(\frac{s}{r}\right)^3 \left(\frac{s}{r} - 2 \cos(\theta)\right)^3 + \dots \right]. \quad (2.30) \end{aligned}$$

By multiplying out and rearranging the terms to group them in powers of $\frac{d}{r}$ we obtain

$$\frac{1}{r'} = \frac{1}{r} \left[1 + \left(\frac{s}{r}\right) (\cos(\theta)) + \left(\frac{s}{r}\right)^2 \frac{(3 \cos^2(\theta) - 1)}{2} + \left(\frac{s}{r}\right)^3 \frac{(5 \cos^3(\theta) - 3 \cos(\theta))}{2} + \dots \right]. \quad (2.31)$$

As it turns out, the coefficients in this series are the Legendre polynomials in cosine which form an orthogonal basis set in function space. This also means the above can be rewritten as

$$\frac{1}{r'} = \frac{1}{r} \sum \left(\frac{s}{r}\right)^n P_n(\cos \theta), \quad (2.32)$$

where P_n denotes the Legendre polynomial of degree n . Finally, substitution back into the potential gives

$$V(\mathbf{r}) = \frac{1}{4\pi\epsilon_0} \sum \frac{1}{r^{n+1}} \int_0^\tau s^n P_n(\cos \theta) \rho(\mathbf{s}) d\tau'. \quad (2.33)$$

This result is the multipole expansion of the electrostatic potential in powers of $\frac{1}{r}$. Summing over all the terms of the expansion is, as a matter of fact, an exact solution for the potential. However, the real value of the expansion is that it can be used as a tool for approximating the potential. In such cases only the leading order terms play an important role.

From here it is easy to find the multipole expansion of the electric field by applying the gradient operator to the scalar potential

$$\mathbf{E}(\mathbf{r}) = -\nabla V(\mathbf{r}). \quad (2.34)$$

This procedure can be carried out in a similar fashion for the vector potential $\mathbf{A}(\mathbf{r})$, expanding the $\frac{1}{r}$ part just as before. This gives

$$\mathbf{A}(\mathbf{r}) = \frac{\mu_0 I}{4\pi} \oint \frac{1}{r'} d\mathbf{l} = \frac{\mu_0 I}{4\pi} \sum \frac{1}{r^{n+1}} \oint s^n P_n(\cos \theta) d\mathbf{l}. \quad (2.35)$$

Since Legendre polynomials turn out to be special cases of the spherical harmonics, both $V(\mathbf{r})$ and $A(\mathbf{r})$ can be written in as

$$V(\mathbf{r}) = \frac{1}{4\pi\epsilon_0} \sum \frac{1}{r^{\ell+1}} \int_0^\tau \frac{4\pi s^\ell \rho(\mathbf{s})}{2\ell+1} Y_{\ell m}^*(\theta, \phi) Y_{\ell m}(\theta, \phi) d\tau' \quad (2.36)$$

$$A(\mathbf{r}) = \frac{\mu_0 I}{4\pi} \sum \frac{1}{r^{\ell+1}} \oint \frac{4\pi s^\ell}{2\ell+1} Y_{\ell m}^*(\theta, \phi) Y_{\ell m}(\theta, \phi) d\mathbf{l}. \quad (2.37)$$

Looking more closely at $V(\mathbf{r})$ and multiplying and dividing by Z we get

$$V(\mathbf{r}) = \frac{1}{4\pi\epsilon_0} \sum \frac{1}{r^{\ell+1}} \frac{4\pi Z}{2\ell+1} \left[\frac{1}{Z} \int_0^\tau e s^\ell \rho(\mathbf{s}) Y_{\ell m}^*(\theta, \phi) d\tau' \right] Y_{\ell m}(\theta, \phi) \quad (2.38)$$

$$= \frac{1}{4\pi\epsilon_0} \sum \frac{1}{r^{\ell+1}} \frac{4\pi Z}{2\ell+1} Q_{\ell m} Y_{\ell m}(\theta, \phi). \quad (2.39)$$

Quantum mechanically, the $Q_{\ell m}$'s take the role of operators, such that

$$Q_{\ell m} = \langle \psi(\mathbf{s}) | e s^\ell Y_{\ell m}^*(\theta, \phi) | \psi(\mathbf{s}) \rangle \quad (2.40)$$

$$= \langle \psi(\mathbf{s}) | O_{\ell m}(E) | \psi(\mathbf{s}) \rangle. \quad (2.41)$$

In the above $\hat{O}_{\ell m}(E)$ is now the electric multipole operator of order (ℓ, m) . As mentioned previously, the quadrupole moments in nuclei tell us if the nuclear shape is prolate or oblate. The leading-order quadrupole moment operator is known to be

$$\hat{Q}_{20}(E) = er^2 Y_{20}^*(\theta, \phi) \quad (2.42)$$

$$= e(3 \cos^2(\theta) - r^2) \quad (2.43)$$

$$= e(3z^2 - r^2). \quad (2.44)$$

2.3 Fermi's Golden Rule

Fermi's Golden Rule provides a means for calculating transition probabilities in nuclear and atomic systems. I describe this briefly below.

For a number of nuclei in an initial excited state $|i\rangle$, the decay rate is given by the famous radioactive decay law,

$$\frac{dN(t)}{dt} = -\lambda N(t), \quad (2.45)$$

where $N(t)$ is the number of excited nuclei at time t and λ is the transition probability. The solution to this differential equation yields the well known exponential decay law

$$N(t) = N_0 e^{-\lambda t}. \quad (2.46)$$

The mean life or lifetime of the state is then given by

$$\tau = \frac{\int_0^\infty t e^{-\lambda t} dt}{\int_0^\infty e^{-\lambda t} dt} = \frac{1}{\lambda}. \quad (2.47)$$

Heisenberg's uncertainty principle relates the mean lifetime to the width of the excited state, such that

$$\Gamma \tau = \hbar, \quad (2.48)$$

where Γ is the spread in the energy of the excited state. Over a large number of measurements N , one can obtain an average energy whose quantum mechanical analogue is the expectation value $\langle E \rangle$

$$\langle E \rangle = \frac{1}{N} \sum_{i=1}^N E_i. \quad (2.49)$$

The spread in the energy values can be estimated by taking the square-root of the variance [19]

$$\Gamma = \left[\frac{1}{N} \sum_{i=1}^N (E_i^2 - \langle E \rangle^2) \right]^{\frac{1}{2}}. \quad (2.50)$$

The quantity Γ is related to the probability of measuring the energy of the state to be a specific value. As will be shown below, Fermi's Golden Rule shows that transition probabilities are proportional to the nuclear matrix elements

$$\mathcal{M}_{fi} = \langle \psi(J_f, M_f) | \hat{O}_{\ell m} | \psi(J_i, M_i) \rangle, \quad (2.51)$$

which can be factorized using the Wigner-Eckart theorem into a reduced matrix element and a Clebsch-Gordan coefficient

$$\mathcal{M}_{fi} = (-1)^{J_f - M_f} \begin{pmatrix} J_f & \ell & J_i \\ M_f & m & M_i \end{pmatrix} \langle \psi(J_f) | | \hat{O}_{\ell} | | \psi(J_i) \rangle. \quad (2.52)$$

Therefore, measured transition matrix elements yield important information about the structure of atomic nuclei, particularly the operators and the overlap of the wave functions in Eq. (2.52)

Fermi's Golden Rule can be derived using perturbation theory, where the time-dependence of the Hamiltonian is treated as a first order perturbation,

so that

$$\hat{H} = \hat{H}_0 + \hat{H}'(t). \quad (2.53)$$

If $|\phi_n\rangle$ are a complete orthonormal basis set of eigenvectors of \hat{H}_0 so that

$$\hat{H}_0|\phi_n\rangle = E_n|\phi_n\rangle, \quad (2.54)$$

then $|\Psi(\mathbf{r}, t)\rangle$, any general eigenstate of \hat{H} , is also a solution of the time-dependent Schrödinger equation and can be expressed as

$$|\Psi(\mathbf{r}, t)\rangle = \sum_n c_n(t) e^{-iE_n t/\hbar} |\phi_n\rangle. \quad (2.55)$$

Substituting the above into the time-dependent Schrödinger equation we get

$$i\hbar \frac{\partial |\Psi(\mathbf{r}, t)\rangle}{\partial t} = [\hat{H}_0 + \hat{H}'(t)] |\Psi(\mathbf{r}, t)\rangle \quad (2.56)$$

$$i\hbar \sum_n \left[\frac{\partial c_n(t)}{\partial t} - i c_n(t) \frac{E_n}{\hbar} \right] e^{-iE_n t/\hbar} |\phi_n\rangle = \sum_n c_n(t) [\hat{H}_0 |\phi_n\rangle + \hat{H}'(t) |\phi_n\rangle] e^{-iE_n t/\hbar}. \quad (2.57)$$

Furthermore, taking an inner product with $\langle \phi_k | e^{iE_k t/\hbar}$ yields

$$i\hbar \sum_n \left[\frac{\partial c_n(t)}{\partial t} - i c_n(t) \frac{E_n}{\hbar} \right] e^{i(E_k - E_n)t/\hbar} \langle \phi_k | \phi_n \rangle, \quad (2.58)$$

on the left side and

$$\sum_n c_n(t) [\langle \phi_k | \hat{H}_0 | \phi_n \rangle + \langle \phi_k | \hat{H}'(t) | \phi_n \rangle] e^{i(E_k - E_n)t/\hbar} \quad (2.59)$$

on the right-hand side. Finally, the orthonormality of the eigenstates $|\phi_n\rangle$

yields

$$i\hbar \frac{\partial c_k(t)}{\partial t} = \sum_n \langle \phi_k | \hat{H}'(t) | \phi_n \rangle e^{i\omega_{kn}t}, \quad (2.60)$$

where $\omega_{kn} = (E_k - E_n)/\hbar$.

If we assume that the nucleus is in an initial state $|\phi_0\rangle$ and that $\hat{H}'(t)$ is almost constant over the time interval of interest, then $c_k(t)$ can be solved explicitly [19]

$$c_k(t) = \frac{\langle \phi_k | \hat{H}'(t) | \phi_0 \rangle}{(E_k - E_0)} (1 - e^{i\omega_{k0}t}), \quad (2.61)$$

so that

$$|c_k(t)|^2 = \frac{2}{\hbar^2} |\langle \phi_k | \hat{H}'(t) | \phi_0 \rangle|^2 \frac{(1 - \cos(\omega_{k0}t))}{\omega_{k0}^2}. \quad (2.62)$$

Now the transition probability (λ) to a set of final states (labeled by f) is given by

$$\lambda = \frac{d}{dt} \sum_{k \in f} |c_k(t)|^2 \quad (2.63)$$

$$= \frac{2}{\hbar^2} \int |\langle \phi_k | \hat{H}'(t) | \phi_0 \rangle|^2 \frac{\sin(\omega_{k0}t)}{\omega_{k0}} \rho(E_k) dE \quad (2.64)$$

$$= \frac{2\pi}{\hbar^2} |\langle \phi_k | \hat{H}'(t) | \phi_0 \rangle|^2 \rho(E_f) \quad (2.65)$$

where $\rho(E_f)$ is the density of final states. This result is Fermi's Golden Rule which relates nuclear matrix elements to lifetimes.

2.4 The Relation Between Lifetime Measurements and Coulomb Excitation

As emphasised in the previous section, lifetime measurements give important nuclear structure information via Fermi's Golden Rule. In this section I focus on a particular kind of experiment called Coulomb excitation, where independent lifetime measurements together with measured quadrupole transition strengths can give important information about the shapes of nuclei that are studied.

Coulomb excitation is a technique used for measuring matrix elements of electric multipole transitions, which yield transition probabilities. Coulomb excitation has the distinct advantage of relying solely on the Coulomb interaction to produce the excited states in the nuclei of interest. As a result, the analysis is simplified by the fact that the effects of the strong interaction can be safely ignored. In order to achieve this it is important that the nuclear surfaces remain well separated (≈ 6.5 fm for light nuclei and ≈ 5 fm for heavy nuclei).

In Coulomb-excitation experiments, a projectile is scattered inelastically off a target nucleus and in this time-dependent process the Coulomb interaction is used to excite states in the target and projectile nuclei. In the early days of accelerator technology it was only possible to use light nuclei as projectiles; due to which the electromagnetic interaction between target and projectile was comparatively weak and so only a few states could be populated [20]. In later years, as accelerator technology improved, it became practical to use heavy ions as projectiles. This allowed a large number of excited states to be populated. In the following years the technique was further developed and refined to become an important tool for investigating transi-

tion probabilities of low-lying collective excitations. One particular aspect of this field of research involved determination of spectroscopic quadrupole moments by reorientation effect measurements [21].

Coulomb-excitation measurements rely on the ability to make measurements of differential cross sections. In practice this means taking measurements at various scattering angles, which might be affected by poor statistics, particularly in radioactive ion beam experiments. In such cases the total cross section can still be measured. The inelastic scattering cross section in a Coulomb excitation can be written in the semi-classical limit as

$$\left(\frac{d\sigma}{d\Omega}\right)_n = P_n \left(\frac{1}{4}a^2 \sin^{-4}\left(\frac{\vartheta}{2}\right)\right), \quad (2.66)$$

where P_n is the probability of the nucleus being Coulomb excited into state $|n\rangle$ and the rest is the well known Rutherford scattering cross section, where ϑ is the scattering angle in the centre of mass frame and a is half the distance of closest approach in a head-on collision given (in the c.g.s. system) by

$$a = \frac{b}{2} = \frac{Z_1 Z_2 e^2}{\mu v^2}, \quad (2.67)$$

where b is the impact parameter and μ is the reduced mass [20].

The cross sections for inelastic scattering can be measured experimentally and from these data the reduced transition probability can be extracted. In first-order perturbation theory, the inelastic scattering cross section for an electric quadrupole ($E2$) excitation, can be expressed as

$$d\sigma_{E2} = \left(\frac{Z_1 e}{\hbar\nu}\right)^2 a_{if}^{-2} B(E2, I_i \rightarrow I_f) df_{E2}(\vartheta, \xi), \quad (2.68)$$

where a_{if} is the distance of closest approach in a head-on collision, $B(E2, I_i \rightarrow$

I_f) is the reduced transition strength and $df_{E2}(\vartheta, \xi)$ is the differential scattering cross section which depends on the centre of mass angle ϑ and the adiabaticity parameter ξ [22]. The reduced transition probability relates to the electric quadrupole matrix element so that

$$B(E2, I_i \rightarrow I_f) = \frac{1}{I_0 + 1} |\langle I_0 M_0 | \hat{M}(E2) | I_f M_f \rangle|^2. \quad (2.69)$$

As outlined previously, the operator in the electric quadrupole matrix element is given by Eq. (2.44) and the reduced transition probability is related to the lifetime τ . In the rotational model, the $B(E2, I_i K \rightarrow I_f K)$ relates to the quadrupole moment via

$$B(E2, I \rightarrow I - 2) = \frac{5}{16\pi} e^2 Q_0^2 |\langle I_i 2K0 | I_f K \rangle|^2, \quad (2.70)$$

which yields the absolute value of Q_0 once the $B(E2)$ value is known. However this does not provide information on the sign of Q_0 . Reorientation effect measurements provide the sign of Q_s , and hence, Q_0 . Eq. (2.69) can also be rewritten as

$$B(E2, I_i \rightarrow I_f) = 8.161 \times 10^{-10} E_\gamma P_\gamma(E2, I_i \rightarrow I_f), \quad (2.71)$$

where $P_\gamma(E2)$ is the partial γ -ray transition probability, which can be obtained from the total transition probability of the level

$$P_\gamma(E2) = P(\text{level}) \frac{I_\gamma(E2)}{I_\gamma(\text{total})} \quad (2.72)$$

$$= \frac{1}{\tau} \frac{I_\gamma(E2)}{I_\gamma(\text{total})}, \quad (2.73)$$

where $I_\gamma(E2)$ is the intensity of the γ -ray transition and $I_\gamma(\text{total})$ is the sum

of the intensities of all transitions depopulating the level. This equation can additionally be used to extract magnetic dipole to electric quadrupole ($M1/E2$) mixing ratios¹ if enough experimental spectroscopic information is available. For a typically mixed $M1/E2$ transition the probabilities $P_\gamma(E2)$ and $P_\gamma(M1)$ are given by

$$P_\gamma(E2) = \frac{P(\text{level})}{1 + \delta^{-2} + \alpha_T(E2) + \delta^{-2}\alpha_T(M1)} \quad (2.74)$$

$$P_\gamma(M1) = \frac{P(\text{level})}{1 + \delta^2 + \alpha_T(M1) + \delta^2\alpha_T(E2)} \quad (2.75)$$

where δ and α_T are multipole mixing ratios and total internal conversion coefficients,² respectively. As a result, if a $B(E2)$ value can be measured with Coulomb excitation and the lifetime is obtained from an independent lifetime measurement, the mixing ratio and $M1$ transition strength can also be extracted.

Finally, complementary lifetime measurements are relevant in Coulomb-excitation studies if the transition probability can be inserted from an independent measurement, providing valuable insight in the study of nuclear shapes. This is illustrated in the example of ^{70}Se , shown in figure 2.9, where both lifetime and Coulomb-excitation measurements have been used to determine the shape of the nucleus [2]. The overlap between the transitional matrix element determined via lifetime measurements and the Coulomb-excitation curve provides a means to deduce the nuclear shape in the labo-

¹Analogous to the electric charge distribution described previously, magnetic transitions occur due to varying current distributions in nuclei. The lowest-order moment in such current distributions is the magnetic dipole moment represented by the magnetic moment operator $\vec{\mu}$. In electromagnetic transitions in nuclei the radiation field is written in terms of the eigenfunctions of angular momentum operators (the spherical harmonics) which allow both electric and magnetic multipoles.

²Internal conversion becomes important in heavier nuclei and for low-energy high-multipole order transitions where the multipole radiation field of the excited nucleus causes an emission of an inner shell electron instead of usual γ -ray emission.

ratory frame. As shown in figure 2.9, this method relies on the accuracy of both measurements.

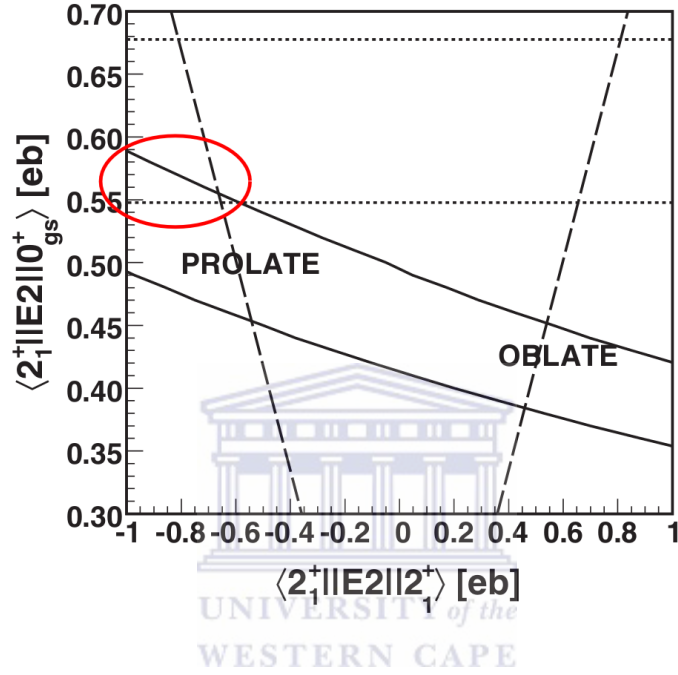



Figure 2.9: Plot of the transition matrix element as a function of the diagonal matrix element for the 2_1^+ state in ^{70}Se . The extreme values consistent with measurement of the $2_1^+ \rightarrow 0_{gs}^+$ transition in ^{70}Se are shown as solid lines. The dotted horizontal lines show the $1\text{-}\sigma$ limits on $\langle 2_1^+ || E2 || 0_{gs}^+ \rangle$ obtained from a lifetime measurement [1]. The region where the two measurements overlap is circled here and indicates that the nucleus should be prolate.

Chapter 3

Nuclear Lifetimes II - Astrophysics

3.1 Introduction



Life as we know it would not exist without stars. We depend almost entirely on energy from the Sun. Beyond this, almost all the chemical elements heavier than lithium (such as carbon, calcium and iron, etc.) can only have been synthesized in these giant furnaces. This makes stellar astrophysics a rather interesting topic of study.

3.1.1 Life Cycles of Stars

A star starts out as a cloud of interstellar gas which collapses under its own gravity. This collapse occurs when the gravitational energy of the system surpasses the thermal energy of the individual particles that make up the gas:

$$\frac{GM^2}{R} \geq \frac{3kTM}{2m}, \quad (3.1)$$

or equivalently

$$M \geq 3.7 \left(\frac{kT}{Gm} \right)^{\frac{3}{2}} \rho^{-\frac{1}{2}}, \quad (3.2)$$

where M , R and T are the total mass, radius and temperature of the cloud respectively, m is the mean molecular weight and ρ is the density. This is called the Jeans criterion [23]. For typical interstellar clouds (which are made of mostly neutral hydrogen with density around $100 \text{ atoms cm}^{-3}$ and temperature of around 100 K) the mass required to fulfill the Jeans criterion is $2 \times 10^4 M_{\odot}$ ¹ [23]. As the cloud collapses, the density increases rapidly. If the temperature is kept relatively constant during this time through radiating away the energy released, the mass required to fulfill the Jeans criterion reduces, allowing smaller regions of the cloud to individually collapse under their own gravity. Thus, the large cloud fragments into smaller clouds, each collapsing under its own weight. This stage of stellar evolution, where the gas is essentially in free fall lasts for a few decades. This is one of the crucial initial processes that lead to the formation of stars. The precise details of this process are still not completely known [23].

In the early stages of star formation, the energy released by the gravitational collapse is easily radiated away because of the transparency of the gas. However, as the cloud collapses, the density and opacity of the gas increases allowing some energy to be trapped within the gas, thereby raising the temperature of the cloud. The internal pressure of the gas now starts to play a role and the rate of collapse becomes dependent on the rate at which the energy is radiated from the star. At this stage, the time-scale of radiation cooling is longer than the time-scale of collapse. Thus the interior temperature of the star rises steadily. This stage of stellar evolution can last

¹The notation M_{\odot} denotes a solar mass, a unit of mass commonly used in astronomy and astrophysics which is equivalent to the mass of our Sun.

several million years [23].

Eventually the temperature of the core reaches $\sim 10^7$ K, high enough for thermonuclear reactions to begin with fusing hydrogen nuclei. This is the main sequence stage of stellar evolution (which can take several billion years for smaller stars) so named because the star remains on the main sequence of the Hertzsprung-Russell (H-R) diagram shown in figure 3.1. On the main sequence, energy is mainly produced via hydrogen burning while the star is in hydrostatic equilibrium, which is explained in the next section. As a result, the star's size, temperature and luminosity hardly change during this time. The main sequence stage comes to an end with the depletion of the hydrogen fuel in the core, after which the evolution of the star depends on its mass [23].

Once hydrogen is depleted in the core and the rate of energy production begins to drop, gravitational collapse resumes. This rapidly increases the temperature in an envelope surrounding the core, creating a hydrogen burning shell. There is a rapid release of energy in this region so it cannot be radiated away fast enough to maintain hydrostatic equilibrium. Thus the core temperature rises, while the outer layers of the star are forced to expand and cool. The lower surface temperature of the star means it becomes redder and the higher energy production rate means it becomes brighter. Such stars are located at the red giant branch of the H-R diagram. In some massive stars helium burning may begin in the core. Depending on the mass, some stars may be able to ignite the burning of successively heavier elements that were produced in the previous burning stages. This process, which is mostly helium burning produces elements like carbon, nitrogen and oxygen which are eventually burnt producing heavier elements all the way up to iron.

Stars in the mass region of the Sun (up to $\sim 8M_{\odot}$) have enough mass

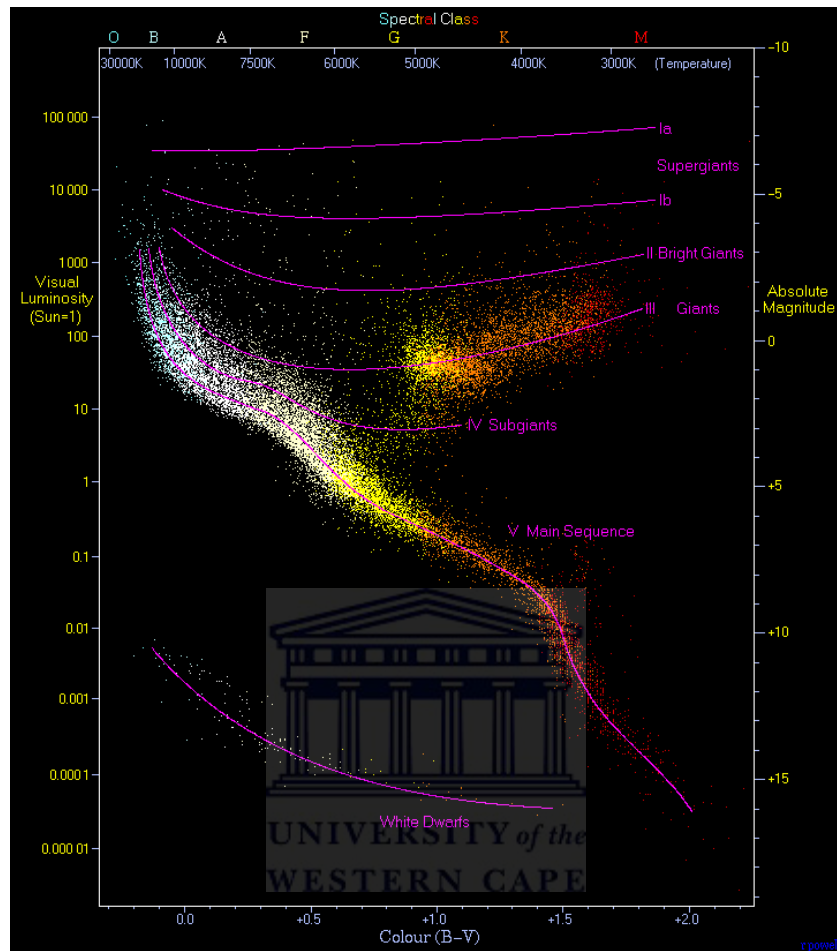


Figure 3.1: A Hertzsprung-Russell diagram is a plot of luminosity against temperature (or spectral class) for a group of stars. The diagram shows various structures associated with different stages of stellar evolution. At the top are supergiants which are not very clear in this diagram. Below this we find the main sequence and the giant and subgiant branches. Stars such as the sun spend most of their lives on the main sequence burning hydrogen. It is only when they begin to deplete the hydrogen in their cores that they migrate off towards the right. Stars in the upper left hand side of the main sequence tend to be more massive and burn hydrogen faster. As a result these stars are expected to be the first to deplete their hydrogen supply and leave the main sequence. Having left the main sequence, these stars move to the subgiant and giant branches. The point at which the giant branch meets the main sequence is known as the main sequence turn off and provides a means of estimating the age of a stellar population [24].

to ignite helium burning, but not enough to ignite carbon burning once the helium is depleted. In such stars, towards the end of their life, the star's core is composed primarily of carbon and oxygen, surrounded by a helium burning shell, a layer of helium ash from hydrogen burning, a hydrogen burning shell and an outer layer of hydrogen. Similarly as explained before, the energy produced in the inner burning shells is not easily radiated away, forcing the outer layers to expand and cool. This pushes the star up the asymptotic giant branch in the H-R diagram. Eventually the outer layers of gas are forced away from the core to form a planetary nebula. The exposed carbon-oxygen core has a high temperature and low luminosity and forms a typical white dwarf.

Very massive stars nearing the end of their fuel supply are stuck with iron cores and have no alternative but gravitational collapse. The gravitational collapse forces photodisintegration of iron nuclei and electron capture which consumes energy. To compensate for this energy loss, the core collapses faster and faster leading to a large explosion called a supernova.

3.1.2 Equilibrium Conditions in the Stellar Interior

Most stars are in hydrostatic equilibrium, so that the internal pressure is balanced by the weight of the outer layers of gas. Mathematically this means the gradient of the pressure is

$$\frac{dP(r)}{dr} = \frac{-GM(r)\rho(r)}{r^2}, \quad (3.3)$$

where $P(r)$ is the internal pressure at radial distance r and G is the gravitational constant [25]. The minus sign reflects the fact that gravity acts toward the centre of the star. In the above, $\rho(r)$ is the density at distance r and

$M(r)$ is the mass contained within a spherical shell,

$$M(r) = \int_0^r 4\pi r'^2 \rho(r') dr'. \quad (3.4)$$

If one assumes that the pressure on the surface of the star vanishes, the pressure at the centre ($r = 0$) can be written as

$$P(0) \approx 8\rho_s \frac{GM}{R}, \quad (3.5)$$

where ρ_s is the mean density of the star [26].

If the equilibrium condition does not hold, then the right-hand side of Eq. (3.6) determines whether the star implodes or expands

$$\rho \ddot{r} = -G \left(\frac{M\rho}{r^2} \right) - \frac{dP}{dr}. \quad (3.6)$$

Ordinary stellar interiors are composed mostly of gaseous material which is well described by the ideal gas law

$$PV = nkT \quad (3.7)$$

which can be rewritten as

$$P(r) = \frac{k}{m} \rho(r) T(r), \quad (3.8)$$

where k is Boltzmann's constant and m is the mean molecular weight of the particles in the gas ($m \approx \frac{1}{2}m_H$). Assuming $\rho(0) = 2\bar{\rho}$, where $\bar{\rho} \simeq \frac{M}{R^3}$ is the density at a point midway between the centre and surface, and using the earlier estimate for $P(0)$ gives [23]

$$T(0) = \left(\frac{m}{k}\right) \left(\frac{GM}{R}\right), \quad (3.9)$$

which yields a value of around 10^7 K for the Sun.

Stars constantly radiate large amounts of energy in the form of electromagnetic radiation and jets of high energy particles. Although it is well known that objects radiate energy by virtue of temperature, no object can keep radiating energy over such long time scales simply because of high temperature. Thus energy must come from some other source in order for the star to maintain the high temperature. The thermal energy, E_T , of the star is well approximated by integrating the thermal energy per unit mass for an ideal gas over the entire star

$$E_T = \int_0^R \left[\frac{3}{2} \frac{k}{m} T\right] \rho(r) 4\pi r^2 dr \simeq \overline{\left[\frac{3}{2} \frac{k}{m} T\right]} M. \quad (3.10)$$

The total gravitational energy, E_G , is given by integrating over the entire star

$$E_G = \int_0^R \left[\frac{-GM(r)}{r}\right] \rho(r) 4\pi r^2 dr \simeq -\overline{\left[\frac{GM(r)}{r}\right]} M. \quad (3.11)$$

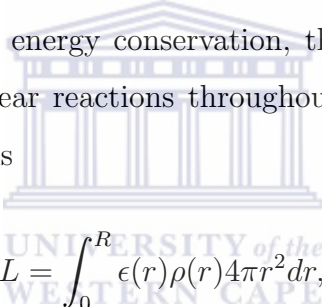
A numerical calculation of these values for the Sun gives a result of $2E_T \approx -E_G$. In its general form this is the virial theorem [23], which states that in a non-rotating star one half of the energy released by gravitational collapse goes to the internal energy while the other half is radiated away.

Given the luminosity of the sun, the virial theorem indicates it ought to have radiated all its thermal energy in $\sim 4.4 \times 10^7$ years. Since the earth itself is around 4.5 billion years old, clearly there must be another energy source in the Sun that has not yet been taken into consideration [23]. That source is the energy released by nuclear fusion. It is estimated that the total

amount of energy that can be released by fusion would allow the Sun to shine at its current luminosity for around 10^{11} years.

3.1.3 Nuclear Reactions

Hydrostatic equilibrium alone is not enough to ensure a stable star. Thermal equilibrium must also be taken into account, which requires that all parts of the star have reached the same temperature. This condition can obviously not hold since stellar cores can reach temperatures of the order of 10^7 K while surface temperatures are of the order of 10^3 K. To make matters worse, the energy radiated from the surface of the star prevents perfect thermal equilibrium. However, by energy conservation, the energy leaving the star must be replaced by nuclear reactions throughout the interior of the star. Mathematically this means



$$L = \int_0^R \epsilon(r) \rho(r) 4\pi r^2 dr, \quad (3.12)$$

where L is the luminosity of the star and $\epsilon(r)$ is the rate of energy released by nuclear reactions per unit time per unit mass of stellar material. This condition allows maintenance of an energy balance over the whole star that keeps it stable over cosmological time scales. Indeed when thermonuclear reactions cease within the star it begins to collapse [23].

3.2 Reaction Rates

In determining the rate at which energy is produced in a star via thermonuclear fusion, one useful tool is the Q -value,

$$Q = (m_1 + m_2 - m_3 - m_4)c^2, \quad (3.13)$$

for a nuclear reaction, $1 + 2 \rightarrow 3 + 4$. This is the energy liberated in the (exothermic) reaction for $Q > 0$. This alone is not enough to determine the rate at which the energy is produced. The rate of energy production also depends on the number density of the reactants and the cross section of the reaction.

The cross section is classically the geometrical cross sectional area of the two reactants $\sigma = \pi(R_1 + R_2)^2$ where R_1 and R_2 are the radii of the individual nuclei. Since nuclear reactions are governed by the rules of quantum mechanics, this geometrical cross section must be modified to $\sigma = \pi\lambda^2$, where λ is the reduced de Broglie wavelength,

$$\lambda = \frac{m_1 + m_2}{m_2} \frac{\hbar}{(2m_1 E_1)^{1/2}}. \quad (3.14)$$

Here E_1 is the kinetic energy of m_1 in the laboratory frame. It is easy to see from Eq.(3.14) that the cross section is energy dependent. This is the same as saying the cross section depends on the relative velocity between m_1 and m_2 , so that $\sigma \equiv \sigma(v)$. The reaction rate r is then given by

$$r = N_1 N_2 v \sigma(v), \quad (3.15)$$

where N_1 and N_2 are the number densities of the nuclei of type 1 and 2. As the velocities of the particles in a star follow a distribution, it is often useful to work with the average value

$$\langle v\sigma \rangle = \int_0^\infty \phi(v) v \sigma(v) dv, \quad (3.16)$$

where $\phi(v)$ is a normalized probability density function, described below. Thermonuclear reactions take place in the plasma present in stellar cores

and the energy of the reactants is by virtue of their relative thermal motion. This stellar plasma is usually non-degenerate and the particles within move at non-relativistic speeds. For a plasma in thermodynamic equilibrium one can use a Maxwell-Boltzmann velocity distribution

$$\phi(v) = 4\pi v^2 \left(\frac{m}{2\pi kT} \right)^{3/2} \exp\left(\frac{-mv^2}{2kT} \right). \quad (3.17)$$

Since the exponential term is proportional to mv^2 the function $\phi(v)$ can be written in terms of energy:

$$\phi(v) \propto E \exp\left(\frac{-E}{kT} \right). \quad (3.18)$$

This means that when $E \ll kT$, the function increases linearly with E and when $E \gg kT$ the function decreases exponentially with increasing E . For reactions in a stellar plasma, the velocities of both the interacting nuclear species (labeled as x and y) are important. Both are described by the distributions

$$\phi(v_x) = 4\pi v_x^2 \left(\frac{m_x}{2\pi kT} \right)^{3/2} \exp\left(\frac{-m_x v_x^2}{2kT} \right) \quad (3.19)$$

$$\phi(v_y) = 4\pi v_y^2 \left(\frac{m_y}{2\pi kT} \right)^{3/2} \exp\left(\frac{-m_y v_y^2}{2kT} \right). \quad (3.20)$$

Thus the reaction rate per pair of interacting particles is given by

$$\langle v\sigma \rangle = \int_0^\infty \int_0^\infty \phi(v_x) \phi(v_y) v \sigma(v) dv_y dv_x. \quad (3.21)$$

It is more useful to work with the relative velocity v and the centre-of-mass velocity V which are related to v_x and v_y by the classical Galilean transformations. The expression for $\langle v\sigma \rangle$ can then be transformed into

$$\langle v\sigma \rangle = \int_0^\infty \int_0^\infty \phi(V)\phi(v)v\sigma(v)dv dV, \quad (3.22)$$

with redefined velocity distributions

$$\phi(V) = 4\pi V^2 \left(\frac{M}{2\pi kT} \right)^{3/2} \exp\left(\frac{-MV^2}{2kT} \right) \quad (3.23)$$

$$\phi(v) = 4\pi v^2 \left(\frac{\mu}{2\pi kT} \right)^{3/2} \exp\left(\frac{-\mu v^2}{2kT} \right), \quad (3.24)$$

where μ is the reduced mass and M is the total mass. Since σ depends only on v , we can immediately integrate Eq.(3.22) over V which yields

$$\langle v\sigma \rangle = \left(\frac{8}{\pi\mu} \right)^{1/2} \frac{1}{(kT)^{3/2}} \int_0^\infty \sigma(E) E \exp\left(\frac{-E}{kT} \right) dE. \quad (3.25)$$

Consider now a general case of two nuclei fusing to form a compound nucleus which then decays into two other nuclei

$$1 + 2 \rightarrow 3 + 4 + Q, \quad (3.26)$$

where $Q > 0$ at low stellar temperatures. As the temperature rises, more and more particles have energy greater than the Q -value and so the reverse process becomes more important. The forward process can be viewed as the fusion of two nuclei which proceeds through an excited state in a compound nucleus C

$$1 + 2 \rightarrow C \rightarrow 3 + 4 + Q. \quad (3.27)$$

The cross section for this process is given by

$$\sigma_{12} = \pi \lambda_{12}^2 \underbrace{\frac{2J+1}{(2J_1+1)(2J_2+1)}}_{\omega} (1 + \delta_{12}) |\langle 3+4 | H_{II} | C \rangle \langle C | H_I | 1+2 \rangle|^2, \quad (3.28)$$

which includes a term $\pi\lambda_{12}^2$ described previously and a statistical factor ω where J is the angular momentum of the excited state in the compound nucleus and J_1 and J_2 represent the angular momenta of the nuclei in the entrance channel. The statistical factor is essentially a sum over all final states averaged over all initial states [27]. The term $(1 + \delta_{12})$ with the Kronecker δ takes care of the possibility of the nuclei being identical particles in which case the cross section must be doubled. The last term contains the matrix elements which depend on the specific interaction(s) involved. Since this reaction proceeds through an intermediate state, it is a two-step (resonant) reaction. As a result of this, there are two matrix elements involved, one for the transition into the compound nucleus $\langle C|H_I|1 + 2\rangle$ and one for the transition from the compound nucleus to the final state $\langle 3 + 4|H_{II}|C\rangle$. In general these two transitions do not have to involve the same interaction and thus their operators are labeled differently H_I and H_{II} . The cross section for the reverse process can be constructed similarly

$$\sigma_{34} = \pi\lambda_{34}^2 \frac{2J + 1}{(2J_3 + 1)(2J_4 + 1)} (1 + \delta_{34}) |\langle 1 + 2|H_I|C\rangle \langle C|H_{II}|3 + 4\rangle|^2, \quad (3.29)$$

where the matrix elements are reversed. As a result of time reversal invariance, which applies to the strong and electromagnetic interactions, the matrix elements in each equation should be equal. Thus the cross sections are proportional to each other

$$\frac{\sigma_{12}}{\sigma_{34}} = \frac{\lambda_{12}^2 (2J_3 + 1)(2J_4 + 1) (1 + \delta_{12})}{\lambda_{34}^2 (2J_1 + 1)(2J_2 + 1) (1 + \delta_{34})}. \quad (3.30)$$

Expanding the $\frac{\lambda_{12}^2}{\lambda_{34}^2}$ term with $\lambda^2 = \hbar^2/(2\mu_{xy}E_{xy})$ (where μ_{xy} and E_{xy} are the reduced mass and center-of-mass energy respectively) this is reduced to

$$\frac{\sigma_{12}}{\sigma_{34}} = \frac{m_3 m_4 E_{34}}{m_1 m_2 E_{12}} \frac{(2J_3 + 1)(2J_4 + 1)(1 + \delta_{12})}{(2J_1 + 1)(2J_2 + 1)(1 + \delta_{34})}. \quad (3.31)$$

It should be noted that this relation is only valid in the non-relativistic regime and it contains no information about the compound nucleus even though it was derived assuming a two step process. This means the cross sections can be obtained independently, regardless of the intermediate state. This result is general and in many instances it may be easier to make a measurement of the cross section for the reverse process rather than trying to directly measure the cross section of interest [23].

The rate of energy production ϵ_{12} depends on the Q -value and the reaction rate r_{12} , so that $\epsilon_{12} = Qr_{12}$. This is often expressed in terms of the density of the stellar material ρ . Since at high stellar temperatures the reverse reaction becomes important as well, the net rate of energy production in a star is usually expressed as [23]

$$\epsilon_{net} = \epsilon_{12} + \epsilon_{34} = (r_{12} - r_{34})Q/\rho. \quad (3.32)$$

3.3 Resonances

Resonant reactions are those which proceed via some intermediate stage and lead to large enhancements of the reaction cross section. These reactions play an important role in thermonuclear reactions where particle energies are low compared to the Coulomb barrier.

To begin with, we look at the familiar case of plane waves incident on a three-dimensional attractive square well potential of radius R . We restrict our discussion to low energy neutron scattering. The neutron has two distinct channels, an elastic scattering channel and a reaction channel. We have two

distinct regions, region I where $r < R$ and region II where $r > R$. In region I $V(r) = -V_0$ and in region II $V(r) = 0$. In this case we have the general solution for the wave function in region I

$$u_I = Ae^{iKr} + Be^{-iKr} \quad (3.33)$$

and in region II

$$u_{II} = Ce^{iKr} + De^{-iKr}. \quad (3.34)$$

We consider only waves coming in from $r \gg R$ and can set $A = 0$. This means that the incoming waves are either reflected at the boundary or transmitted to region I. Given this interpretation we define the transmission coefficient

$$\hat{T} = \frac{|B|^2}{|D|^2}. \quad (3.35)$$

In addition, we have the continuity condition which requires that the wave function be smooth. This means that both the wave function and its derivatives must be continuous everywhere. So at the boundary between region I and region II

$$u_I(R) = u_{II}(R) \quad (3.36)$$

$$\frac{\partial}{\partial r}u_I(R) = \frac{\partial}{\partial r}u_{II}(R), \quad (3.37)$$

with

$$u_{in} = Ae^{iKr} + Be^{-iKr}. \quad (3.38)$$

The second term in Eq. (3.38) represents incoming waves and the first term

represents reflected waves. It is expected that the amplitude of the reflected waves is reduced by a factor q due to absorption. We should also take into account the possibility of the reflected waves being shifted in phase by some factor ζ relative to the incoming waves. This means $|A|^2 \leq |B|^2$, with the condition [3]

$$A = Be^{2i\zeta}e^{-2q}. \quad (3.39)$$

Folding this into Eq. (3.38) yields

$$u_{in} = Be^{2i\zeta}e^{-2q}e^{iKr} + Be^{-iKr} \quad (3.40)$$

$$= B[e^{-i(Kr+\zeta+iq)} + e^{i(Kr+\zeta+iq)}]e^{i(\zeta-q)} \quad (3.41)$$

$$= 2Be^{i(\zeta-q)}\cos(Kr + \zeta + iq). \quad (3.42)$$

Taking the logarithmic derivative of the radial wave function then leads to

$$f_0 = R \left(\frac{1}{u_{in}(r)} \frac{du_{in}(r)}{dr} \right)_{r=R} \quad (3.43)$$

$$= R \frac{-2Be^{i(\zeta-q)}K \sin(KR + \zeta + iq)}{2Be^{i(\zeta-q)}\cos(KR + \zeta + iq)} \quad (3.44)$$

$$= -KR \tan(KR + \zeta + iq). \quad (3.45)$$

From this it should be clear that f_0 is energy dependent and that this dependency arises from the dependencies of K , ζ and q on energy [3]. Since the properties of the nuclear interior are not completely known, we must try to express the cross section near a resonance in terms of quantities we can measure. First we impose the condition for a resonance energy E_λ where

$$f_0(E_\lambda, q) = -KR \tan(KR + \zeta + iq) = 0. \quad (3.46)$$

Many energies may fulfill this condition, but we will consider just one. We will assume that elastic scattering is the dominant process so that $|q| \ll 1$ and look at the Taylor expansion in order to approximate f_0 near the resonance energy

$$f_0 \approx f_0(E_\lambda, q) + (E - E_\lambda) \left(\frac{\partial f_0}{\partial E} \right)_{E_\lambda, q=0} + q \left(\frac{\partial f_0}{\partial q} \right)_{E_\lambda, q=0}. \quad (3.47)$$

The last term can be expanded using Eq. (3.45)

$$q \left(\frac{\partial f_0}{\partial q} \right)_{E_\lambda, q=0} = -qKR \left[\frac{\partial}{\partial q} \tan(KR + \zeta + iq) \right]_{E_\lambda, q=0} = -iqKR. \quad (3.48)$$

The $\left(\frac{\partial f_0}{\partial E} \right)_{E_\lambda, q=0}$ term is expected to be real since $q = 0$ implies a vanishing reaction cross section. Substitution back into Eq. (3.47) yields

$$f_0 \approx (E - E_\lambda) \left(\frac{\partial f_0}{\partial E} \right)_{E_\lambda, q=0} - iqKR = \text{Re}(f_0) + i\text{Im}(f_0). \quad (3.49)$$

Given this result we define the new quantities

$$\Gamma_{\lambda e} \equiv -\frac{2kR}{(\partial f_0 / \partial E)_{E_\lambda, q=0}} \quad (3.50)$$

$$\Gamma_{\lambda r} \equiv -\frac{2qKR}{(\partial f_0 / \partial E)_{E_\lambda, q=0}} \quad (3.51)$$

$$\Gamma_\lambda \equiv \Gamma_{\lambda e} + \Gamma_{\lambda r}, \quad (3.52)$$

where $\Gamma_{\lambda e}$ and $\Gamma_{\lambda r}$ are the elastic scattering and reaction partial widths respectively and their sum is then the total width. Notice that only $\Gamma_{\lambda r}$ really depends on q . With this the reaction cross section (from Eq. (A.14)) can be re-written as

$$\sigma_{re} = \frac{\pi}{k^2} \frac{\Gamma_{\lambda e} \Gamma_{\lambda r}}{(E - E_\lambda)^2 + \frac{\Gamma_\lambda^2}{4}} \quad (3.53)$$

which clearly has a peak at $E = E_\lambda$ and has a full width at half maximum of Γ_λ which is why this quantity is called the width of the resonance. This result is the Breit-Wigner formula for s -wave neutrons. Importantly, when $|E - E_\lambda| \gg \Gamma_\lambda$ (far from the resonance energy), the reaction cross section all but disappears leaving only the elastic scattering cross section. So far this treatment has neglected the angular momentum considerations and the effects of the Coulomb barrier. A fuller treatment can be found in Blatt and Weisskopf [27]. On including a statistical factor for the orbital angular momentum degenerate states, the resonant scattering cross section is²

$$\sigma_{re,l} = (2\ell + 1) \frac{\pi}{k^2} \frac{\Gamma_{\lambda e} \Gamma_{\lambda r}}{(E - E_\lambda)^2 + \frac{\Gamma_\lambda^2}{4}}. \quad (3.54)$$

3.3.1 Astrophysical S-factor

In general, while analysing nuclear reactions it is important to consider the tunneling probability through the Coulomb barrier. This probability is re-

²The $(2\ell + 1)$ term is replaced by $\frac{2J+1}{(2J_1+1)(2J_2+1)}$ for the general case of resonant reactions.

lated to the Sommerfeld parameter defined as

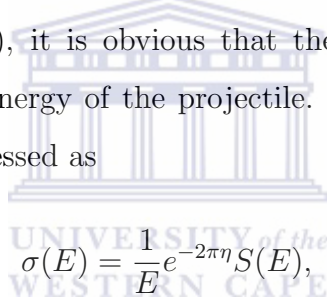
$$\eta = \frac{a}{\lambda} \quad (3.55)$$

$$= \frac{Z_1 Z_2 e^2}{\hbar v}, \quad (3.56)$$

where a is the half distance of closest approach as mentioned in Chapter 2 Section 2.4 and λ is the reduced de Broglie wavelength from Eq. (3.14) so that,

$$P = e^{-2\pi\eta}. \quad (3.57)$$

Clearly the cross section for a reaction drops rapidly below the Coulomb barrier. From Eq. (3.14), it is obvious that the cross section also drops linearly with increasing energy of the projectile. In light of the above, the cross section can be expressed as



$$\sigma(E) = \frac{1}{E} e^{-2\pi\eta} S(E), \quad (3.58)$$

where $S(E)$ is the astrophysical S -factor and encapsulates all the nuclear physics effects. For non-resonant reactions the S -factor varies smoothly with center-of-mass energy and changes less rapidly with beam energy than the cross section. It is therefore a useful tool for extrapolating cross sections away from resonances. In terms of the S -factor the reaction rate can be written as

$$\langle v\sigma \rangle = \left(\frac{8}{\pi\mu} \right)^{1/2} \frac{1}{(kT)^{3/2}} \int_0^\infty S(E) e^{-2\pi\eta} e^{\left(\frac{-E}{kT}\right)} dE, \quad (3.59)$$

which is proportional to both the Maxwellian distribution, which decreases exponentially at high energies, and the Gamow factor, which increases expo-

nentially with energy. As a result $\langle v\sigma \rangle$ has a peak at intermediate energies as shown in figure 3.2. This energy regime is known as the Gamow window and it defines the energy range most relevant for astrophysical reaction rates.

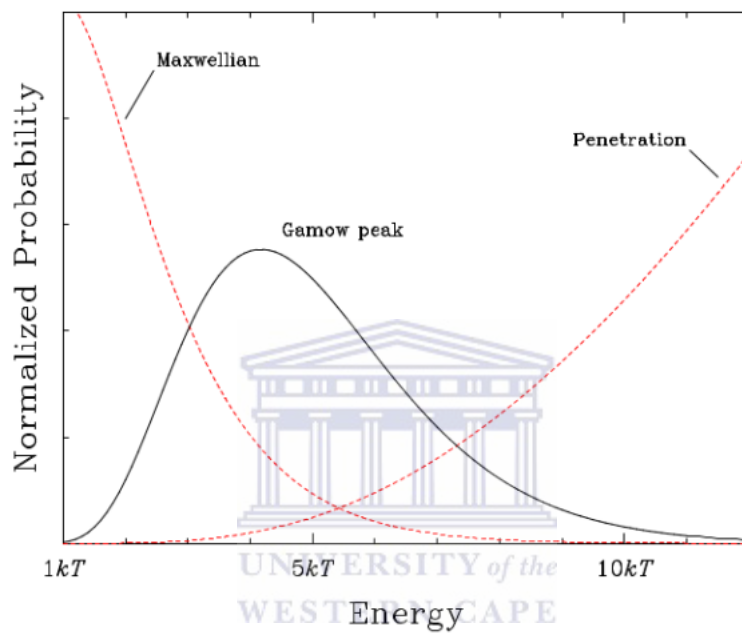


Figure 3.2: The Gamow window sits at intermediate energies, where the Maxwellian distribution and tunneling probability are comparable.

3.4 Hydrogen Burning

3.4.1 PP-chains

For most of a star's life it is dependent on hydrogen burning for energy production [23]. Hydrogen burning can proceed via various mechanisms which are sensitive to the precise conditions within the stellar core. One method is for hydrogen burning to proceed via the proton-proton chains (or pp-chains). These reactions have the net result of fusing four protons into a ${}^4\text{He}$ nucleus



This is a multi-step process going through various different reactions. If we assume a stellar gas consisting entirely of hydrogen, then the only reactants will be protons and the first reaction in the pp-chains produces deuterium as follows



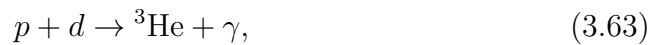
The next step is the burning of deuterium and several reactions are possible

$$\begin{aligned}
& d(p, \gamma)^3\text{He} \\
& d(d, \gamma)^4\text{He} \\
& d(d, t)p \\
& d(d, n)^3\text{He} \\
& d(^3\text{He}, p)^4\text{He} \\
& d(^3\text{He}, \gamma)^5\text{Li} \\
& d(^4\text{He}, \gamma)^6\text{Li}.
\end{aligned}$$

Since the total reaction rate depends on the number of available particles and the reaction rate per particle pair $\langle\sigma v\rangle_{12}$

$$r_{12} = \frac{N_1 N_2}{1 + \delta_{12}} \langle\sigma v\rangle_{12}, \quad (3.62)$$

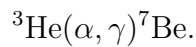
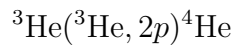
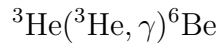
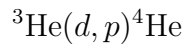
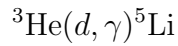
this means that processes involving protons dominate (due to large proton numbers in the stellar interior). So the first reaction



dominates over the others. The deuterium abundance in the star now depends on the deuterium producing rates and deuterium burning rates,

$$\frac{dD}{dt} = r_{pd} - r_{dp} = \frac{N_p^2}{2} \langle\sigma v\rangle_{pp} - N_p N_d \langle\sigma v\rangle_{pd}. \quad (3.64)$$

The final step is the burning of ^3He , where once again there are several possible reactions which can take place



Of these the ${}^3\text{He}(d, p){}^4\text{He}$ and ${}^3\text{He}({}^3\text{He}, 2p){}^4\text{He}$ reactions have the largest S -factors and play important roles. Since the deuterium abundance in stars is very low, the latter reaction dominates. This completes the first pp-chain (pp-chain I). The ${}^3\text{He}(\alpha, \gamma){}^7\text{Be}$ reaction also plays an important role in the stellar interior. This leads to two further branches (pp-chain II and pp-chain III) which can compete favourably with pp-chain I depending on the temperature of the core.

3.4.2 CNO cycles

Other important energy producing processes in stars are the CNO-cycles. These are not possible in first generation stars, which by definition have only the products of big bang nucleosynthesis available for fusion (mostly hydrogen and helium). Later generations of stars contain trace amounts of heavier nuclei formed by previous generations. In a sufficiently massive star the core reaches temperatures (and pressures) high enough for reactions involving these heavier nuclei to play an important role. The most significant reactions involve those nuclei with the lowest Coulomb barriers and the highest abundances. These are the carbon and nitrogen nuclei. Other nuclei between helium and carbon have lower Coulomb barriers but, their abundances are

so low that they do not play a significant role in energy production [23]. An important cycle for energy production in these stars (such as the sun) is the CNO cycle. We restrict our discussion to the cold CNO cycle, which is responsible for energy production in main sequence stars. The cycle starts with a ^{12}C nucleus capturing a proton and producing ^{13}N . It then proceeds through β^+ decay of ^{13}N , proton capture by ^{13}C , another proton capture by ^{14}N , β^+ decay by ^{15}O and finally regenerates ^{12}C via $^{15}\text{N}(p, \alpha)^{12}\text{C}$.

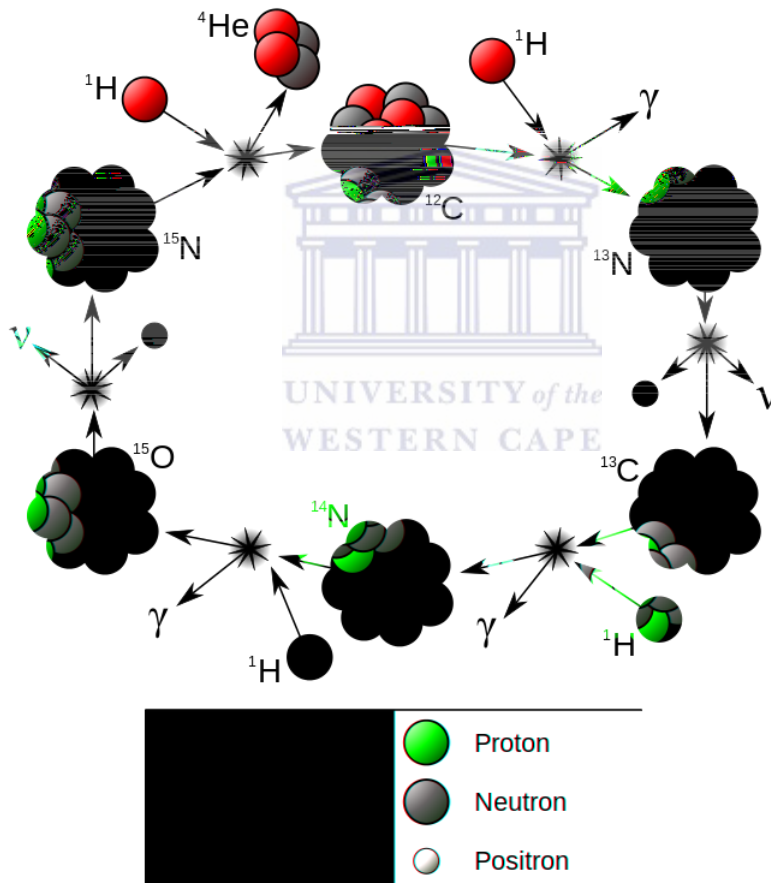
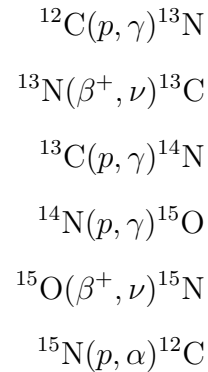


Figure 3.3: Pictorial description of the cold CNO cycle.



A diagram of the cycle is shown in figure 3.3.

Although the abundances of carbon and nitrogen nuclei are comparatively much lower than that of hydrogen in a young stellar interior, these nuclei are not consumed by the process. So the CNO cycle is a significant source of energy. As one would expect, the overall rate of energy production in the cycle depends on the slowest reaction. The nitrogen nuclei have the highest Coulomb barrier of all the capture reactions in the cycle. Since the ${}^{14}\text{N}(p, \gamma){}^{15}\text{O}$ reaction proceeds essentially via the electromagnetic interaction, while the ${}^{15}\text{N}(p, \alpha){}^{12}\text{C}$ proceeds mostly via the strong force, the ${}^{14}\text{N}(p, \gamma){}^{15}\text{O}$ reaction is expected to be the slowest reaction. As discussed below, the cross section for this reaction is the least well known of the cycle, and still remains an important research problem [28]. An accurate determination of the ${}^{14}\text{N}(p, \gamma)$ reaction rate is essential for understanding energy generation in main sequence stars and correlating measured neutrino fluxes from the Sun to the temperature and elemental composition of the solar core [4, 29].

3.5 The ${}^{14}\text{N}(p, \gamma){}^{15}\text{O}$ Reaction

As mentioned previously, the ${}^{14}\text{N}(p, \gamma){}^{15}\text{O}$ reaction, being the slowest, forms a bottleneck in the CNO-cycle. Thus a precise determination of this reaction

rate is important to better understand energy production in main sequence stars. As shown in figure 3.4, extrapolation of the S -factor to stellar energies shows large discrepancies arising from the results of various experiments.

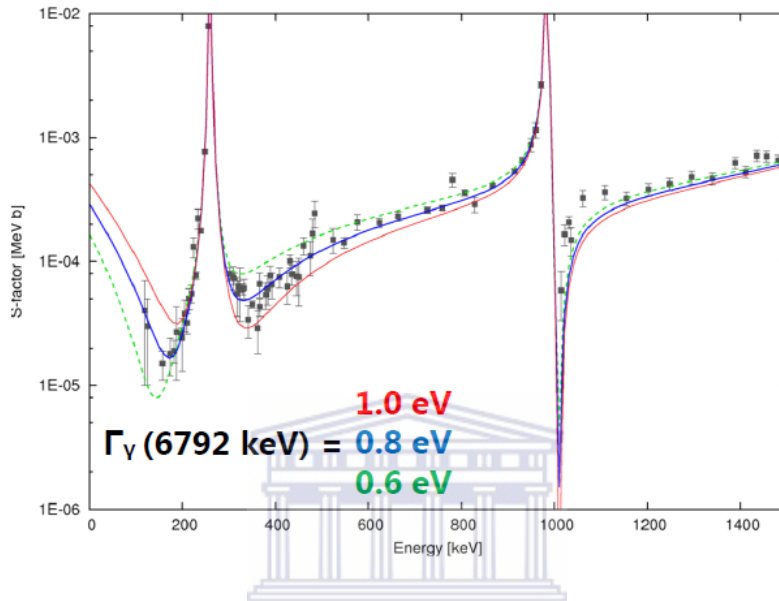


Figure 3.4: R-matrix fit highlighting the effect of uncertainties in the 6791 keV state. Note that very small changes in the width lead to large variations in the S -factor below 200 keV [28].

This is largely because of two reasons.

1. The S -factor is affected by a wide sub-threshold resonance from the 6791 keV state in ^{15}O , as shown in figure 3.5.
2. The Gamow window for the reaction is below 200 keV, where direct measurement of the cross section is difficult.

Instead the cross section is measured in a more practical region and the S -factor is then extrapolated to the Gamow peak. The procedure requires independently determined widths of the known resonances to be used in the extrapolations as shown in figure 3.4. This calls for an accurate measurement

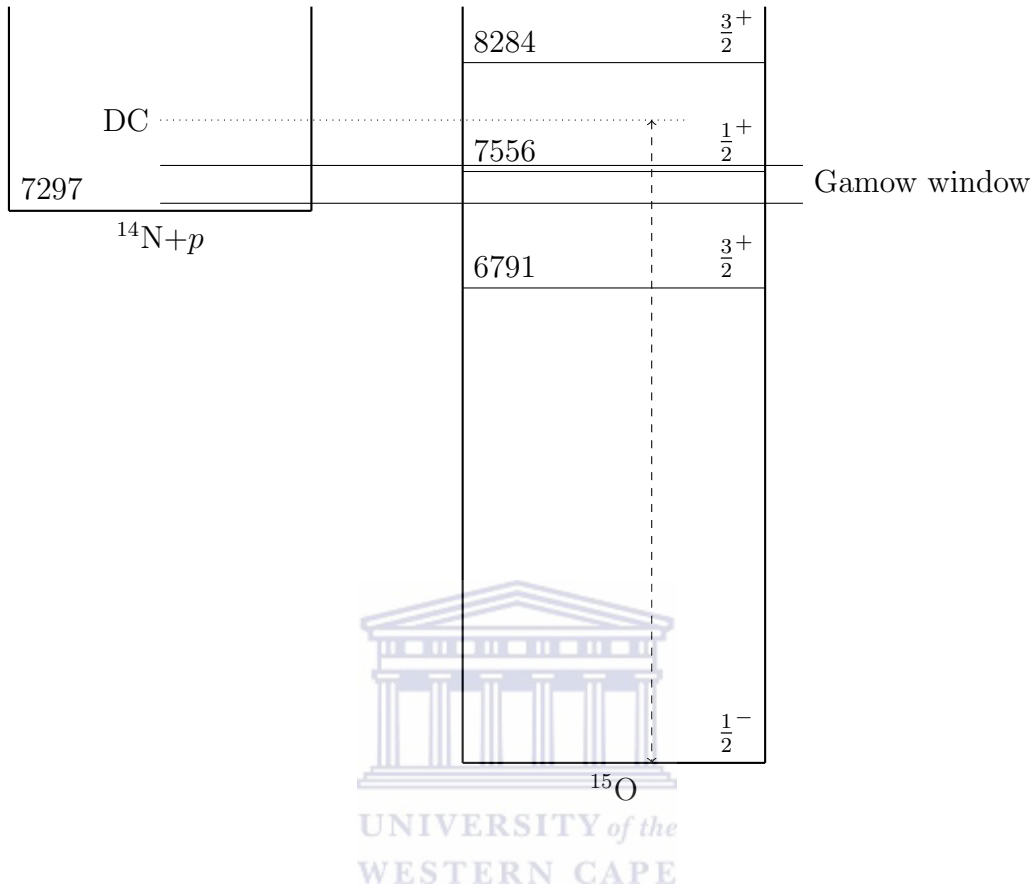


Figure 3.5: Level scheme of ^{15}O showing the excited state at 6791 keV which has a high energy tail contributing to the cross section in the Gamow window.

of the width (lifetime) of the sub-threshold 6791 keV state. To date, several attempts to measure the lifetime of the state have been made using various methods [8, 6, 30, 7], which agree reasonably well with one another. Attempts have also been made at direct cross section measurements and R-matrix fits [4, 5, 31]. A compilation of the results is shown in Table 5.1.

However, a weighted mean of the partial widths extracted from lifetimes shown above is $\Gamma_{\gamma}^{ave} = 0.59 \pm 0.12$ eV. This 20% relative uncertainty continues to be too large for reasonable extrapolations down to lower energies [28]. Therefore, there is a clear need for new lifetime measurements to stringently

Table 3.1: Compiled results of previous experiments.

Group	Method	τ_{γ}^{6791} [fs]	Γ_{γ}^{6791} [eV]
Oxford 1968 [7]	DSAM	< 28	> 0.023
TUNL 2001 [8]	DSAM	1.6 ± 0.7	0.41 ± 0.17
RIKEN 2004 [30]	CoulEx	0.69 ± 0.43	0.95 ± 0.59
LUNA 2004 [5]	R-Matrix fit	1.1 ± 0.5	0.59 ± 0.27
Bochum 2008 [9]	DSAM	< 0.77	> 0.85
LUNA 2008 [4]	R-Matrix fit	0.75 ± 0.20	0.87 ± 0.23
TRIUMF 2013 [6]	DSAM	< 1.42	> 0.46

constrain the S -factor extrapolations.

This thesis describes the design and simulation of a new set up at iThemba LABS that potentially allows one to remeasure the lifetime of the subthreshold state using the Doppler Shift Attenuation Method (DSAM). A measurement of this lifetime has already been carried out at TRIUMF [32] using a similar design. The published data offers useful guidance from our simulations. Since such lifetime measurements (of the order $\tau \approx 1$ fs) are extremely challenging, our goal is to produce the state similarly to Ref.[32] using the inverse kinematic transfer reaction ${}^3\text{He}({}^{16}\text{O}, {}^{15}\text{O}){}^4\text{He}$, so that we are least sensitive to systematic effects and have maximal sensitivity. In the next section I briefly discuss direct nuclear reactions before describing the design and the simulations.

3.6 Direct Nuclear Reactions

Nuclear reactions can be broadly classified on the basis of how a projectile interacts with target nuclei. On one extreme a projectile may impart energy to only a single nucleon exciting a single degree of freedom. On the other

extreme, the projectile may be totally absorbed into the nucleus, sharing its energy amongst all the available nucleons and forming a compound nucleus which later decays via an exit channel. Resonance reactions fall into the latter category.

Those reactions in which there is little change between the initial and final states (for example, with only single particle excitations) are known as direct nuclear reactions. Besides these, there are a variety of processes that exist between the two extreme cases mentioned above, such as semi-direct, pre-equilibrium, pre-compound and others [33]. A key feature distinguishing direct reactions from compound nucleus reactions is the time scale in which they occur. Direct reactions take place over a time scale comparable to the time of flight of the projectile while traversing the target nucleus. This is much shorter than what one would expect from resonant reactions, where the time scales are much longer, on the order of the lifetime of the compound state that is produced.

3.6.1 Scattering Theory

We begin by modelling the reaction as a scattering problem, where a beam of particles with a well defined momentum direction interacts with a nuclear potential. A sketch of the scenario can be found in figure 3.6. The initial and final states can be represented by wave functions which have the asymptotic forms

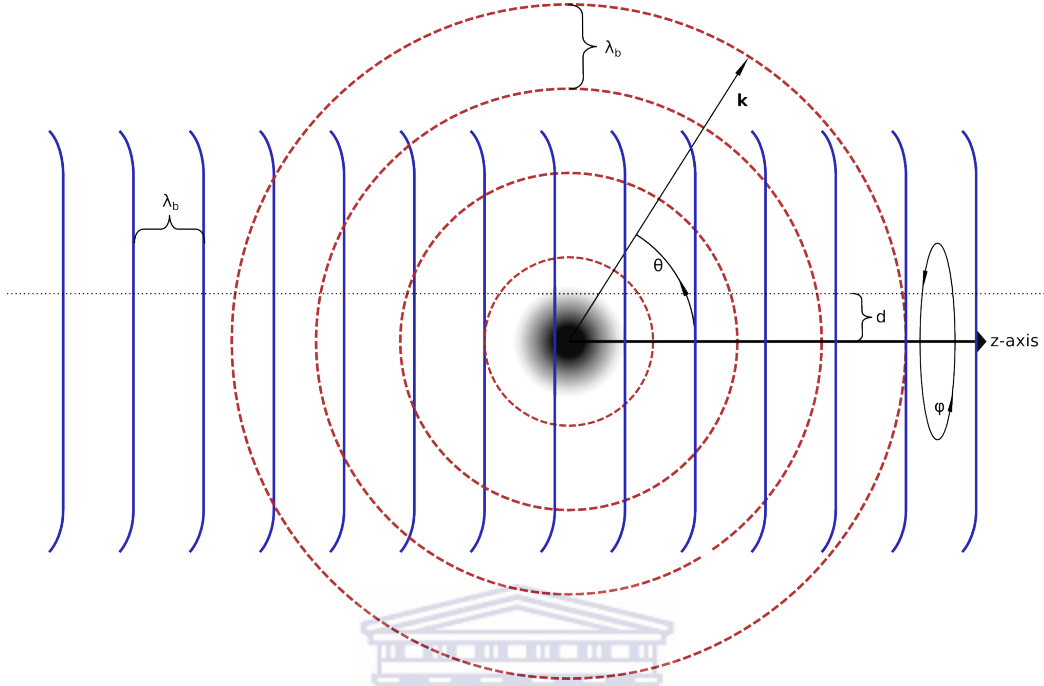


Figure 3.6: Diagram of the scenario described above. A localised central potential at the centre, a beam of particles approximated by plane waves with wavelength λ_a and scattered particles approximated as outward bound spherical waves with wavelength λ_b .

$$\psi_{initial} = A_0 e^{i(\mathbf{k}\cdot\mathbf{r})} \Psi_{projectile} \Psi_{target} \quad (3.65)$$

$$\lim_{r \rightarrow \infty} \psi_{final} = A_0 \left[e^{i(\mathbf{k}\cdot\mathbf{r})} \Psi_{projectile} \Psi_{target} + \sum_b f_b(\theta, \phi) \frac{e^{i(\mathbf{k}_b\cdot\mathbf{r})}}{r_b} \Psi_{ejectile} \Psi_{residual} \right]. \quad (3.66)$$

In the above, the index b ranges over all possible elastic and inelastic channels. Also introduced here is the scattering amplitude $f_b(\theta, \phi)$ which is proportional

to the differential cross section of the reaction,

$$\frac{d\sigma_b}{d\Omega} \propto |f_b(\theta, \phi)|^2. \quad (3.67)$$

A fuller treatment of the scattering problem can be found in appendix A.

3.6.2 Born approximation

In the simplistic description above much of the information relating to the specifics of the reaction has been ignored. However, solving the Schrödinger equation requires some explicit handling of these factors. All the information needed to describe the internal structure of both the target and the projectile is encapsulated in the wave functions Ψ .

Unlike the time independent Schrödinger equation for a bound state problem in a central field

$$\left[\frac{-\hbar^2}{2m} \nabla^2 + V(r) - E \right] \Psi(\mathbf{r}) = 0, \quad (3.68)$$

which can easily be solved using standard methods, here the states involved are in the continuum and the nature of the potential $V(r)$ is not known explicitly. Thus, the Schrödinger equation reduces to an inhomogeneous Helmholtz equation

$$(\nabla^2 + k^2)\Psi(\mathbf{r}) = \lambda U(r)\Psi(\mathbf{r}), \quad (3.69)$$

where $k^2 = \frac{2mE}{\hbar^2}$, $U(r) = \frac{2m}{\hbar^2}V(r)$ and λ is a parameter related to the strength of the potential. The situation is further complicated if we allow reactions to excite internal degrees of freedom so that the total Hamiltonian can be

written as

$$\hat{H} = \hat{H}_{\text{target}} + \hat{H}_{\text{projectile}} - \frac{\hbar^2}{2\mu_\alpha} \nabla_\alpha^2 + V(r)_\alpha, \quad (3.70)$$

which now contains a term $\frac{\hbar^2}{2\mu_\alpha} \nabla_\alpha^2$ describing the relative motion of the two nuclei³ and an interaction potential $V(r)_\alpha$ proportional to $\lambda U(r)$ [34]. Introducing this to the Schrödinger equation yields, for the special case of elastic scattering

$$\left[E - \hat{H}_{\text{target}} - \hat{H}_{\text{projectile}} + \frac{\hbar^2}{2\mu_\alpha} \nabla_\alpha^2 \right] \Psi = V(r)_\alpha \Psi. \quad (3.71)$$

For convenience we collect the operator terms into a free particle Hamiltonian \hat{H}_0 so that

$$\left[E - \hat{H}_0 \right] \Psi = V(r)_\alpha \Psi. \quad (3.72)$$

In the limit $V(r)_\alpha \rightarrow 0$, the eigenstates involved ought to be plane wave eigenstates ψ_0 . Therefore, the solutions to the Helmholtz equation can be written in the form

$$\Psi = \left[E - \hat{H}_0 \right]^{-1} V(r)_\alpha \Psi + \psi_0. \quad (3.73)$$

The above is called the Lippmann-Schwinger equation and it has singularities when E takes eigenvalues of \hat{H}_0 . This can be solved by shifting the poles slightly as follows. Since

$$\lim_{\epsilon \rightarrow 0} \left[E - \hat{H}_0 + i\epsilon \right]^{-1} \simeq \left[E - \hat{H}_0 \right]^{-1}, \quad (3.74)$$

we can write

$$\Psi = \lim_{\epsilon \rightarrow 0} \left[E - \hat{H}_0 + i\epsilon \right]^{-1} V(r)_\alpha \Psi + \psi_0, \quad (3.75)$$

³In general many target-projectile combinations are possible, the subscript α takes care of this.

as a particular solution to Eq. (3.73), where ψ_0 satisfies the eigenvalue equation

$$\left[E - \hat{H}_0 \right] \psi_0 = 0. \quad (3.76)$$

In shorthand notation, one can use a substitution for the operator in Eq. (3.75)

$$\lim_{\epsilon \rightarrow 0} \left[E - \hat{H}_0 + i\epsilon \right]^{-1} V(r)_\alpha = \hat{\mathcal{O}}, \quad (3.77)$$

so that

$$\Psi = \psi_0 + \hat{\mathcal{O}}\Psi \quad (3.78)$$

is a general solution to the integral equation. It is apparent that the solution to Eq (3.77) is in fact an infinite series, called the Born series

$$\Psi = \sum_{\mu=0} \hat{\mathcal{O}}^\mu \psi_0. \quad (3.79)$$

which converges for a small interaction coupling λ . This is the Plane Wave Born Approximation or PWBA. In reality the Coulomb interaction in nuclei will distort the incident waves somewhat. Therefore, it is often more appropriate to use the Distorted Wave Born Approximation or DWBA with the aid of a computer program such as DWUCK4 [35].

3.6.3 Partial Waves

So far the effects of angular momentum have been ignored. In reality angular momentum plays an important role in characterising the scattering amplitude. To see this we take a closer look at the scenario sketched earlier, in particular the assumption that the wave function for the incident particles can be approximated with plane waves. Since we have chosen $\mathbf{k} = k_z$ it is

implied that the uncertainty in the xy - position of each particle is large, or equivalently that the beam must be smeared over a certain area and so the impact parameter (labeled d in figure 3.6) cannot be known a priori. Since ℓ is the cross-product of position with momentum ($\mathbf{r} \times \mathbf{p}$) this means that the incoming angular momentum must be a sum over all possible angular momentum states⁴. Since we have assumed a central potential, ℓ is a good quantum number and the wavefunction can be separated into radial and angular parts [36]. The spherical harmonics form a complete orthonormal set of eigenfunctions for the angular momentum operator ℓ^2 . So the initial and final wavefunctions in a scattering problem can be expressed as a sum of partial waves

$$\psi_{initial} = e^{ikz} = \sum_{\lambda=0}^{\ell} \sum_{\mu=-\lambda}^{\mu=\lambda} c_{\lambda} u_{\lambda}(r) Y_{\lambda\mu}(\theta, \phi) \quad (3.80)$$

$$\psi_{final} = f_b(\theta, \phi) \sum_{\lambda=0}^{\ell} \sum_{\mu=-\lambda}^{\mu=\lambda} d_{\lambda} u_{\lambda}(r) Y_{\lambda\mu}(\theta, \phi). \quad (3.81)$$

In the above, the wave function is separated into a radial part, $u_{\ell}(r)$, and an angular part, $Y_{\ell m}(\theta, \phi)$, and the subscript b is used to label the exit channels in ψ_{final} . The radial wavefunctions reduce to the spherical Bessel functions far away from the scattering centre [34], so that

$$\lim_{r \rightarrow \infty} u_{\lambda}(r) = j_{\lambda}(kr) = (kr)^{\lambda} \left(-\frac{1}{(kr)} \frac{d}{d(kr)} \right)^{\lambda} \frac{\sin(kr)}{(kr)}. \quad (3.82)$$

⁴It is crucial to note that only a limited number of angular momentum values can be carried by the incoming particles, because the interaction potential is localized, if this were not the case, the expansion would be less useful as we would end up with an infinite series of partial waves to sum over. Having a characteristic length scale for the potential means we can impose the condition $d < r_0$ where r_0 reflects the size of the potential in some sense and therefore only the first few terms of the expansion contribute to the wavefunction.

If the target and the beam were both unpolarized, the sum over μ removes all contributions from functions with $\mu \neq 0$. The spherical harmonics then reduce to the Legendre polynomials and the scattering amplitude depends only on θ ,

$$\psi_{initial} = \sum_{\lambda=0}^{\ell} c_{\lambda} u_{\lambda}(r) P_{\lambda}(\cos\theta) \quad (3.83)$$

$$\psi_{final} = f_b(\theta) \sum_{\lambda=0}^{\ell} d_{\lambda} u_{\lambda}(r) P_{\lambda}(\cos\theta). \quad (3.84)$$

3.6.4 Direct Nuclear Reactions for Experiments

As mentioned previously, direct nuclear reactions such as $^{16}\text{O}(^3\text{He}, ^4\text{He})^{15}\text{O}$ occur over short time scales and only involve excitations of a few degrees of freedom in the target. This greatly simplifies analysis, while simultaneously allowing a good selectivity in the production of excited states. Frequently we are interested in cases of nucleon transfer such as pick-up reactions (p, d), ($^3\text{He}, \alpha$), (p, t), etc., and stripping reactions such as (d, p), ($\alpha, ^3\text{He}$), (d, n) and so on. Consider the $B(p, d)A$ reaction, in which the nucleus A forms a closed shell with respect to neutrons. In such cases it is useful to regard the target as the product nucleus A with an extra neutron in the next shell. In other words B can be represented as

$$|B\rangle = |A + \psi_n\rangle, \quad (3.85)$$

where $|\psi_n\rangle$ describes a neutron in the next available single particle state. To determine the transition probability we need only calculate the matrix

element

$$\langle f|V_\alpha|i\rangle = \langle A + d|V_\alpha|B + p\rangle \quad (3.86)$$

$$= \langle A + d|V_\alpha|A + \psi_n + p\rangle \quad (3.87)$$

$$= \langle d|V_\alpha|\psi_n + p\rangle. \quad (3.88)$$

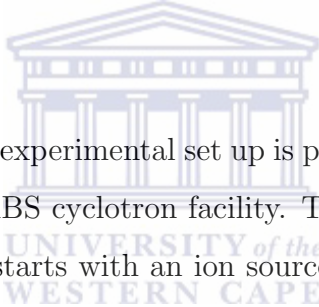
This kind of analysis is particularly useful for near closed shell nuclei, where direct nuclear reactions allow an examination of particle-hole excitations around the shell gaps.



Chapter 4

Apparatus and Design

Specifications



The Doppler shift lifetime experimental set up is planned to be located at the G-line of the iThemba LABS cyclotron facility. The process of generating a beam at iThemba LABS starts with an ion source which feeds positive ions into one of two solid pole cyclotrons. These are called the SPC1 and SPC2 units shown in figure 4.1, which accelerate the charged particle beam up to around $K = 8$ in energy before it is injected into the $K = 200$ separated sector cyclotron shown in figure 4.2. From there the beam is guided down the beam line by a series of bending and focusing magnets to one of several vaults used for either isotope production, radiotherapy or nuclear physics experiments, such as lifetime measurements.

Before describing the design considerations of our set up, I briefly discuss some of the techniques used for lifetime measurements in nuclear physics.

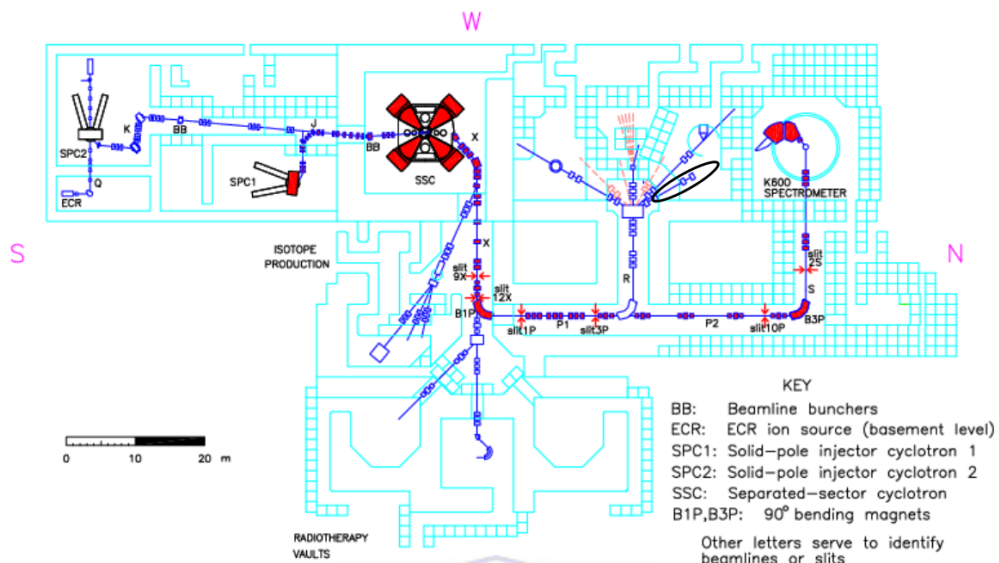


Figure 4.1: Floor plan of the iThemba LABS facility showing the SPC1 and SPC2 units and SSC. The G-line is circled in black.

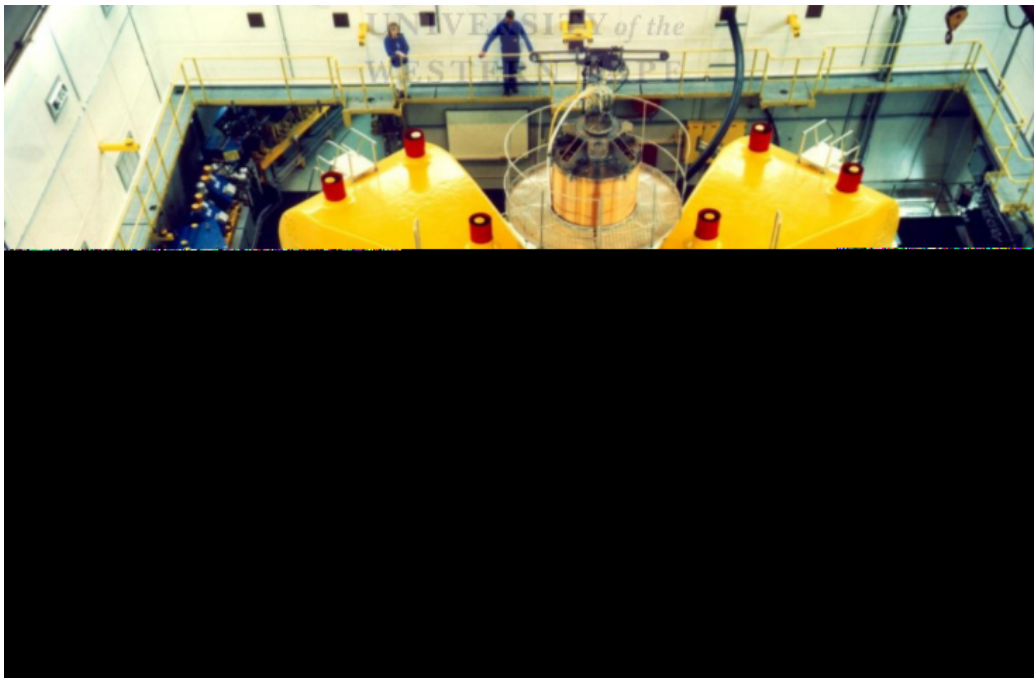


Figure 4.2: The separated sector cyclotron (SSC) from above.

4.1 Techniques

Nuclear lifetimes span a vast range of time scales from attoseconds (10^{-18} s) to billions of years, necessitating a variety of techniques for nuclear lifetime measurements. I describe below three popular techniques for measuring short lifetimes.

4.1.1 Fast Electronic Timing

For lifetimes of the order of nanoseconds or even several hundred picoseconds, fast electronics is sufficient to make the measurements. This method is based on a fast timing measurement of the delay between the production of an excited state and the detection of γ rays (following de-excitation) in a detector that ideally has fast response and good timing resolution. This requires precise measurements of the time difference between a beam pulse event on the target and a γ -ray detection event. Taking several such measurements and collating the data gives a distribution which can be fitted with the well known exponential decay law:

$$A(t) = A_0 e^{-t/\tau}, \quad (4.1)$$

where t is the time elapsed since the population of the state, A_0 is a normalization and τ , a free parameter, is the lifetime of the state [37].

4.1.2 Recoil Distance Doppler Shift

The Recoil Distance Doppler Shift method (RDDS) is used for measuring nuclear level lifetimes ranging from a few picoseconds up to several hundred picoseconds. The method relies on detecting γ rays from a nuclear reaction

while the nucleus is in motion or after it has stopped. For such measurements, a thin target is used in the reaction so that the recoils decay outside the target. Some distance away a thick foil is used to stop the recoiling nuclei. The de-excitation photons are then detected in a high purity germanium (HPGe) crystal as shown in figure 4.3.

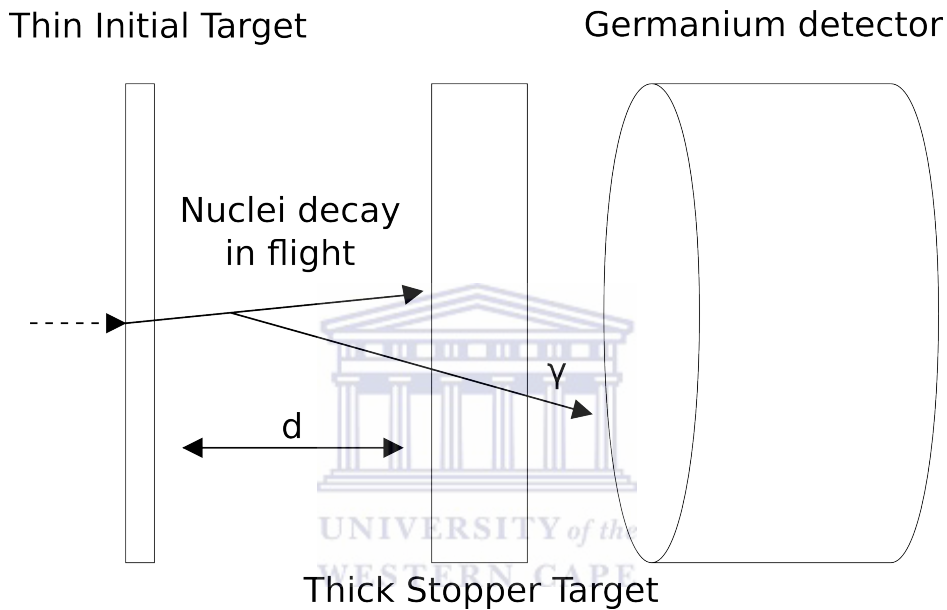


Figure 4.3: Schematic of the Recoil Distance Doppler Shift method. The recoil distance is labelled d .

If the decay takes place while the recoils are in flight between the target and stopper foil, the γ -ray energy will be Doppler shifted. On the other hand, if the decay happens once the nuclei have come to a stop, there will be no Doppler shift. If the lifetime of the excited state is greater than the stopping time then the two peaks can be resolved reasonably well, and the recoil velocity can be determined from the energy shift [37]. By measuring the relative intensities in the two peaks as a function of a variable recoil distance d , one can reliably extract the unknown lifetime τ .

4.1.3 Doppler Shift Attenuation Method

The Doppler Shift Attenuation Method (DSAM) is a technique for measuring nuclear lifetimes from a few femtoseconds up to a few picoseconds. The

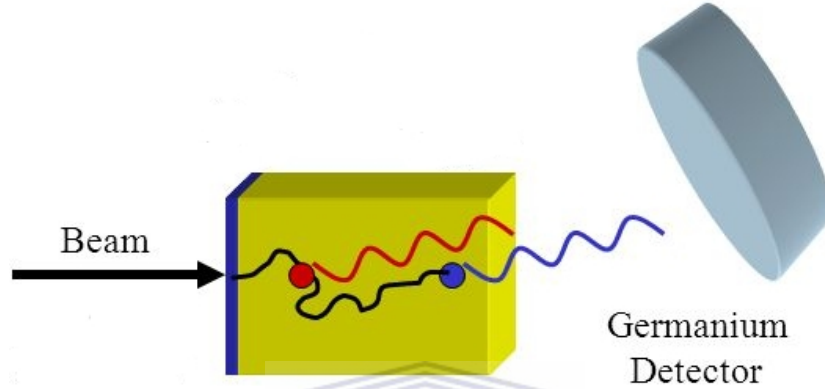


Figure 4.4: Schematic of a DSAM experiment where the nucleus de-excites while recoiling in the stopping medium.

method relies on detecting Doppler shifted γ rays emitted from a recoiling nucleus that is produced in a nuclear reaction. As the excited nucleus recoils in a stopping medium (shown in figure 5.3), the recoil velocity varies with time until the instant the γ ray is emitted. This implies that the Doppler shift is related to the lifetime. The Doppler shifted energy E_γ is dependent on the energy loss of the recoils in the medium prior to photon emission

$$E_\gamma = E_0 \frac{\sqrt{1 - F^2(\tau)\beta^2}}{1 - F(\tau)\beta\cos\theta}, \quad (4.2)$$

where E_0 is the unshifted energy and θ is the angle between the momenta of the recoiling nucleus and the detected γ -ray. In the above, $F(\tau)$ is an attenuation factor that is related to the lifetime by

$$F(\tau) = \frac{\int e^{t/\tau} v(t) \cos\zeta dt}{v_0\tau}, \quad (4.3)$$

where ζ is the angular spread in the recoil velocity [8]. Therefore the lifetime τ can be obtained with careful analysis of the lineshape of the measured γ ray or the centroid shift of the γ -ray peak, provided the detector response is well understood at that energy. A lineshape analysis offers less reliance on the detector resolution and the requirement for high statistics in the γ -ray peak of interest as opposed to the centroid-shift method. Additionally, an accurate understanding of the energy loss mechanism is very important to extract nuclear level lifetimes using this method. It is important that the recoils stop in the target backing, which is by necessity thick and of high Z material. Care also must be taken that the recoils do not stop too quickly so that a large fraction of the decays do not occur before losing significant kinetic energy [37, 32]. Below I discuss our design for fs-level lifetime measurements using the DSA method.

4.2 Design specifications

As mentioned in Chapter 3, Section 3.5, the only conclusive measurement of the lifetime of the 6791 keV state in ^{15}O was carried out by Bertone *et al.* using a $^{14}\text{N}(p, \gamma)$ reaction in direct kinematics with 300 keV protons [8]. Consequently, this experiment relied on the Doppler shift attenuation method with low recoil energies. It is well established that the stopping powers are not accurately known at such low energies. Ideally, the lifetime ought to be measured using an inverse kinematic reaction due to the obvious advantages listed below.

1. Higher recoil energies from inverse kinematics ensure that the recoiling nuclei are predominantly under the influence of electronic stopping. Unlike nuclear stopping, which plays a role at lower energies, electronic

stopping does not cause large angle scattering, and is much better understood.

2. Higher recoil velocities that are forwardly peaked produce larger Doppler shifts and greater sensitivity. Additionally, short-lived states in high velocity recoiling nuclei will all have decayed by the time nuclear stopping begins to play a role.

It was also mentioned previously, that we aim to produce the subthreshold state in ^{15}O at 6791 keV using a $^{16}\text{O}(^3\text{He}, \alpha)$ reaction in inverse kinematics. This is similar to work done previously [32], and the design is very similar to ones used before at TRIUMF [32] and Chalk River Laboratories [38]. In the reaction, a heavy ion ^{16}O beam will be bombarded on a ^3He target implanted on a thick foil, such as Au or Zr. The reaction produces a light ejectile (an α particle) that can be tagged by a $(\Delta E - E)$ silicon telescope, provided the E detector is thick enough to fully stop the light ejectiles of interest. This arrangement allows one to gate on the excited state of interest, minimizing systematic effects due to γ -ray feeding from higher lying states. The ^{15}O nucleus recoils within the target, emitting a Doppler shifted γ ray which will be detected by a high purity germanium detector placed at 0° to the beam for maximal sensitivity.

I discuss the vacuum system and design specifications of the scattering chamber at the G-line below.

4.2.1 Vacuum System

It is easy to see why a vacuum system is needed to transport the beam to the target, as high particle densities lead to high interaction probabilities and short mean free paths. For the purposes of beam transport particle

densities around 10^9 cm^{-3} with cross sections around 10^{-14} cm^2 are sufficient to produce a mean free path on the order of 10^3 m . This criterion corresponds to pressures of $\sim 10^{-7} \text{ mbar}$. However, beam transport is not the only motivation for using a high vacuum system, as contaminants in the vacuum chamber may condense on the target resulting in unwanted fusion evaporation reactions. For this reason it is important to achieve a vacuum better than $\sim 10^{-7} \text{ mbar}$ in the scattering chamber for precise lifetime measurements. Vacuum considerations in the proposed beamline are discussed below.

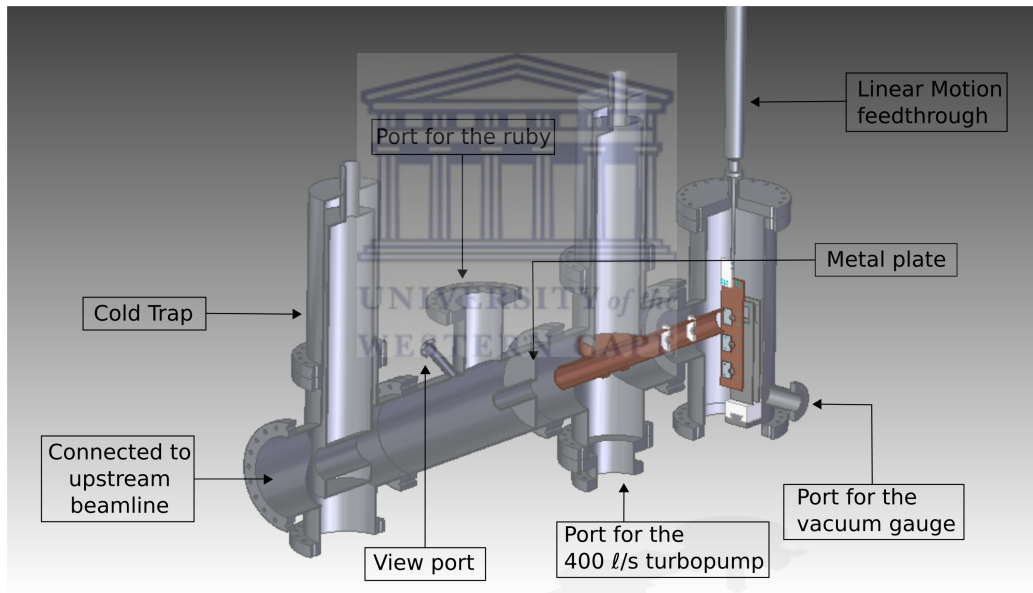


Figure 4.5: Full design done in Solid Edge (ST6). We use CF flanges everywhere for high vacuum.

4.2.2 Pumps and Gauges

Since there are no pumps capable of pumping across all pressure ranges, the pumping on the beamline must be done in stages. Pressures down to 10^{-3} mbar are considered rough vacuum. Various pumps are capable of pumping down to these pressures. In our set up it is planned to use a 110 ℓ/s dry scroll pump as the first stage of pumping. The lack of oil in such pumps reduces contaminants in the vacuum system. The second stage of pumping will use a 400 ℓ/s turbopump which would take the pressure down to $\sim 10^{-9}$ mbar. As shown in figure 4.5, the design also includes a metal plate, with a small aperture and length of pipe 6 cm long with a inner diameter of 3 cm, between the last two sections of the set up and the rest of the beam line. This is intended to produce low pumping speeds across the plate, which effectively reduces the volume that needs to be pumped by the main turbo pump in the vicinity of the target. The upstream part of the beamline will be pumped by a 150 ℓ/s turbopump. The design also makes provision for an inverted magnetron vacuum gauge to be attached as close to the target as possible to monitor the vacuum at the reaction site.

Since the roughing pumps upstream of the set up are not oil free, two cryogenic systems have been put into the design. A cold trap will be placed upstream of the rest of the set up and a cold shroud placed just upstream of the target. Both are introduced in order to condense hydrocarbon vapours and other possible contaminants out of the vacuum. The cold shroud also serves a second purpose related to the target heating which is explained in the following section.

4.2.3 Target Holder and Cooling Arrangement

It was mentioned before that the experiment requires implanted ^3He targets on thick foils of high Z stopping material. While these implanted targets are stable at room temperature, they are known to outgas with beam heating. In our design, as shown in figure 4.6, the targets are sandwiched between target frames and the target ladder which can hold up to three targets. In our design the beam stops fully in the gold backing. The target ladder will be mounted on a manual linear motion feed-through to provide precise control of the position of the targets.

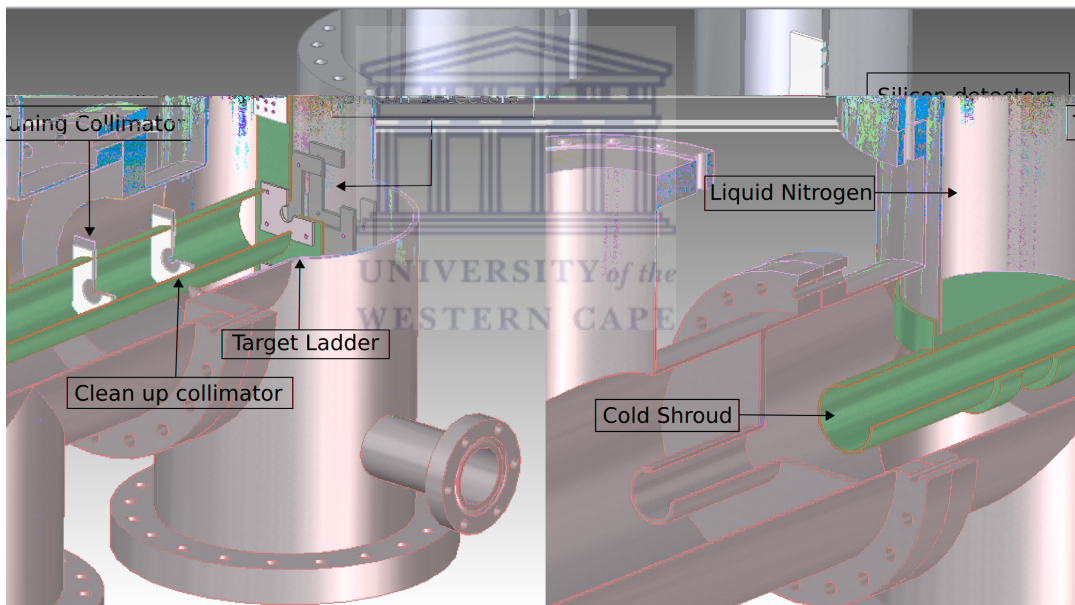


Figure 4.6: Close up view of the design. All copper parts are to be made of oxygen free high conductivity copper. The white plates are ceramic insulators to electrically isolate the collimators and target ladder.

4.2.4 Target Heating

The power delivered by the beam depends on the energy of the beam and the beam current. In our design, the beam spot is expected to have a diameter of about 3 mm while the targets will have effective diameters of 10 mm. Therefore, the full power of the beam will be absorbed by the implanted region of the target. Assuming radial heat conduction, one can calculate the temperature gradient in the material

$$\frac{dT}{dr} = \frac{P}{\kappa A}, \quad (4.4)$$

where P is the beam power, κ is the thermal conductivity of the material in $\text{Wm}^{-1}\text{K}^{-1}$ and A is the cross sectional area through which the heat flows. The temperature difference can be found trivially,

$$\Delta T = \int_{r_i}^{r_o} \frac{P dr}{\kappa 2\pi r t}, \quad (4.5)$$

$$= \frac{P}{\kappa 2\pi t} \ln \frac{r_o}{r_i}, \quad (4.6)$$

where A is expressed as $2\pi r$ multiplied by the target thickness t . Table 4.1

Table 4.1: Comparison of heating in different target materials.

Material	$\kappa[\text{Wm}^{-1}\text{K}^{-1}]$	$\Delta T[\text{K}]$
Au	318	12.05
Zr	22.6	169.57

shows an estimate of the temperature gradient for 25 μm thick Au and Zr foils, assuming a 10 pA, 50 MeV beam hits the centre of the target and the temperature remains constant over the beam spot. To minimize the effects of outgassing of the implanted helium due to the beam, the cold shroud is

designed to be placed in thermal contact with the target ladder using copper braids. It is however, important that the target ladder is slightly warmer than the cold shroud so that contaminants do not condense on the targets. To estimate this effect I performed a finite element analysis using Solid Edge to estimate the temperature gradient along the cold shroud. The results show that the cold shroud is approximately 4 K cooler near the contact on the LN₂ tank than at the edge near the target. The visual output of this simulation is shown in figure 4.7. The copper braids will surely not conduct as much, guaranteeing that the target ladder will not be as cold as the shroud.

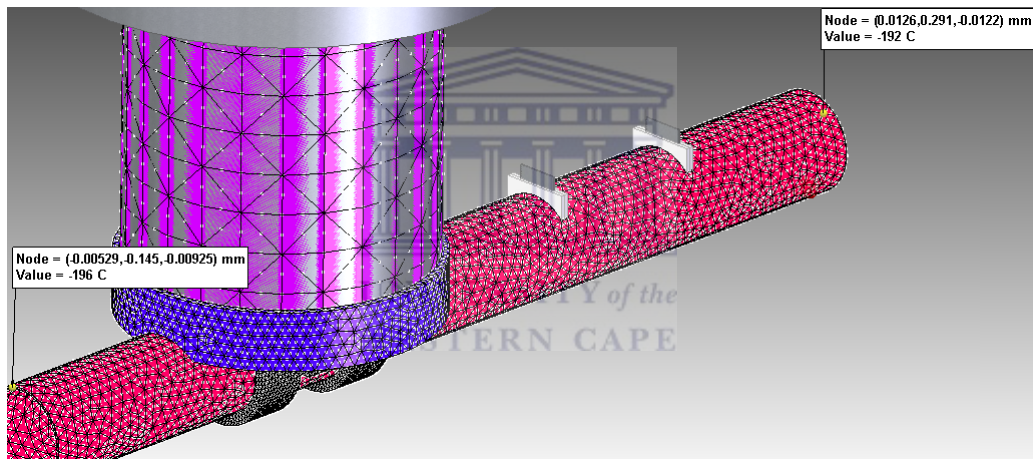


Figure 4.7: Heat transfer simulation performed in Solid Edge.

4.2.5 Beam Tuning

The design allows the beam to be tuned using a combination of a ruby upstream of the cold shroud (figure 4.5) and a pair of collimators mounted in the cold shroud (shown in figure 4.6). As the ruby scintillator needs to be observed with a camera while tuning the beam, a view port has been included

for this purpose. The ruby is placed further upstream of the silicon detectors to minimize stray radiation reaching the silicon detectors. It is planned that the beam will be tuned by minimizing the current on the defining and clean up collimators¹, while maximising the current on the target ladder. This requires the collimators and target ladder to be electrically isolated from the rest of the chamber.



¹The collimator arrangement is designed so that halo effects are minimal

Chapter 5

Monte Carlo Simulations

Simulations play a crucial role in scientific investigations across all fields. For the purposes of experimental nuclear physics, computer simulations are often used as tools to better understand systematic effects, make predictions of experimental data and fine tune experimental design based on these predictions. In the following sections I describe some Monte Carlo simulations that I have developed for the anticipated ${}^3\text{He}({}^{16}\text{O}, {}^{15}\text{O}){}^4\text{He}$ experiment to measure the ~ 1 fs lifetime of the subthreshold state in ${}^{15}\text{O}$ at 6.8 MeV using the DSA method. The simulations will be used to optimize the experimental set up for both γ -detection efficiency, as well as the γ -ray lineshape, that will eventually be used to extract the lifetime.

The simulation procedure consists of three important subgroups:

1. Calculation of reaction kinematics.
2. Randomization and selection of recoil and ejectile momenta.
3. Calculation of the γ -ray lineshape.
4. Incorporation of the above into a Geant4 code to incorporate γ -ray detection efficiencies.

5.1 Monte Carlo Methods

Since observables can never be specified with infinite precision, simulating natural processes requires one to work with the statistical properties of a population with an assumed inherent randomness. For example, the direction of a γ ray from a radioactive decay cannot be known *a priori*. As a result, simulating a radioactive decay requires picking the direction of a photon at random with known probability for each direction. This process is repeated for a large number of particles in an ensemble and is called the Monte Carlo method.

The defining characteristic of Monte Carlo methods is the use of random numbers within a computer program. This program is equipped with a (pseudo) random number generator that generates random numbers within the interval $(0, 1)$. In general, the probability of uniformly generating a random number in the interval $(x, x + dx)$ is

$$p(x)dx = dx, \tag{5.1}$$

when $0 < x < 1$ and 0 otherwise. The function $p(x)$ is called the probability distribution function of x . Given a function $y(x)$, the probability distribution of y must satisfy

$$|p(y)dy| = |p(x)dx| \tag{5.2}$$

$$p(y) = p(x) \left| \frac{dx}{dy} \right|, \tag{5.3}$$

by the fundamental transformation law of probabilities [39]. If $p(y)$ is an

arbitrary probability density function $f(y)$, then the above gives

$$p(x) \frac{dx}{dy} = f(y) \quad (5.4)$$

$$\int_{-\infty}^x p(x) dx = \int_{-\infty}^{y'} f(y) dy \quad (5.5)$$

$$x = \mathcal{F}(y'), \quad (5.6)$$

where \mathcal{F} is known as the cumulative density function of y and $p(x) = 1$ for

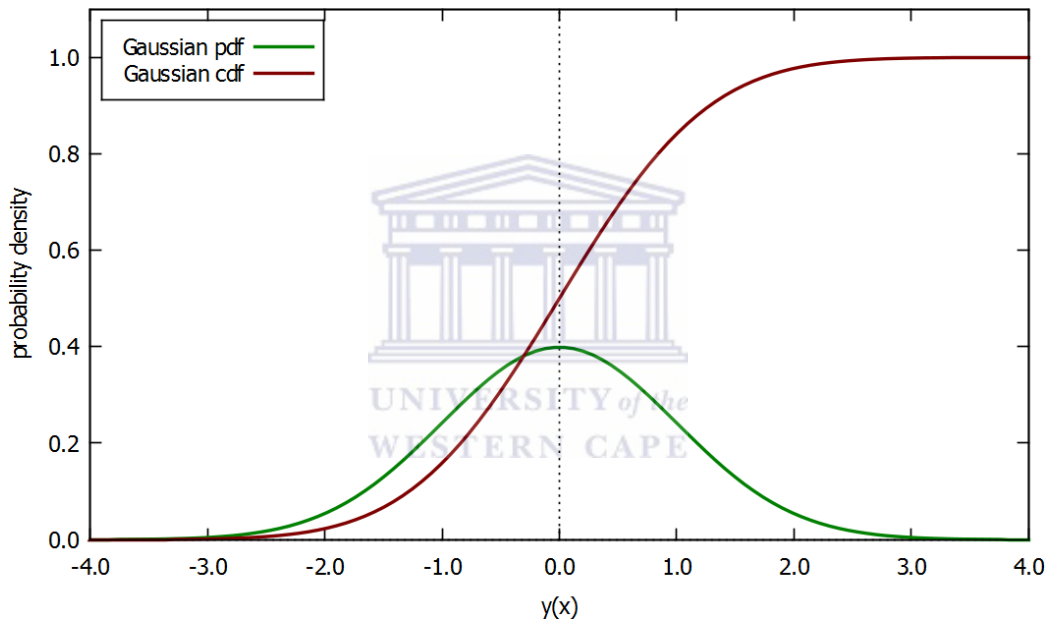


Figure 5.1: A Gaussian probability density function $f(y)$ (green) with its cumulative density function $\mathcal{F}(y)$ (red).

$x \in (0, 1)$ and zero elsewhere. This gives $\mathcal{F}^{-1}(x)$ that will generate random deviates y that follow the distribution $f(y)$. This is the concept behind the inverse transform method of generating random deviates from a given probability distribution function. Geometrically, $\mathcal{F}(y)$ can be interpreted as the probability of randomly selecting a number from the distribution which is less than y . The inverse transformation is now the same as picking a uniform random x in $(0, 1)$ and finding $y(x)$ such that the $\mathcal{F}(y) = x$. This can be

seen by looking at a particular example shown in figure 5.1.

It should be noted that the Gaussian distribution pictured in figure 5.1 is one example where the inverse transform method to generate a single Gaussian variate is not trivial¹. Fortunately the distribution can be obtained using a generalization with multiple variates [39]. If $x_1, x_2, x_3, \dots, x_n$ are random deviates with a joint probability distribution $p(x_1, x_2, x_3, \dots, x_n)$ and $y_1, y_2, y_3, \dots, y_n$ are all functions of the x 's, then the joint probability distribution of the y 's is given by the product of $p(x_1, x_2, x_3, \dots, x_n)$ with the Jacobian determinant of the x 's with respect to the y 's

$$p(y_1, \dots, y_n) dy_1 \dots dy_n = p(x_1, \dots, x_n) \begin{vmatrix} \frac{\partial x_1}{\partial y_1} & \dots & \frac{\partial x_1}{\partial y_n} \\ \vdots & & \vdots \\ \frac{\partial x_n}{\partial y_1} & \dots & \frac{\partial x_n}{\partial y_n} \end{vmatrix} dy_1 \dots dy_n. \quad (5.7)$$

This forms the basis of the Box-Müller transform used to generate pairs of normally distributed variates. The use of this method for our purposes is described in more detail later in this chapter.

5.2 Simulations for ${}^3\text{He}({}^{16}\text{O}, {}^{15}\text{O}){}^4\text{He}$

5.2.1 Reaction Kinematics

The first step in our simulations is an accurate determination of the recoil and ejectile kinematics for a 50 MeV ${}^{16}\text{O}$ beam incident on a ${}^3\text{He}$ target. Once the initial values of the ejectile and recoil momenta are determined, they will eventually be tracked in a Geant4 simulation code to determine the Doppler effects. Since the proposed reaction is in inverse kinematics, with

¹This is because the inverse of the cdf for the Gaussian distribution is calculated numerically which can become computationally taxing.

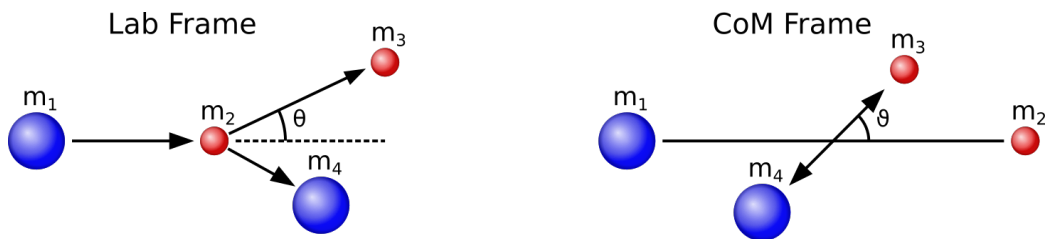


Figure 5.2: The sum of the momenta in the centre of mass frame is always 0, which greatly simplifies analysis.

a relatively high beam energies, it is best that the kinematics be calculated relativistically for a generic lineshape simulation which correctly calculates all recoil velocities. It is useful to analyse this problem in the centre of mass frame, where $\sum_i \mathbf{p}_i = 0$. Figure 5.2 illustrates the difference between the laboratory and centre of mass frames. In what follows, subscripts 1 to 4 denote the projectile, target, ejectile and recoil respectively. Greek subscripts denote 4-vectors following the Einstein summation convention, primed symbols are taken to be in the centre of mass frame and we set $c = 1$ for convenience. For such a reaction shown in figure 5.2, the square of invariant mass of the system before the collision in the lab frame is

$$s_{Lab} = p^\mu p_\mu \quad (5.8)$$

$$= (E_1 + E_2)^2 - (\mathbf{p}_1 + \mathbf{p}_2)^2 \quad (5.9)$$

$$= (E_{beam} + m_1 + m_2)^2 - (E_{beam} + m_1)^2 - m_2^2 \quad (5.10)$$

$$= (m_1 + m_2)^2 + 2m_2 E_{beam}. \quad (5.11)$$

Similarly, in the centre of mass frame

$$s_{CoM} = p'^{\mu} p'_{\mu} \quad (5.12)$$

$$= (E'_1 + E'_2)^2 \quad (5.13)$$

$$= \left[\sqrt{m_1^2 + \mathbf{p}'_1{}^2} + \sqrt{m_2^2 + \mathbf{p}'_2{}^2} \right]^2. \quad (5.14)$$

Since by definition $\mathbf{p}'_1{}^2 = \mathbf{p}'_2{}^2 = \mathbf{p}'^2$, these subscripts can be dropped and an expression for p' can be obtained by equating the two expressions above .

$$s_{Lab} = s_{CoM} \quad (5.15)$$

$$s_{Lab} = m_1^2 + m_2^2 + 2\mathbf{p}'^2 + 2\sqrt{m_1^2 + \mathbf{p}'^2} \sqrt{m_2^2 + \mathbf{p}'^2} \quad (5.16)$$

$$s_{Lab} - m_1^2 - m_2^2 - 2\mathbf{p}'^2 = 2\sqrt{m_1^2 + \mathbf{p}'^2} \sqrt{m_2^2 + \mathbf{p}'^2} \quad (5.17)$$

$$(s_{Lab} - m_1^2 - m_2^2)^2 + 4\mathbf{p}'^4 = 4\mathbf{p}'^2 (s_{Lab} - m_1^2 - m_2^2) + 4(m_1^2 m_2^2 + m_1^2 \mathbf{p}'^2 + m_2^2 \mathbf{p}'^2 + \mathbf{p}'^4)$$

$$(s_{Lab} - m_1^2 - m_2^2)^2 = 4\mathbf{p}'^2 s_{Lab} + 4m_1^2 m_2^2 \quad (5.18)$$

$$\sqrt{\frac{(s_{Lab} - m_1^2 - m_2^2)^2 - 4m_1^2 m_2^2}{4s_{Lab}}} = p'. \quad (5.19)$$

Since s is conserved we also have

$$s_{CoM} = p'^{\mu} p'_{\mu} \quad (5.20)$$

$$= (E'_3 + E'_4)^2 \quad (5.21)$$

$$= \left[\sqrt{m_3^2 + \mathbf{p}'_3{}^2} + \sqrt{m_4^2 + \mathbf{p}'_4{}^2} \right]^2, \quad (5.22)$$

after the collision and similar to before $\mathbf{p}'_3 = \mathbf{p}'_4 = \mathbf{p}'_a$, so that

$$p'_a = \sqrt{\frac{(s_{Lab} - m_3^2 - m_4^2)^2 - 4m_3^2m_4^2}{4s_{Lab}}}, \quad (5.23)$$

where the subscript 'a' represents 'after' the collision. We can now find the velocity of the centre of mass frame v_{cm} with the Lorentz boost.

$$p_2'^{\mu} = \Lambda_{\nu}^{\mu} p^{\nu} \quad (5.24)$$

$$\begin{pmatrix} E_2' \\ 0 \\ 0 \\ p' \end{pmatrix} = \begin{pmatrix} \gamma & 0 & 0 & -\gamma\beta \\ 0 & 1 & 0 & 0 \\ 0 & 0 & 1 & 0 \\ -\gamma\beta & 0 & 0 & \gamma \end{pmatrix} \begin{pmatrix} m_2 \\ 0 \\ 0 \\ 0 \end{pmatrix}, \quad (5.25)$$

where $\beta = \frac{v_{cm}}{c}$ and $\gamma = (1 - \beta^2)^{-\frac{1}{2}}$. As p'_3 is already known, for a given scattering angle θ'_3 in the centre of mass frame it is easy to calculate $\mathbf{p}_3, \mathbf{p}_4, E_3, E_4$ and θ_4 using a combination of projections onto the z -axis and xy -plane, and the Lorentz transformation equations [40]. However, for our purposes it is more useful to work with quantities in the laboratory frame. In such cases the above has only limited use. Instead, the energy of the ejectile in the laboratory frame

$$E_3 = \gamma E_3' - \gamma\beta p_3' \cos \theta'_3, \quad (5.26)$$

must be expressed in terms of the laboratory scattering angle. After much tedious algebra the above can be rewritten as

$$\begin{aligned}
E_3 &= \frac{1}{E_t'^2 - p_1^2 \cos^2 \theta_3} \left[E_t \left(m_2 E_1 + \frac{m_1^2 + m_2^2 + m_3^2 - m_4^2}{2} \right) \right. \\
&\pm p_1 \cos \theta_3 \left\{ \left(m_2 E_1 + \frac{m_1^2 + m_2^2 - m_3^2 - m_4^2}{2} \right)^2 \right. \\
&\quad \left. \left. - m_3^2 m_4^2 - p_1^2 m_3^2 \sin^2 \theta_3 \right\}^{\frac{1}{2}} \right], \tag{5.27}
\end{aligned}$$

which expresses E_3 purely in terms of the masses, total energies E_t and E_t' , and the laboratory scattering angle θ_3 . The total energy in the centre of mass frame E_t' is the square root of the invariant mass obtained from Eq. (5.11). A close look at Eq.(5.27) shows that there may be two solutions for E_3 corresponding to positive and negative square roots. This depends on a quantity ζ

$$\zeta = \frac{p_1}{E_t} \left(\frac{1 + \frac{m_3^2 - m_4^2}{E_t'^2}}{\sqrt{\left[1 - \left(\frac{m_3 + m_4}{E_t'}\right)^2\right] \left[1 - \left(\frac{m_3 - m_4}{E_t'}\right)^2\right]}} \right). \tag{5.28}$$

If $\zeta > 1$, both solutions to Eq. (5.27) are valid because when v_{cm} is large enough, backward scattering angles in the centre of mass frame may correspond to forward angles in the laboratory frame. If $\zeta < 1$, only the solution corresponding to the positive square root is physically realistic. Clearly the value inside the square root in Eq. (5.27) cannot be negative and this condition is used in the kinematics code to check if θ_3 is a valid scattering angle. Since we want to express all quantities in the laboratory frame, the recoil

scattering angle is finally calculated using the relations

$$p_4 \sin \theta_4 = p_3 \sin \theta_3 \quad (5.29)$$

$$p_4 \cos \theta_4 = p_1 - p_3 \cos \theta_3. \quad (5.30)$$

These scattering angles are used to specify initial conditions in the simulation codes that are explained in the following sections.

5.2.2 DSAM Lineshape Code for ${}^3\text{He}({}^{16}\text{O}, {}^{15}\text{O}){}^4\text{He}$

In what follows I describe the DSAM code that I developed using the kinematics described above. The γ -ray lineshape is first simulated using a Monte Carlo code written in C++ (see appendix C), which is independent of γ -detection efficiency. Figure 5.3 is a schematic detailing the various parameters used in the simulation. For the sake of clarity, in the following sections the notation will match the labels in figure 5.3. In our new convention the subscripts 3 and 4 for the ejectile and recoil will be replaced by α and R respectively and the subscript γ will denote quantities related to the γ rays. In the code, the reaction is specified by the user, who supplies the A and Z values of the particles involved in the collision, as well as excitation and beam energies. Atomic masses are retrieved from a lookup table of mass excesses obtained from the Atomic Mass Data Centre [41] and converted to nuclear masses by subtracting Zm_e . These masses are used in conjunction with the excitation energy to find the Q -value of the reaction.

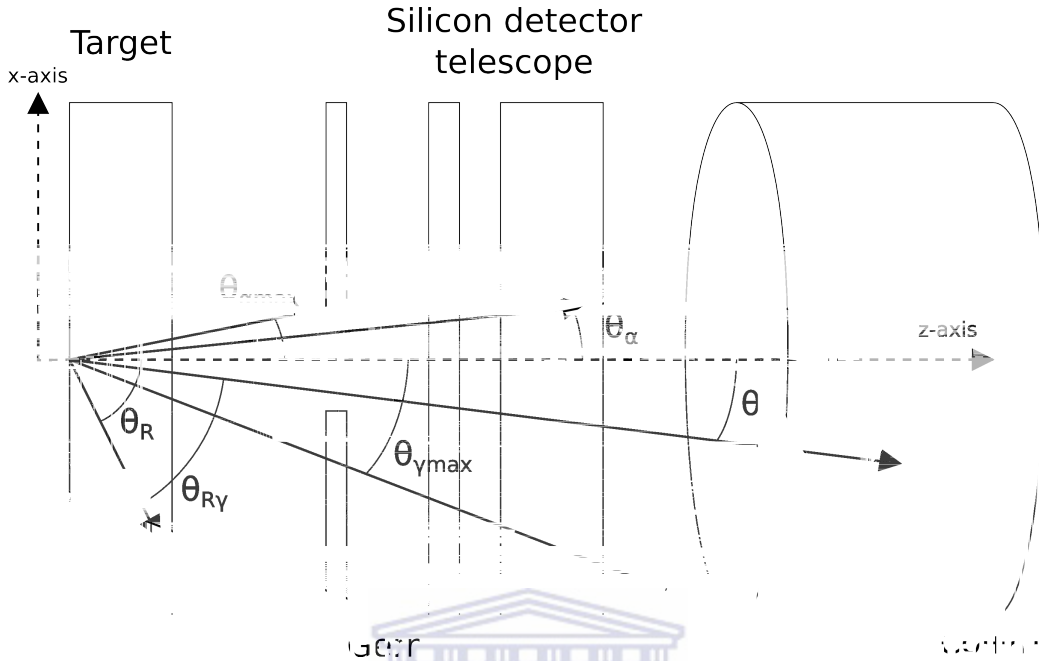


Figure 5.3: Schematic of the DSAM set up. The subscripts R and α label the ‘recoil’ and ‘ejectile’ respectively. The Germanium detector is placed at 0° to the beam for maximal sensitivity to Doppler shifts.

The use of randomized variables in the simulations

The code now chooses a random ejectile scattering angle θ_α in the laboratory frame² using the transformation

$$\theta_\alpha = \cos^{-1} [1 + (\cos \theta_{\alpha\max} - 1)u], \quad (5.31)$$

where the uniform random deviates $u \in (0, 1)$ generate various $\cos \theta_\alpha$ in the range³ $(\cos \theta_{\alpha\max}, 1)$.

In the next step the kinematics calculator is used to calculate the momenta and energies of the ejectile and recoil in the laboratory frame. This is

²As mentioned previously, $\theta_3 = \theta_\alpha$ for a $(^3\text{He}, \alpha)$ reaction.

³Since the kinematics is independent of the azimuthal angle ϕ_α they have been neglected here. However, in the Geant simulations described later this angle must be specified as part of the initial conditions.

done by starting with initial values of energies and momenta

$$E_1 = m_1 + E_{beam} \quad (5.32)$$

$$E_2 = m_2 \quad (5.33)$$

$$p_1 = \sqrt{E_1^2 - m_1^2}. \quad (5.34)$$

The total energy in the laboratory frame E_t is then just the sum of the energies E_1 and E_2 , whereas the total energy in the centre of mass frame E'_t is the square root of the invariant mass derived in Eqs. (5.11) and (5.14). After calculating the ejectile energy in the laboratory frame, the recoil energy E_4 is simply the difference between the total energy and the ejectile energy. Finally, the code calculates the recoil scattering angle for the predetermined θ_α from Eqs. (5.29) and (5.30). The recoil momentum and scattering angle are later used as initial values to calculate the energy loss of the recoil and subsequently the Doppler shift of the emitted γ ray as it moves through the target backing. Since the lifetime of the excited state follows the exponential probability distribution

$$p(t) = e^{-\frac{t}{\tau}}, \quad (5.35)$$

it has a cumulative density function

$$\mathcal{F} = \tau(1 - e^{-\frac{t}{\tau}}). \quad (5.36)$$

The above shows that random decay times t following an exponential distribution can be generated using the inverse transform $t = -\tau \ln(u)$ with uniform variates u in the range $(0, 1)$. For our simulations τ was chosen to be 1 fs. Once this procedure selects a random time of flight t prior to photon emission, θ_γ , the polar angle for the photon is randomized similar to the way

θ_α was generated with Eq. (5.31). This procedure speeds up computation time by selecting only those γ rays which hit a cylindrical HPGe detector shown in figure 5.3. The HPGe detector specifications were taken for a 100% relative efficiency n-type CANBERRA detector.

Finally, the azimuthal angles for the γ ray and recoil, ϕ_γ and ϕ_R , are independently chosen from a uniform distribution over the interval $(0, 2\pi)$. The recoil and γ momenta are now completely specified. The angle between the recoiling ^{15}O nucleus and the emitted photon is easily calculated by taking the scalar product⁴

$$\cos \theta_{\gamma R} = \frac{\mathbf{p}_\gamma \cdot \mathbf{p}_R}{|p_\gamma||p_R|}. \quad (5.37)$$

Once the randomized variables are obtained, the Doppler shift simulation was done independently using two approaches. In the first approach described below, the energy loss for the recoil prior to photon emission was calculated using a cubic spline interpolation discussed in appendix B, together with stopping powers obtained from SRIM2013 [42] for ^{15}O nuclei recoiling in Au. For these calculations, first the decay time t was divided into small time slices of width $dt = 10^{-6}\tau$. The initial value of the recoil kinetic energy T_R from the kinematics is converted into a velocity which is used to find the distance $\Delta x = v_R dt$ that the recoil travels in the first time interval. The spline interpolation described previously was used to obtain the stopping power $\left(\frac{dE}{dx}\right)$ for this value of T_R . Assuming that the stopping power is constant over the infinitesimal time dt , the energy lost in the time interval dt is then

$$\Delta E \simeq \left(\frac{dE}{dx}\right) \Delta x. \quad (5.38)$$

⁴The values of θ_R and \mathbf{p}_R are obtained from the kinematics code.

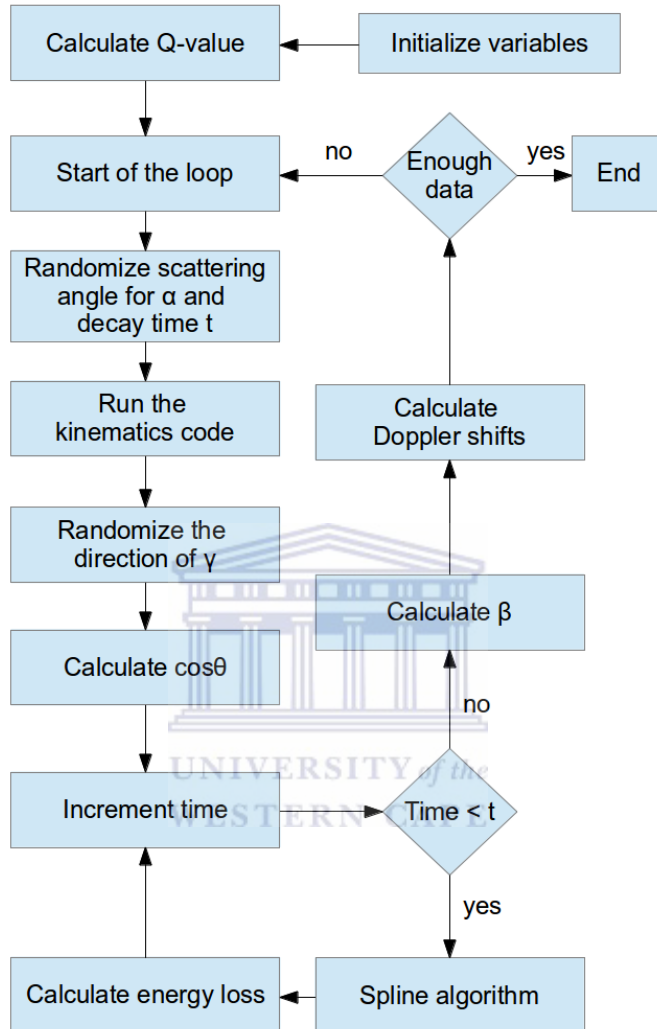


Figure 5.4: Outline of the flow through the Monte Carlo code.

This iterative procedure provides a new recoil kinetic energy $T'_R = T_R - \Delta E$ for the next time step. In this fashion the recoil is stepped through until time t , losing energy at each step. The final kinetic energy of the recoil T_R

after a time t has elapsed is then used to calculate

$$\beta = \frac{\sqrt{2m_4 T_R + T_R^2}}{E_R}, \quad (5.39)$$

which is $\approx 5\%$ for our reaction after the energy losses have been taken into account. The Doppler shifted γ -ray energy can finally be obtained using the formula

$$E_\gamma = E_0 \frac{\sqrt{1 - \beta^2}}{1 - \beta \cos \theta_{\gamma R}}, \quad (5.40)$$

with E_0 being the unshifted γ -ray energy. Figure 5.4 shows this general algorithm used for each event in the simulation.

These simulations were first used to investigate the effects of the collimator on lineshape. This was done by restricting the acceptance angle for ejectiles ($\theta_{\alpha max}$ in figure 5.3). The results are shown in figure 5.5. These sim-

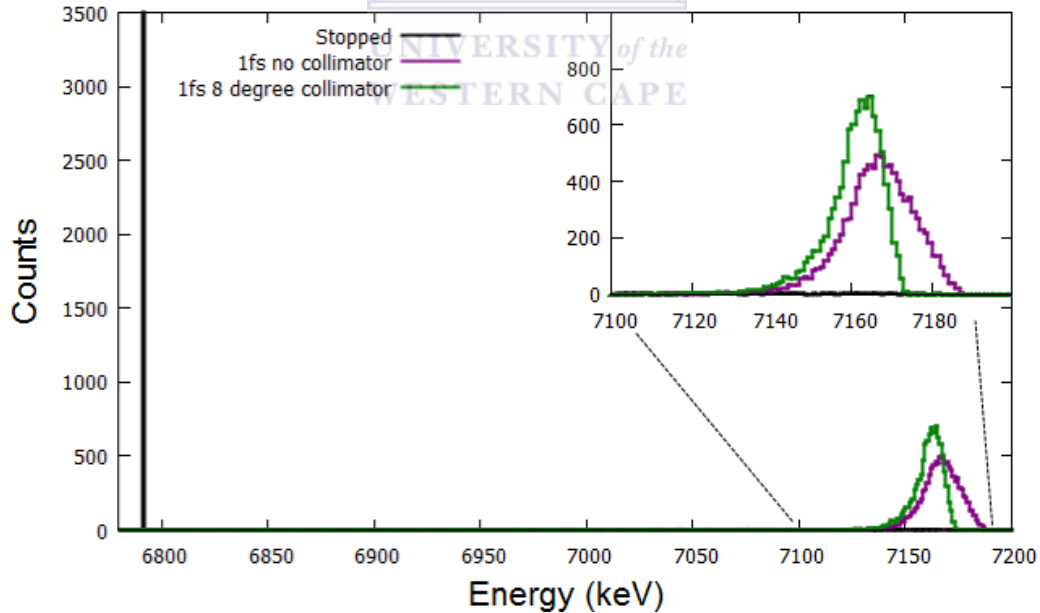


Figure 5.5: The effects of introducing a collimator (setting $\theta_{\alpha max} = 8^\circ$) on lineshape. A clearly asymmetric peak arises on using a collimator.

ulations were done with the detector distance fixed to 150 mm. It is obvious

that for $\tau = 1$ fs there is a clear enhancement in sensitivity to the γ ray lineshape from introducing a collimator for the light ejectiles. I also performed a set of simulations to investigate the effect of changing the target-detector distance while keeping the collimator fixed from the earlier simulation. This offers constraints on the acceptance angle for the γ rays ($\theta_{\gamma max}$ in figure 5.3), for different values of

$$\theta_{\gamma max} = \tan^{-1} \left(\frac{r_g}{d_g} \right), \quad (5.41)$$

where r_g is the radius of the crystal and d_g is the distance from the centre of the front face of the crystal to the target. The results are shown in figure 5.6 and also show a clear improvement in lineshape sensitivity at the cost of solid angle, which is not unexpected.



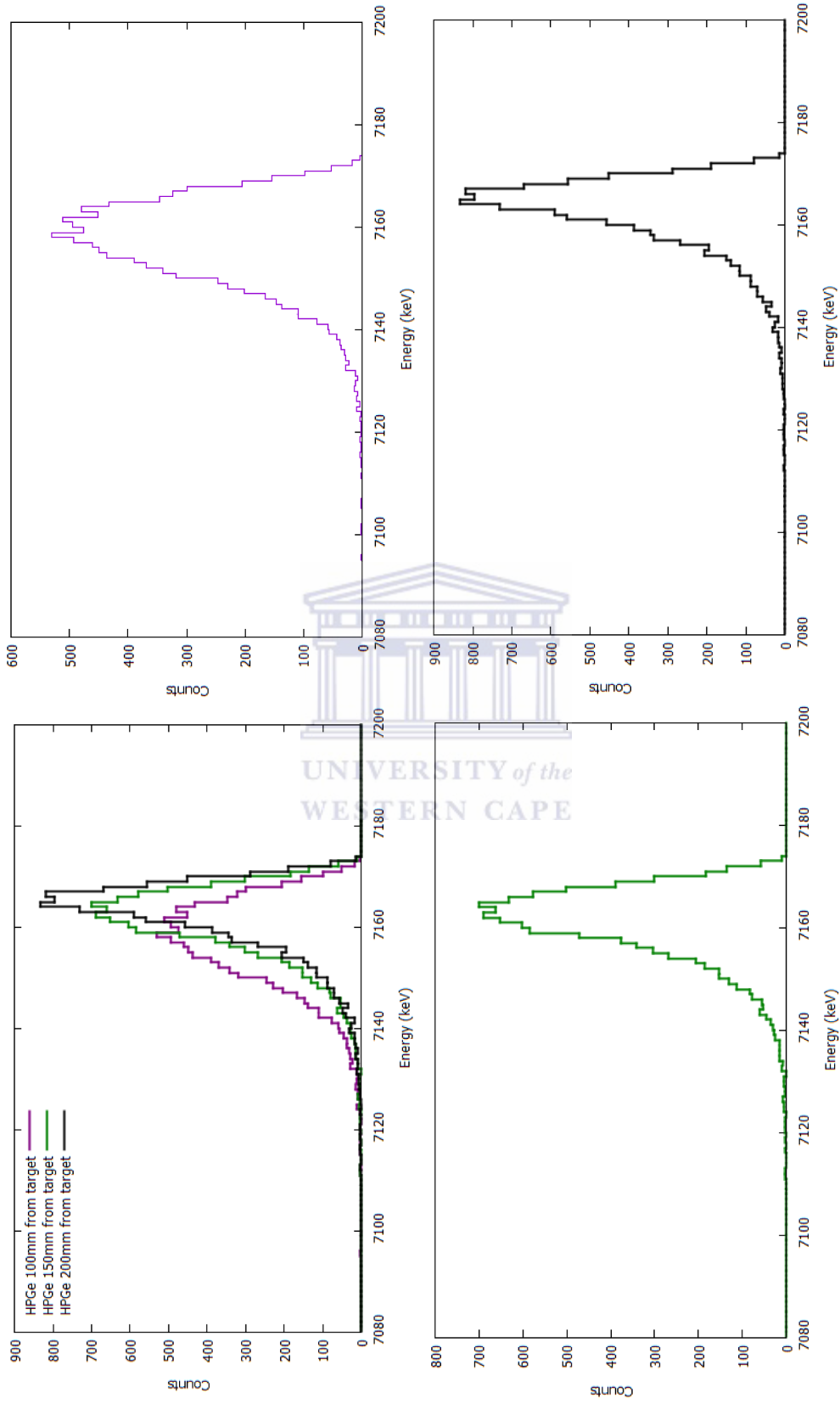


Figure 5.6: The effect of detector distance on lineshape. At the top left all 3 spectra are plotted on the same set of axes for easy comparison. The top right, bottom left and bottom right are individual spectra corresponding to detector distance of 100 mm, 150 mm and 200 mm respectively. The collimator acceptance angle is fixed for all these data at 8° .

Finally, the Doppler effects on varying the HPGe detector angle with respect to the beam axis were simulated to have a complete understanding of the sensitivity requirements for a $\tau = 1$ fs lifetime measurement. This was

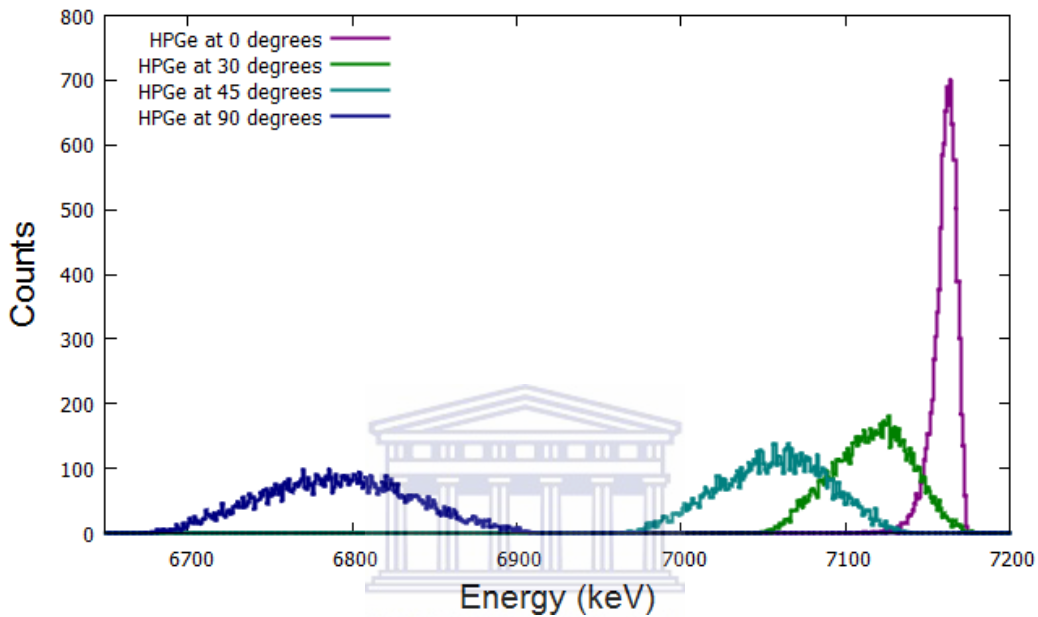


Figure 5.7: Lineshapes obtained for different HPGe detector angles with respect to the beam axis. The collimator angle is kept fixed for all simulations at 8° .

done by making a transformation

$$\begin{pmatrix} p'_{\gamma x} \\ p'_{\gamma y} \\ p'_{\gamma z} \end{pmatrix} = \begin{pmatrix} 1 & 0 & 0 \\ 0 & \cos \eta & \sin \eta \\ 0 & -\sin \eta & \cos \eta \end{pmatrix} \begin{pmatrix} p_{\gamma x} \\ p_{\gamma y} \\ p_{\gamma z} \end{pmatrix}, \quad (5.42)$$

for a general rotation angle η . These simulations were done for a fixed detector distance at 150 mm and θ_{max} set to 8° . The results, shown in figure 5.7, show that for short lifetimes the lineshape gets smeared out rather rapidly as the HPGe detector is moved off the beam axis. It is quite apparent that measuring a 1 fs lifetime requires the detector be placed at 0° to the beam

where sensitivity to the Doppler shift is maximal. Furthermore, restricting the acceptance angles for the ejectiles and γ rays also improves the sensitivity significantly. However this comes at a cost of efficiency, which has not been taken into consideration yet.

This was further investigated with a Geant simulation, which independently calculated the energy losses using its own libraries. The simulation is discussed below.

5.2.3 Geant4 Simulations

GEANT is an ongoing project with collaborators around the world. It provides a toolkit allowing users to model the GEometry ANd Transport of particles in various media. Geant4 is a C++ package which was developed from the earlier FORTRAN codes of GEANT3, allowing users the benefits of object oriented programming in the simulations [43].

Structure of a Geant4 Application

Geant4 provides various classes with the intention of separating the simulation into multiple parts. Thus, the general structure of an application is a single application file containing the `main()` function which initialises the run manager and handles user initialisations. The user is responsible for setting the conditions of a *run* after which the rest of the simulation is controlled through the run manager which takes control at the beginning of each *run*. A *run* is the largest subdivision of a simulation which consists of *events* corresponding to the physics involved in the process. The *events* themselves contain all the different particle *trajectories* that have been generated by the simulation. Finally, the *trajectories* record information from each *step* of the simulation and are each associated with a *particle* object.

I now briefly describe selected user defined classes derived from classes provided by the toolkit which are relevant to later discussions

1. the `DetectorConstruction` class

- defines the volumes in the geometry in terms of shape and placement
- assigns materials to volumes
- defines electromagnetic fields in the volumes
- registers volumes as detectors

2. the `PhysicsList` class

- defines the processes and interactions to be simulated

3. the `PrimaryGeneratorAction` class

- fetches definitions of the primary particles
- performs any calculations necessary to define the initial state of the primary particles
- sets the primary particles in motion at the beginning of each event

4. the `SteppingAction` class

- provides information on the status of the simulation at each step

5. the `RunAction` class

- Collects information from each *event* and allows recording of the events in real time.

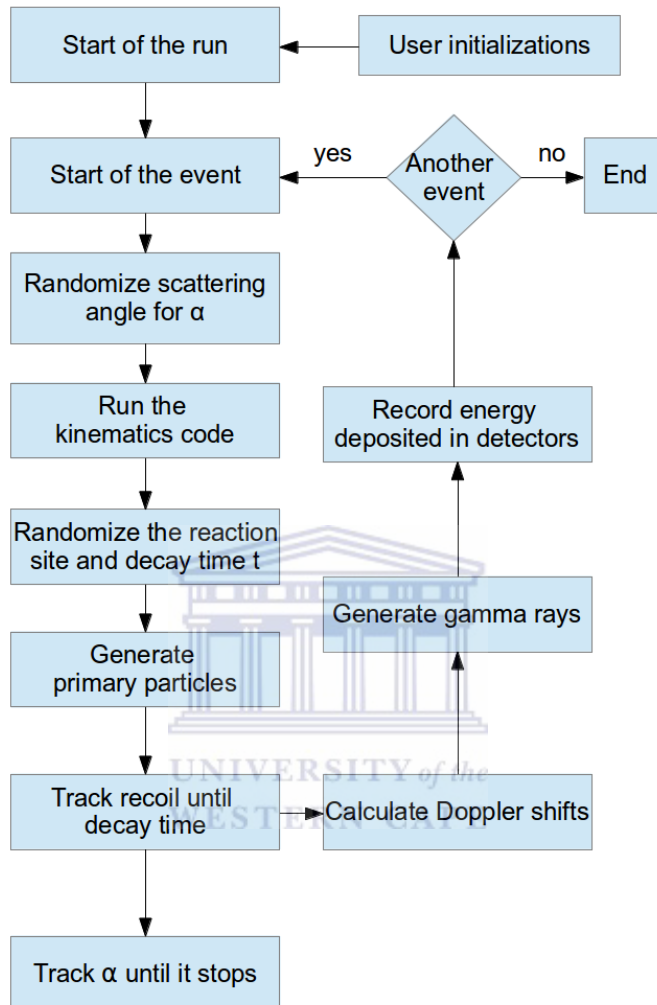


Figure 5.8: General outline of the flow through the Geant code while the simulation runs.

5.2.4 Lineshape and Efficiency Determination from Geant4

The algorithm for this part of the simulation is similar as before, with the main difference that the detection efficiencies and energy losses are determined from the Geant software itself. This minimizes our reliance on several

approximations. Figure 5.8 illustrates the general flow of this algorithm.

The `DetectorConstruction` and `PhysicsList` classes are called during the user initialization phase. A simplified geometry of the experimental set up used in the simulation is shown in figure 5.9. The scattering chamber was constructed as a steel tube with wall thickness matching that of the Solid Edge design (2.7 mm). The target was simplified to a gold disc of thickness $25\ \mu\text{m}$ and the $\Delta E - E$ telescope was constructed as a pair of silicon wafers with thickness $25\ \mu\text{m}$ and $500\ \mu\text{m}$. The germanium detector was constructed as a cylindrical crystal of radius 39 mm and length 79 mm with a 12 mm diameter hole up to a depth of 65 mm. This matches the manufacturer's specifications of a 100% n-type CANBERRA HPGe detector that has already been purchased and is planned to be used for the actual experiment. The germanium detector is enclosed in a 1.5 mm thick aluminium housing which is usual for such detectors. Several such geometries were constructed for varying collimator openings (for the ejectiles) and target to detector distances. For the data described in this section I used collimator apertures of 4.9 mm, 7.6 mm or 10.4 mm respectively, which correspond to acceptance angles of 7° , 11° or 15° for the α particles. The `PhysicsList` is constructed next, which includes electromagnetic interactions and decay events. Control is then passed to the user to set parameters for a *run*.

Once the user starts a *run* the simulation jumps straight into the first event. At the start of each event the `PrimaryGeneratorAction` looks up particle masses and randomizes variables similarly as explained in section 5.2.2 with a few important differences

1. the direction for each γ ray is chosen to be uniformly distributed over the full 4π solid angle so that the γ rays are emitted isotropically.
2. the centre of mass scattering angle for the ejectiles (θ'_α) is chosen sim-

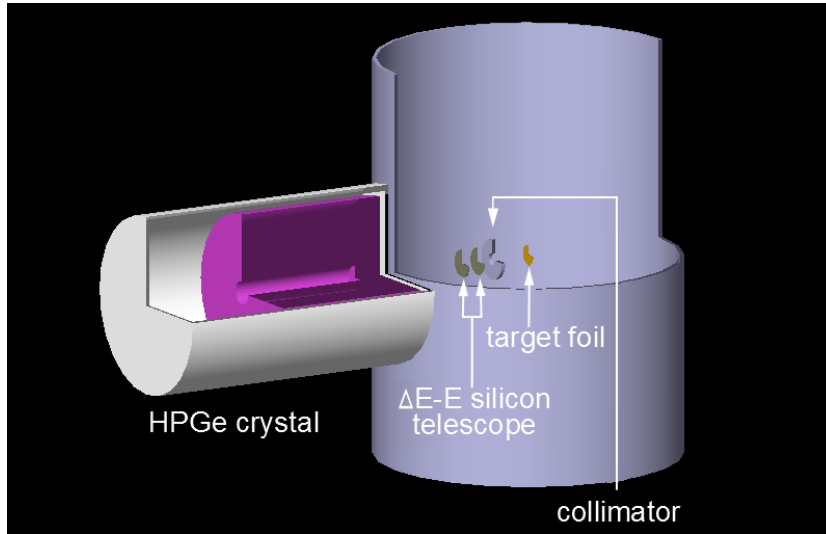


Figure 5.9: Visualization of the detector set up in the Geant code. The beam is assumed to be in the $+\hat{z}$ direction.

ilarly so that the ejectiles are scattered isotropically in the centre-of-mass frame⁵.

3. the reaction site is now also randomized so that the reaction products do not all originate in the same place.

Both the γ -ray direction and the ejectile scattering angles were randomized by picking a $\cos \theta$ uniformly in the interval $(-1, 1)$ for the polar angle and ϕ uniformly in the range $(0, 2\pi)$.

The reaction site was chosen by assuming a uniform beam spot over a circular area with radius 1.5 mm. A TRIM [42] calculation for a 40 keV ^3He beam implanted onto a Au foil shows that the ^3He target nuclei will have a short range of ≈ 81 nm in the foil. This is shown in figure 5.10. Thus, a randomization of the reaction site involves randomly selecting the x and y coordinates from a circle of radius 1.5 mm and a z coordinate by

⁵This is in contrast to the previous simulations where ejectile momenta were chosen in a cone in the laboratory frame.

making the assumption that the distribution in figure 5.10 is a Gaussian distribution. The x and y positions were chosen by selecting randomly the polar angle and radial parameters of the circle and then converting them to Cartesian coordinates. While the randomization of the polar angle in the range $(0, 2\pi)$ is trivial, the radial parameter was randomized using random deviate $u \in (0, 1)$ so that radius r was picked using the inverse transformation $r = \sqrt{u}R$, where $R = 1.5$ mm. This procedure avoids the clustering of points near the origin of the circle⁶.

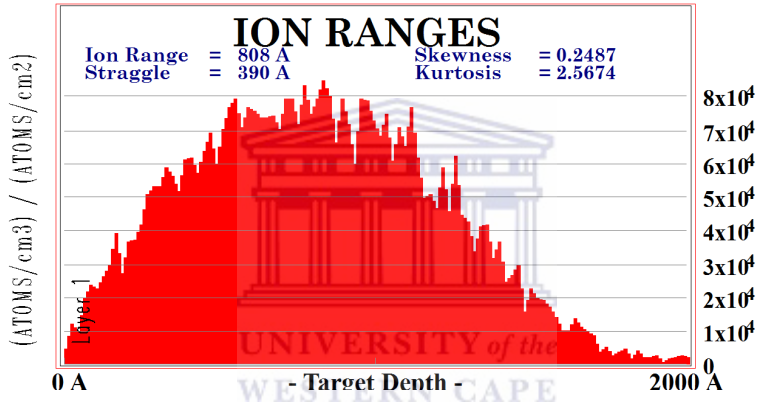


Figure 5.10: Ion ranges for a 40 keV ^3He beam on a Au target.

The z position was randomized using the Box-Müller transformation as explained below. If x_1 and x_2 are uniform deviates over the range $(0, 1)$ and

$$y_1 = \sqrt{-2\ln(x_1)} \cos(2\pi x_2) \quad (5.43)$$

$$y_2 = \sqrt{-2\ln(x_1)} \sin(2\pi x_2), \quad (5.44)$$

⁶This is because in polar coordinates, the differential area element has dimensions of r^2 . Therefore if r is randomized uniformly in $(0, R)$ the probability density will be higher near the origin.

then

$$x_1 = e^{-\frac{1}{2}(y_1^2 + y_2^2)} \quad (5.45)$$

$$x_2 = \frac{1}{2\pi} \tan^{-1} \left(\frac{y_2}{y_1} \right). \quad (5.46)$$

As mentioned previously in Eq. (5.7), the joint probability density functions of the x 's and y 's are related through the Jacobian determinant, which for this case is

$$\begin{vmatrix} \frac{\partial x_1}{\partial y_1} & \frac{\partial x_1}{\partial y_2} \\ \frac{\partial x_2}{\partial y_1} & \frac{\partial x_2}{\partial y_2} \end{vmatrix} = - \left[\frac{1}{\sqrt{2\pi}} e^{-\frac{y_1^2}{2}} \right] \left[\frac{1}{\sqrt{2\pi}} e^{-\frac{y_2^2}{2}} \right]. \quad (5.47)$$

The Jacobian gives independent functions of y_1 and y_2 so that each of them is normally distributed about 0 with a variance of 1. This is known as the Box-Müller transformation for generating pairs of deviates that follow a Gaussian distribution with unit variance and a mean at the origin. After choosing a y in this way from either of these functions, it is easy to multiply by the required variance and add the required mean to obtain the desired distribution. A useful trick for applying the Box-Müller transform is to pick v_1 and v_2 as coordinates defining a point inside a unit circle⁷ and further defining x_1 and x_2 as

$$x_1 = v_1^2 + v_2^2 \quad (5.48)$$

$$x_2 = \tan^{-1} \left(\frac{v_2}{v_1} \right). \quad (5.49)$$

The advantage of this method is that the trigonometric functions in Eqs. (5.43) and (5.44) can be replaced with $v_2/\sqrt{x_1}$ and $v_1/\sqrt{x_1}$ respectively, which considerably speeds up computation time.

⁷This is typically done using an acceptance-rejection type function which keeps choosing v_1 and v_2 in $(-1, 1)$ until $v_1^2 + v_2^2 < 1$.

Once the reaction site is randomized, the time of the decay event is randomly chosen using the same method as before. This time is to be used later in the simulation. Next, the `PrimaryGeneratorAction` part of the code invokes the kinematics code⁸ to find the initial momenta of the ejectile and recoil and sets the primary particles in motion. While transporting the recoil through the simulation, the `SteppingAction` class monitors the recoil position and momentum and at decay time this information is extracted to be used for calculating the Doppler shifts for the gamma rays. Once all the particles have either lost all their energy or left boundaries of the simulation, the simulation records the results and moves on to the next event.

Results

The Geant4 simulations were run using 12 different geometries for 4 million events each. The 12 geometries varied the ejectile acceptance angle with 3 different collimators (4.9 mm, 7.6 mm and 10.7 mm apertures) and placed the HPGe crystal at distances from the target ranging from 85 mm up to 175 mm. The simulated events were histogrammed using ROOT and are shown in the following pages.

⁸This is the same kinematics code discussed before, with minor modifications.

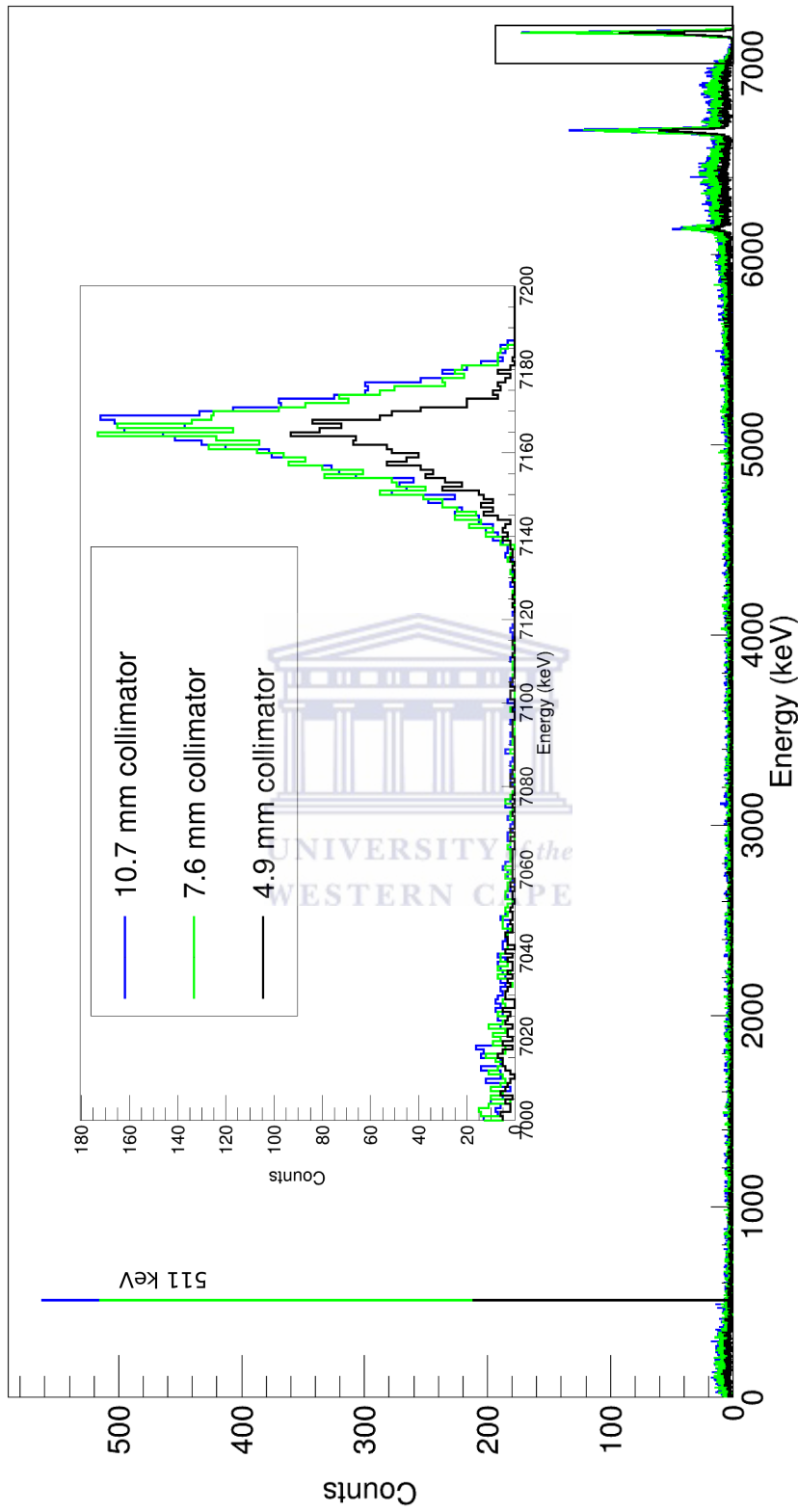


Figure 5.11: The effects of different collimator sizes for a germanium detector placed 85 mm from the target. The inset shows the photopeak in more detail. These spectra are plotted individually on the next page for greater clarity.

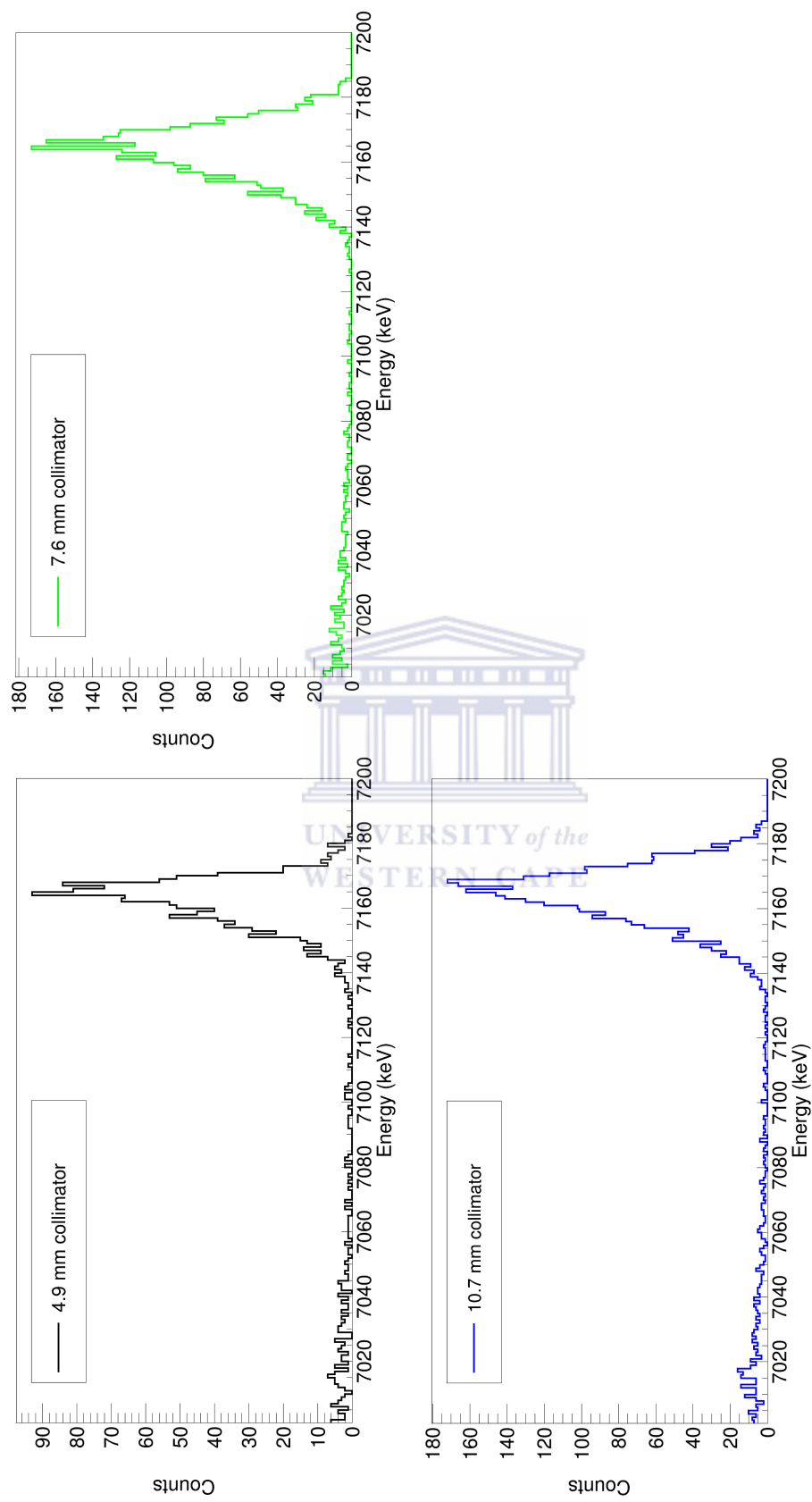


Figure 5.12: The photopeak from the individual spectra in figure 5.11 are plotted separately here for greater clarity. There is clearly little difference between the result obtained using the 7.6 mm collimator as compared to the 10.7 collimator. Using the 4.9 mm collimator however show an improvement in the lineshape at the cost of detection efficiency.

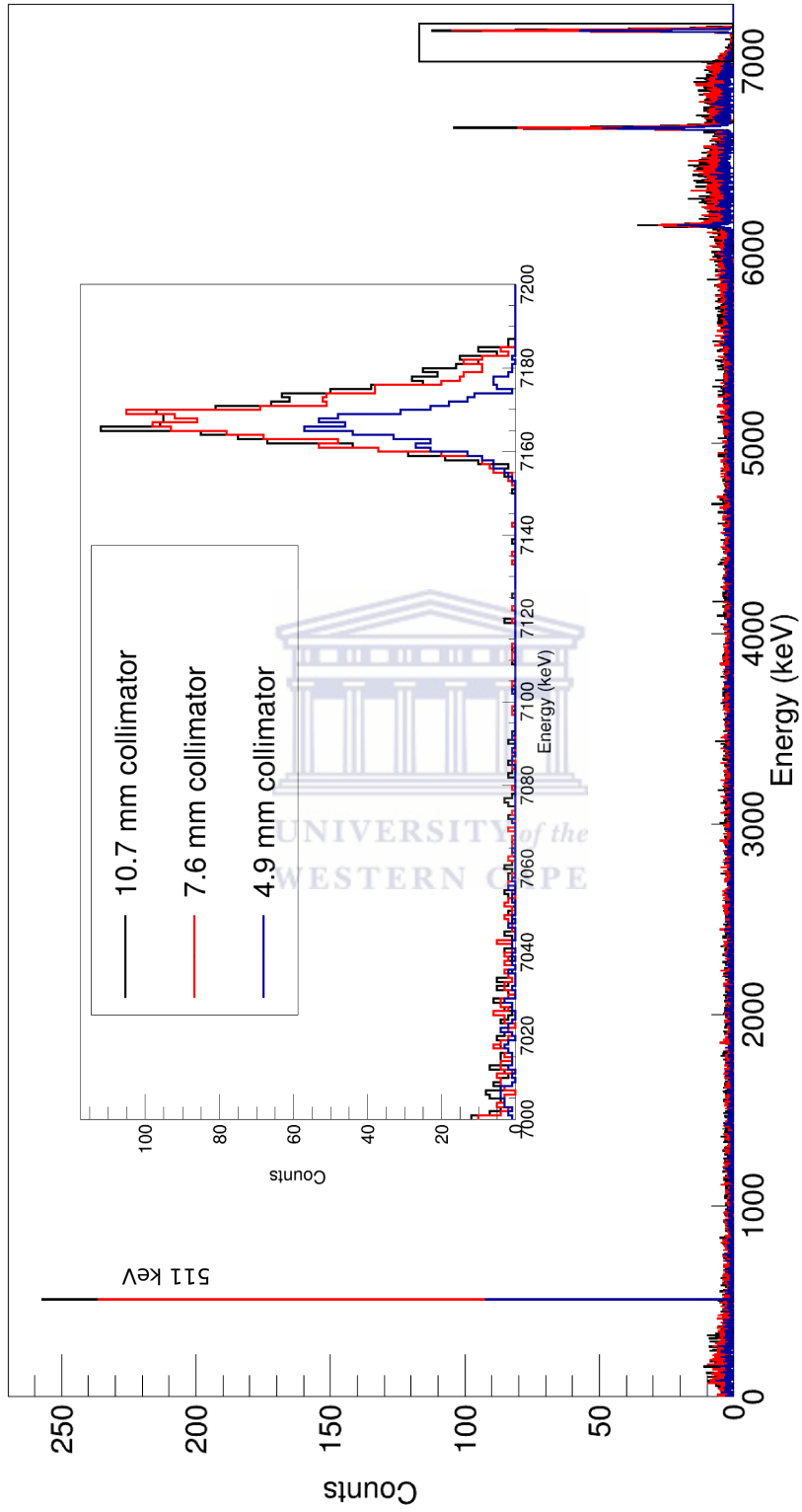


Figure 5.13: The effects of different collimator sizes for a germanium detector placed 145 mm from the target. The inset shows the photopeak in more detail. These spectra are plotted individually on the next page for greater clarity.

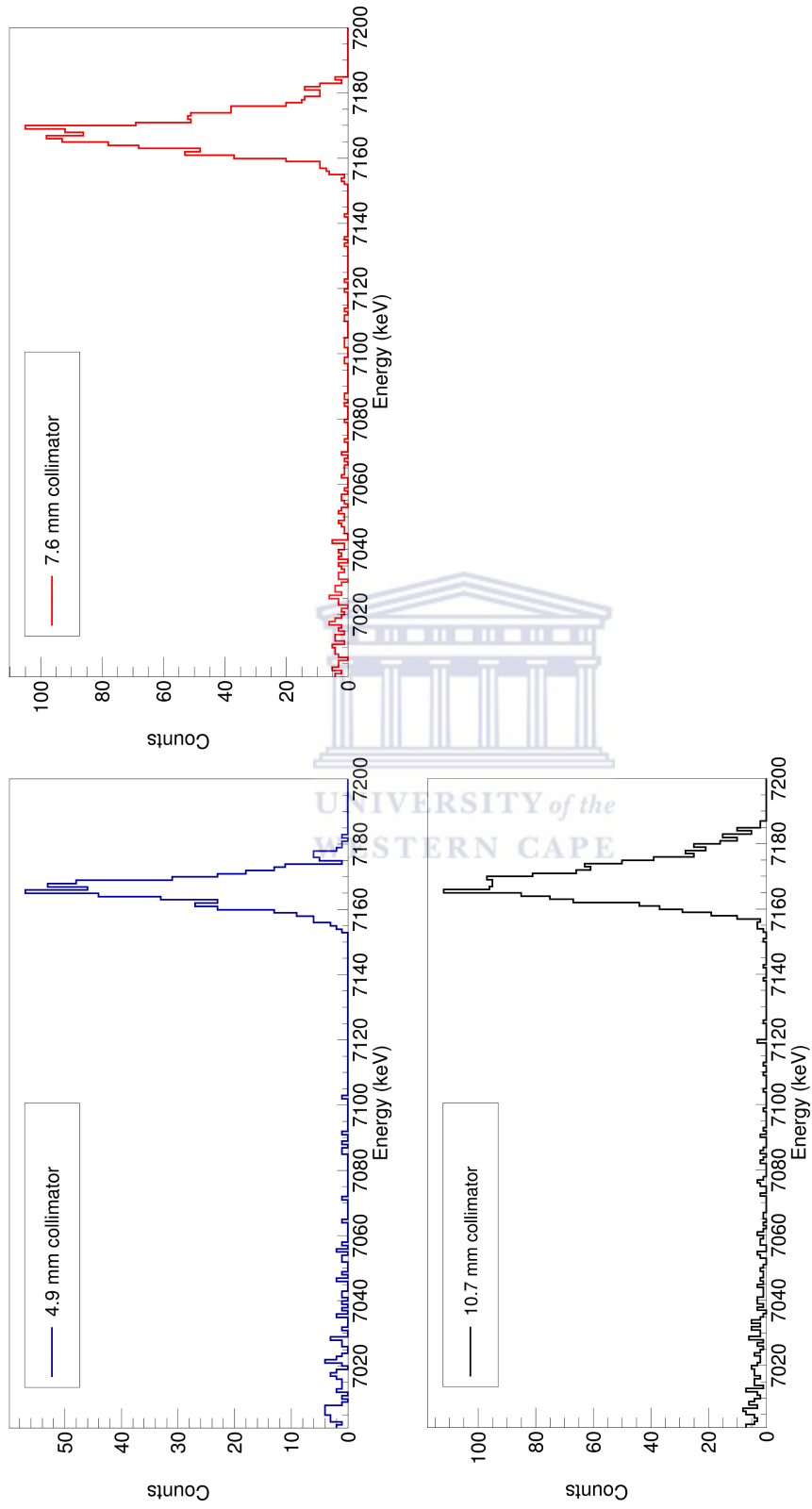


Figure 5.14: The photopeak from the individual spectra in figure 5.13 are plotted separately here for greater clarity. Again same trends from before are visible, there is little difference between the 10.7 and 7.6 mm collimators and the improvement in the lineshape from using a 4.9 mm collimator comes at a cost in efficiency.

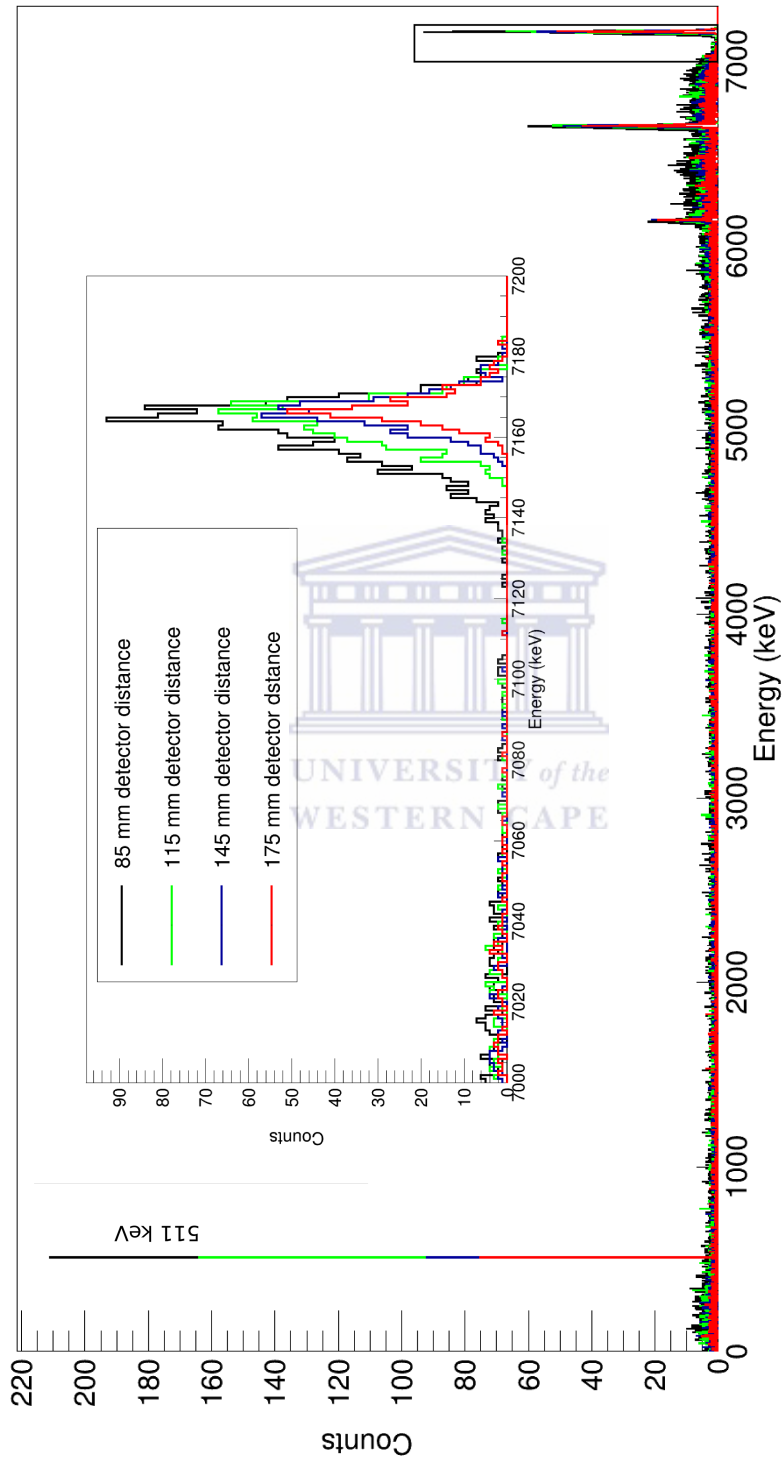


Figure 5.15: The effects of moving the germanium detector to different distances from the target using a 4.9 mm collimator. There is a visible improvement in lineshape on reducing the HPGe detector solid angle.

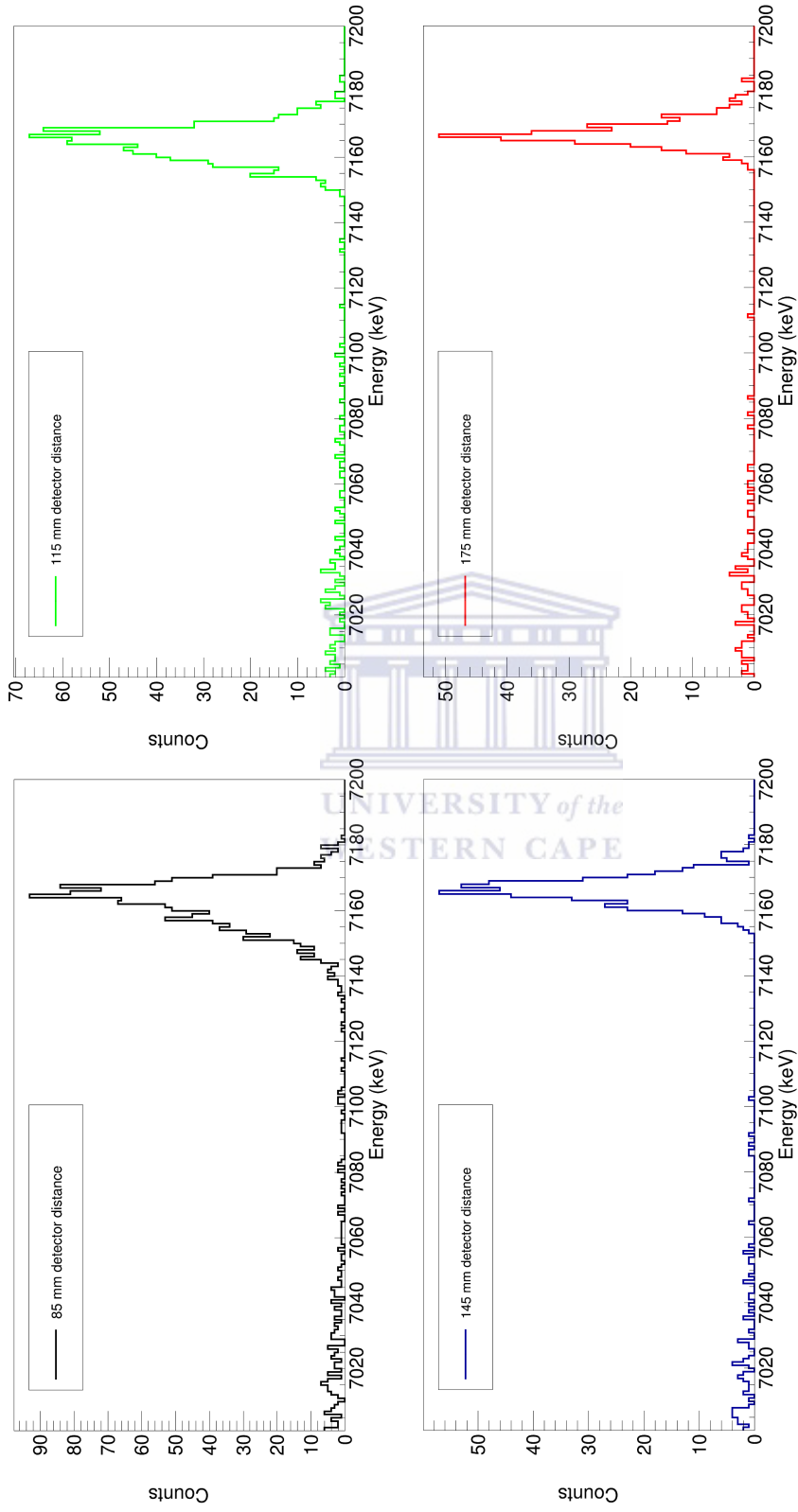


Figure 5.16: These are the spectra from figure 5.15 plotted individually for greater clarity. Clearly the photopeak becomes narrower as the HPGe detector is moved further from the target.

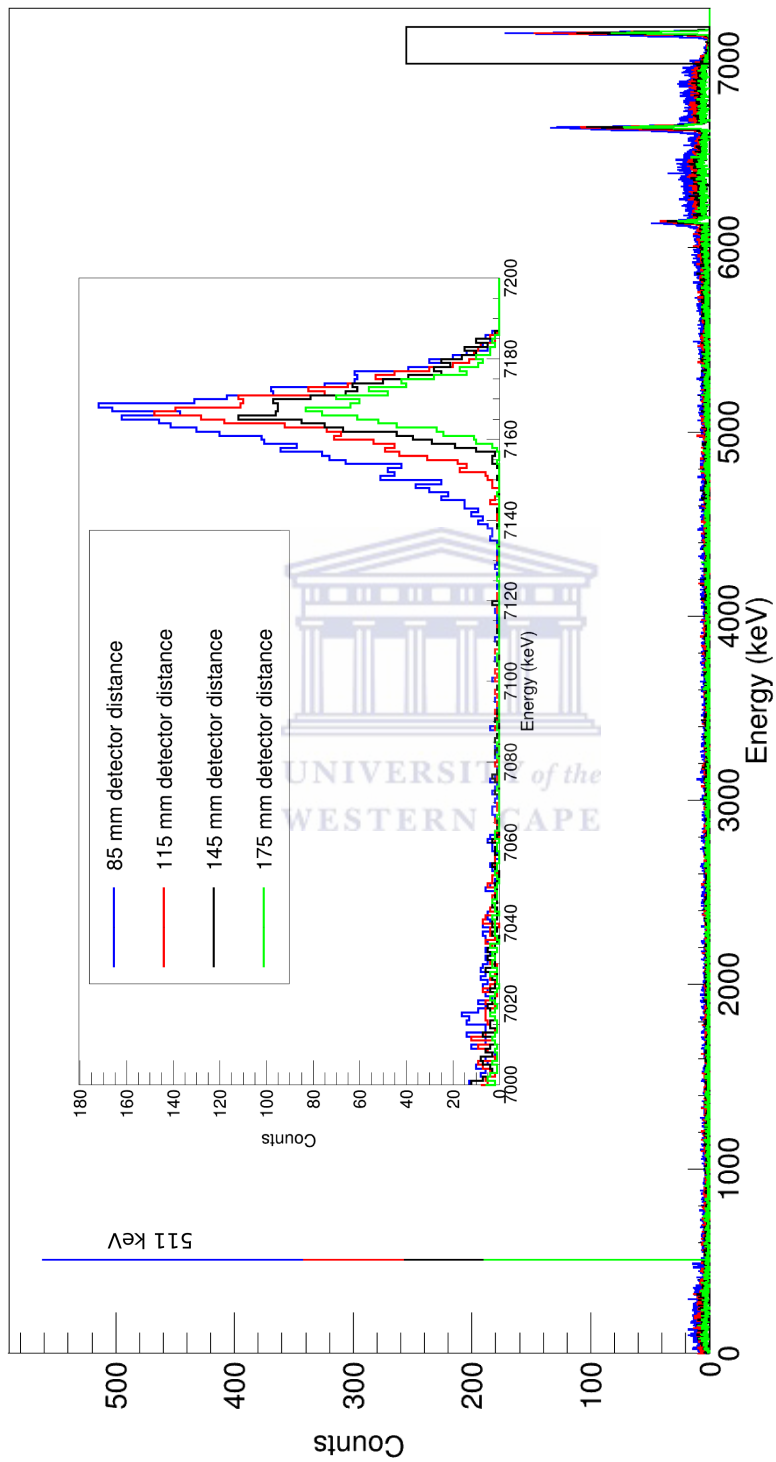


Figure 5.17: The effects of moving the germanium detector to different distances from the target using a 10.7 mm collimator. Again these data show similar trends as before. The wider collimator allows better statistics at the cost of good lineshape.

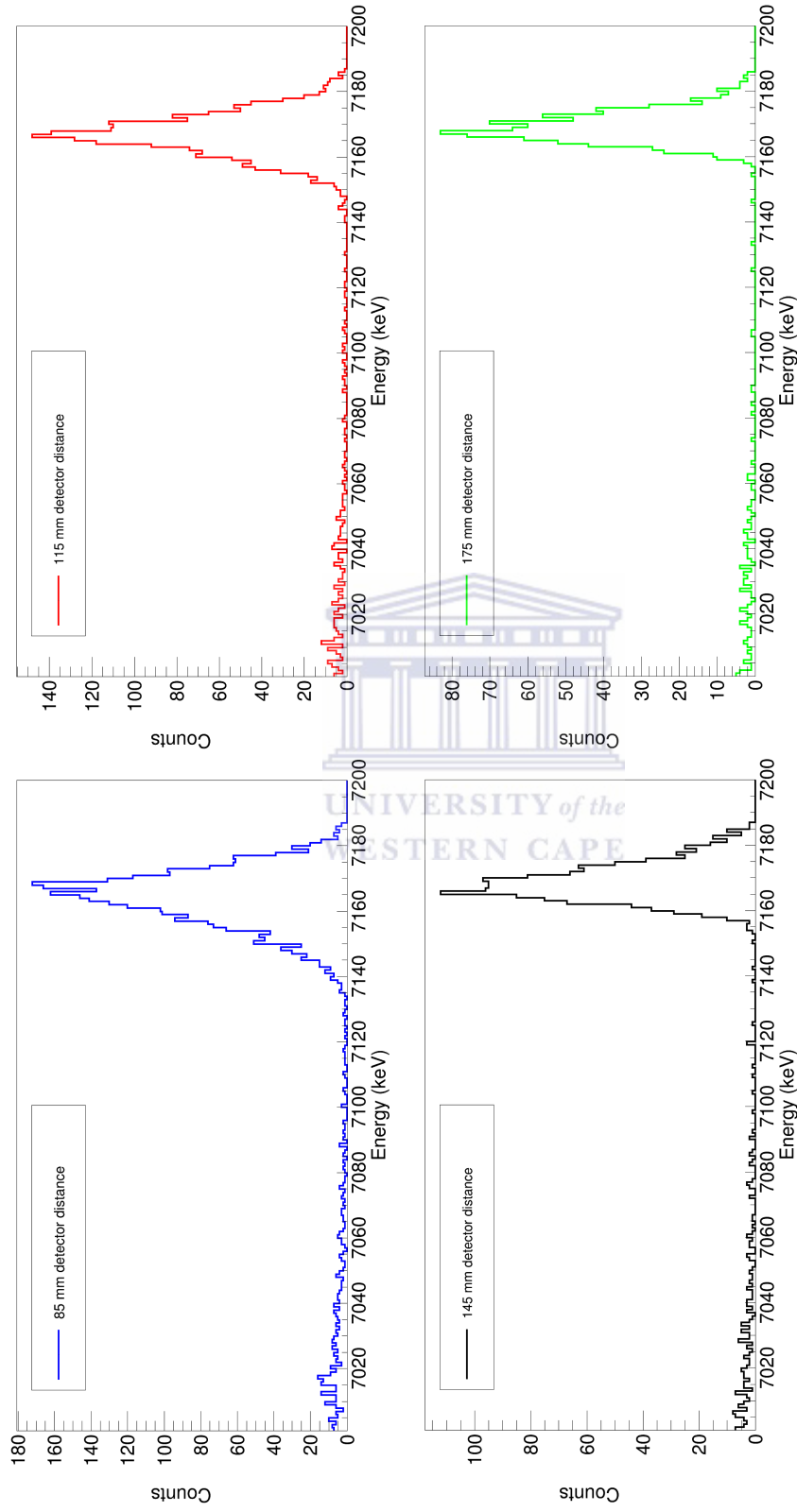


Figure 5.18: These are the spectra from figure 5.17 plotted individually for greater clarity. Again, these data show similar trends to before.

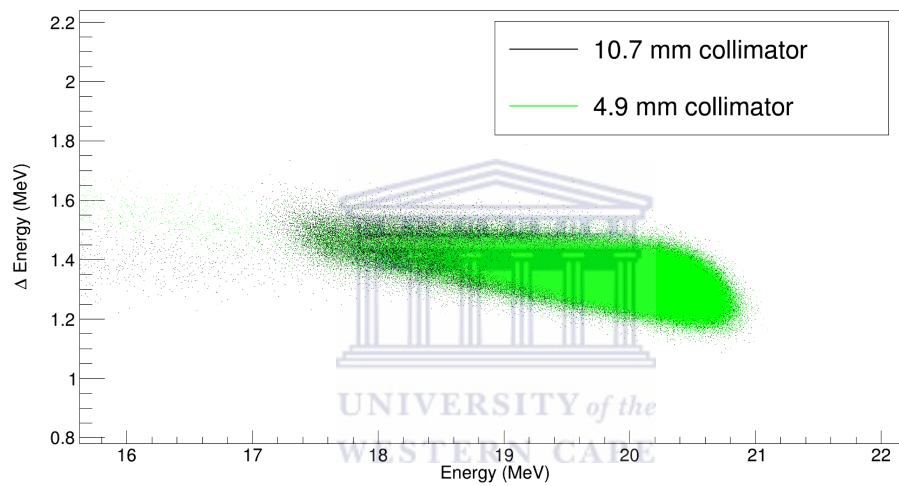


Figure 5.19: Spectra from the $\Delta E - E$ detector for different collimators (4.9 mm in green and 10.7 mm in black). These particle spectra were gated on to obtain the coincidence data presented earlier. The effect of this is shown in figures 5.20 and 5.21

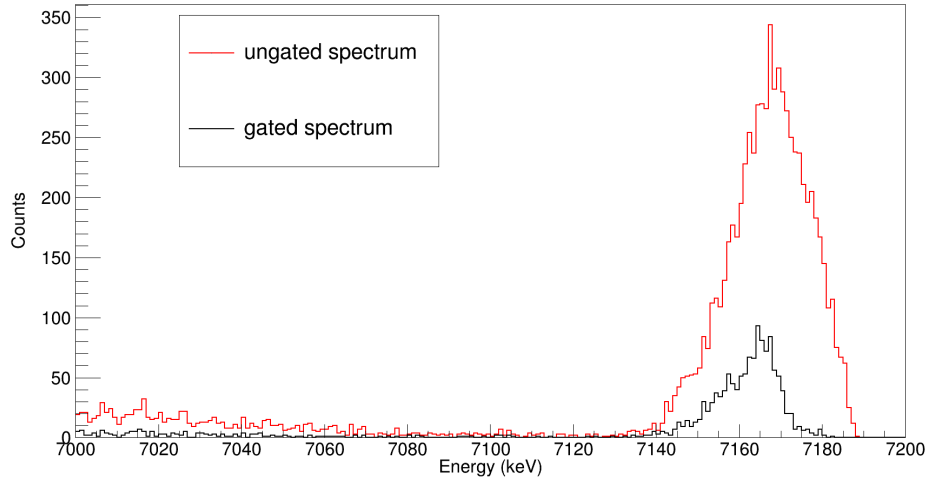


Figure 5.20: Comparison between a raw γ spectrum and one obtained by gating on the particle spectrum. Both spectra were generated with a 4.9 mm collimator and a detector distance of 85 mm from the target.

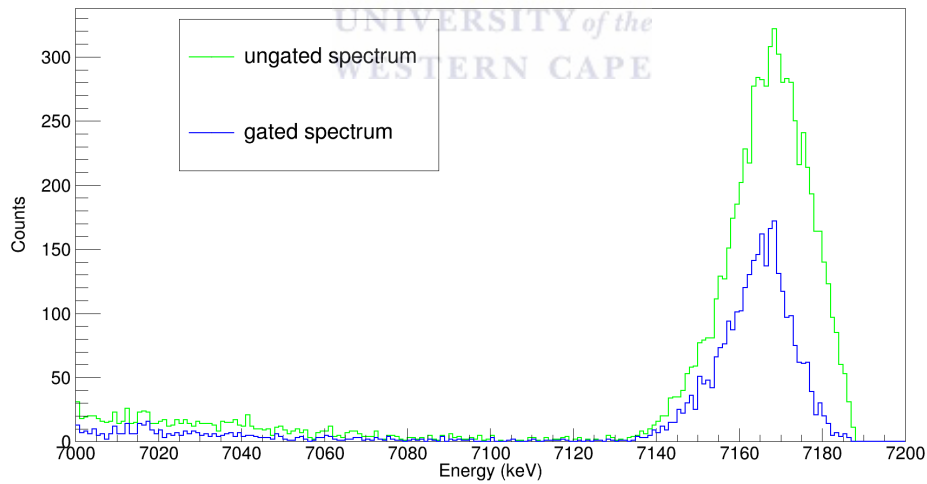


Figure 5.21: Comparison between a raw γ spectrum and one obtained by gating on the particle spectrum. Both spectra were generated with a 10.7 mm collimator and a detector distance of 85 mm from the target.

Efficiencies

The Geant simulations were also used to investigate the absolute γ -detection efficiencies for the various possible configurations of the set up. The particle detection efficiencies were purely dependent on the solid angle subtended by the collimator. Clearly this had a bearing on the extracted γ -ray lineshapes, as established previously (see fig.5.5). Our coincidence information in figures 5.19, 5.20 and 5.21 unfortunately lack the statistics required to make this conclusion. The simulation can however be run with higher statistics to prove our claim. Nevertheless, given the available data, the extracted γ -ray efficiencies are shown in Table 5.1 and are plotted in figures 5.22, 5.23 and 5.24.



Table 5.1: Absolute photopeak efficiencies at 7180 keV obtained from the Geant4 simulation.

Collimator aperture [mm]	Detector distance [mm]	Absolute photopeak efficiency [%]
4.9	85	0.0306 ± 0.0012
4.9	115	0.0199 ± 0.0010
4.9	145	0.0129 ± 0.0008
4.9	175	0.0088 ± 0.0006
7.6	85	0.0707 ± 0.0019
7.6	115	0.0441 ± 0.0015
7.6	145	0.0302 ± 0.0013
7.6	175	0.0201 ± 0.0010
10.7	85	0.0772 ± 0.0020
10.7	115	0.0485 ± 0.0016
10.7	145	0.0343 ± 0.0013
10.7	175	0.0214 ± 0.0011

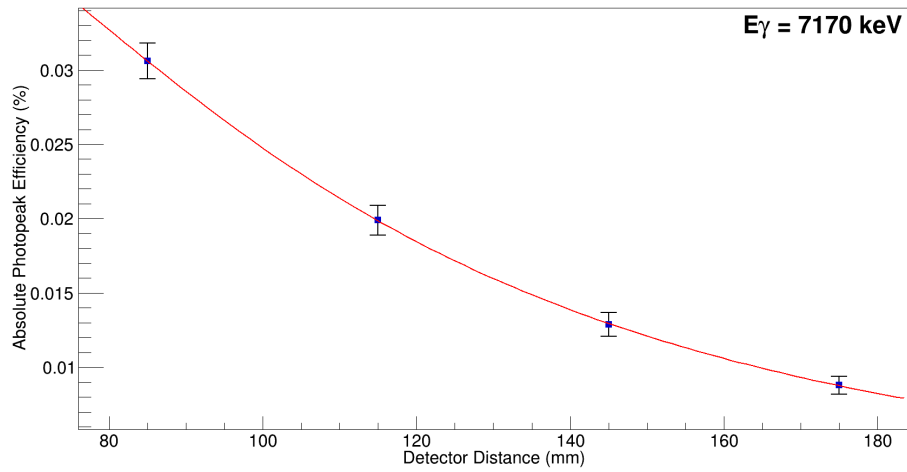


Figure 5.22: The $\alpha-\gamma$ coincidence efficiency for the 4.9 mm collimator setting as a function of detector distance. As expected, the efficiency is reduced at large distances.

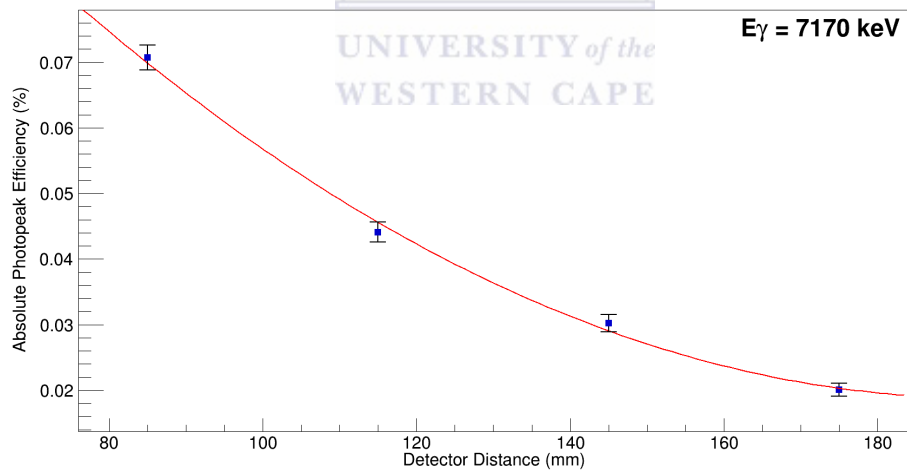


Figure 5.23: The coincidence efficiency for the 7.6 mm collimator setting as a function of detector distance.

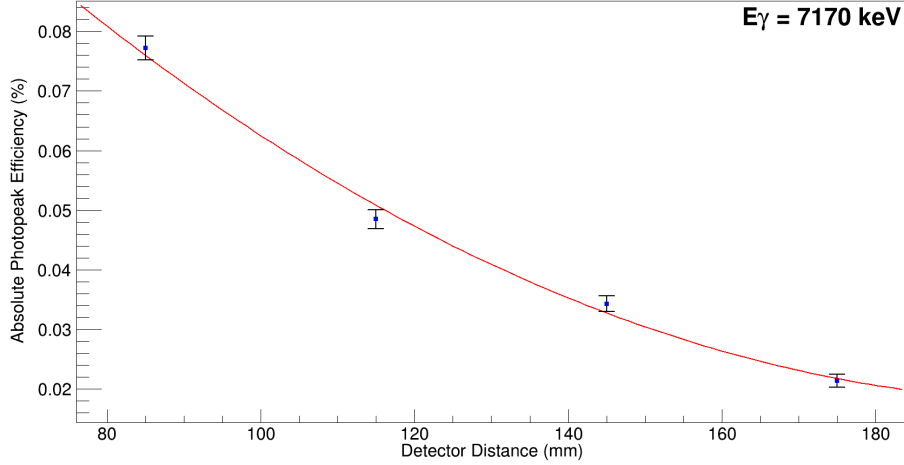


Figure 5.24: The coincidence efficiency for the 10.7 mm collimator setting as a function of detector distance. The efficiencies for this collimator setting are very similar to those for the 7.6 mm collimator.

As an example, we can estimate the beam time requirements for a measurement of the $\tau \simeq 1$ fs lifetime of the 6791 keV state in ^{15}O with the 4.9 mm collimator and the HPGe detector distance at 175 mm from the target⁹. Based on approximate estimates [32], if one assumes $\sigma_{^3\text{He},\alpha} \sim 1.5$ mb, for production of the state of interest, and a target density of $\approx 10^{18}$ ^3He atoms/ cm^2 in the foil, with a beam current of 10 pA, it will take ~ 80 hours to get ~ 3000 counts in the photopeak. This amounts to around two weekends of beam time at iThemba LABS, which is not unreasonable.

⁹This combination offers lowest efficiency and maximum sensitivity to the lineshape from our simulation data sets described in chapter 5.

Chapter 6

Conclusions

In conclusion we have designed and developed a new experimental set up and simulations for the measurement of short nuclear level lifetimes, particularly related to nuclear astrophysics, using the Doppler Shift Attenuation Method. Our design is based on using direct nuclear reactions in inverse kinematics with heavy ion beams on light implanted targets. Our simulations show that for maximal sensitivity to the shortest lifetimes it is imperative to place the γ -ray detector at 0° to the beam and to collimate the light ejectiles from the reaction at forward angles. However sensitivity to γ -ray lineshape also comes with a cost in efficiency. Nevertheless, we are now equipped with a tool to plan actual measurements using these simulations. Depending on the reaction used and the lifetime that needs to be measured, the placement of the HPGe detector and the acceptance angle of the particle collimator can be optimized for each individual measurement using these codes.

Appendix A

Cross sections

A.1 Scattering Theory

Let us begin by considering the case of a beam of nearly monoenergetic particles scattering elastically off a target nucleus at the origin. Assume the beam particles can be approximated reasonably well by plane waves, and choose the z -axis parallel to the beam so that for the initial state $\psi_{initial}$ we have in the position basis

$$\psi_{initial} = A_0 e^{i(\mathbf{k}\cdot\mathbf{r})} \Psi_{projectile} \Psi_{target} \quad (A.1)$$

where $\Psi_{projectile} \Psi_{target}$ represents the internal degrees of freedom of both nuclei and is a function of their internal coordinates. The functions labelled by Ψ will in general be model dependent, a common choice is to use results from one of the many shell model codes available. In the absence of any potential no scattering would take place and the final state would be exactly the same. Introducing a scattering potential at the origin prompts us to modify this

initial guess at the final state to

$$\psi_{final} = A_0 \left[e^{i(\mathbf{k}\cdot\mathbf{r})} \Psi_{projectile} \Psi_{target} + f(\theta, \phi) \frac{e^{i(\mathbf{k}\cdot\mathbf{r})}}{r} \Psi_{ejectile} \Psi_{residual} \right], \quad (\text{A.2})$$

with the scattering amplitude $f(\theta, \phi)$ representing the probability of the projectile being scattered in the direction (θ, ϕ) . So far the scenario described involves only one channel (elastic scattering), in reality many channels may be open and their individual contributions should be summed. Additionally, we should allow for projectiles and targets to become excited as well as the possibility of particles being exchanged in the scattering event so that now the final state in the limit $r \rightarrow \infty$ becomes

$$\lim_{r \rightarrow \infty} \psi_{final} = A_0 \left[e^{i(\mathbf{k}\cdot\mathbf{r})} \Psi_{projectile} \Psi_{target} + \sum_b f_b(\theta, \phi) \frac{e^{i(\mathbf{k}_b\cdot\mathbf{r})}}{r_b} \Psi_{ejectile} \Psi_{residual} \right], \quad (\text{A.3})$$

where the subscript b represents a range of elastic and inelastic processes which may contribute to the final wavefunction [36].

In general the scattering amplitude will be a function of the momentum direction of the scattered particles, or equivalently the coordinates of the detector, as well as the energy of the beam, the state of the scattered particles, and the specifics of the interaction that mediates the scattering process. Thus the scattering amplitude is associated with a specific exit channel and should be marked with a subscript indicating this association.

In some sense $f_b(\theta, \phi)$ represents the probability that an incident particle will be scattered in the direction (θ, ϕ) in channel b and so clearly, due to conservation laws,

$$|f_b(\theta, \phi)|^2 \leq 1. \quad (\text{A.4})$$

In addition to this, the dependence of f_b on the angle ϕ is the result of angular momentum effects; if both the beam and target are unpolarized, this can be dropped.

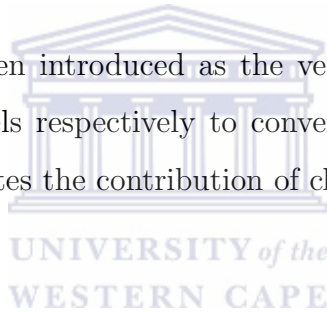
Keeping in line with the interpretation of f_b being related to probability, we expect to be able to calculate the differential cross-section using

$$\frac{d\sigma_b}{d\Omega} = \frac{v_b}{v_a} \frac{\psi_b^* \psi_b}{\psi_{initial}^* \psi_{initial}} \quad (\text{A.5})$$

$$\frac{d\sigma_b}{d\Omega} = \frac{v_b}{v_a} \frac{|f_b(\theta)|^2 \psi_{final}^* \psi_{final}}{\psi_{initial}^* \psi_{initial}} \quad (\text{A.6})$$

$$\frac{d\sigma_b}{d\Omega} = \frac{v_b}{v_a} |f_b(\theta)|^2, \quad (\text{A.7})$$

where v_a and v_b have been introduced as the velocities of particles in the entrance and exit channels respectively to convert particle density to flux and the notation ψ_b denotes the contribution of channel b to the final wavefunction.



A.2 Resonant Scattering

Now consider the problem of particles carrying no charge and no angular momentum (s -wave or $\ell = 0$ neutrons) that are scattered off a nucleus. If we assume there is some limiting range R on the scattering potential, such that the particles are unaffected by it at large distances, we would expect the radial component of the wavefunction to be of a form

$$\Psi_{out}(r) = A \frac{e^{ikr}}{r} + B \frac{e^{-ikr}}{r} \quad (\text{A.8})$$

$$\Psi_{in}(r) = C \frac{e^{ikr}}{r} + D \frac{e^{-ikr}}{r} \quad (\text{A.9})$$

and we can impose boundary conditions to ensure that these functions meet smoothly at the edge of the potential. Let us now look more closely at the wavefunction in the outer region which can be modified such that the incoming waves have an amplitude of unity

$$u(r) = \frac{\Psi_{out}(r)}{r} \quad (\text{A.10})$$

$$u(r) = e^{-ikr} - \eta e^{ikr} \quad (\text{A.11})$$

with $\eta = -\frac{A}{B}$. If every particle entering a sphere of radius R , concentric with the scattering potential, were to leave again we would expect $\eta = 1$. Values of $\eta < 1$ would suggest that some of the particles are being taken out of the elastic channel through processes that occur within this imaginary sphere¹.

We should expect this quantity to be related to the reaction cross section. Looking at the logarithmic derivative we find

$$g = \left(\frac{R du}{u dr} \right) = \frac{(-ikR)(u + 2\eta e^{ikr})}{u} \quad (\text{A.12})$$

and we can solve for η now

$$\begin{aligned} ug &= -ikRu - 2ikR\eta e^{ikR} \\ u(g + ikR) &= -2ikR\eta e^{ikR} \\ (e^{-2ikR} - \eta)(g + ikR) &= -2ikR\eta \\ \frac{e^{-2ikR}(g + ikR)}{-2ikR} &= \eta \left(1 + \frac{(g + ikR)}{-2ikR} \right) \\ \frac{e^{-2ikR}(g + ikR)}{-2ikR} &= \eta \left(\frac{(g + ikR) - 2ikR}{-2ikR} \right) \\ \eta &= \frac{(g + ikR)}{(g - ikR)} e^{-2ikR} \end{aligned} \quad (\text{A.13})$$

¹Note the similarity between η and the scattering amplitude $f(\theta, \phi)$ mentioned earlier. In fact η can be thought of as the scattering amplitude integrated over the solid angle Ω .

Now to find reaction scattering cross section we have

$$\sigma_{re,0} = \pi\lambda^2 \sum_{\ell} (2\ell + 1)(1 - |\eta|^2) = \frac{\pi}{k^2}(1 - |\eta|^2) \quad (\text{A.14})$$

where $(1 - |\eta|^2)$ is the probability of any reaction taking particles out of the elastic scattering channel. If we now expand this bracket and express g as real and imaginary parts we obtain

$$\begin{aligned} 1 - |\eta|^2 &= 1 - \left| \frac{Re(g) + i(Im(g) + kR)}{Re(g) + i(Im(g) - kR)} \right|^2 \\ &= 1 - \frac{[Re(g) + i(Im(g) + kR)] [Re(g) - i(Im(g) + kR)]}{[Re(g) + i(Im(g) - kR)] [Re(g) - i(Im(g) - kR)]} \\ &= 1 - \frac{(Re(g))^2 + (Im(g) + kR)^2}{(Re(g))^2 + (Im(g) - kR)^2} \\ &= \frac{(Re(g))^2 + (Im(g) - kR)^2 - (Re(g))^2 - (Im(g) + kR)^2}{(Re(g))^2 + (Im(g) - kR)^2} \\ &= \frac{-4kRIm(g)}{(Re(g))^2 + (Im(g) - kR)^2} \end{aligned} \quad (\text{A.15})$$

which now relates the reaction cross section to the logarithmic derivative [3]. Notice that only the imaginary component of g contributes to the reaction cross section and so g being purely real would imply that the scattering was purely elastic.

Appendix B

Cubic Splines

A spline is a piecewise defined polynomial which is used to interpolate a tabulated set of values x_i and y_i . The spline is chosen so that it is continuous over the interval $[x_1, x_n]$. In addition to this, the derivatives of the spline are also continuous up to some order [39]. In particular the cubic spline has continuous first and second derivatives.

In general for some set of values $x_1, x_2, x_3, \dots, x_n$ with corresponding values $y_1, y_2, y_3, \dots, y_n$ a cubic spline can be constructed from $n - 1$ cubic functions S_i (one for each subinterval). The S_i 's are defined by

$$S_i(x) = y_i + a_i(x - x_i) + b_i(x - x_i)^2 + c_i(x - x_i)^3, \quad (\text{B.1})$$

when i is a natural number in the interval $[1, n - 1]$. The coefficients a_i, b_i and c_i give a set of $3(n - 1)$ free parameters and we need a matching number of constraints in order to solve for these coefficients. Since the spline must be continuous we have

$$S_i(x_{i+1}) = S_{i+1}(x_{i+1}) = y_{i+1}, \quad (\text{B.2})$$

at each interior point which produces $n - 2$ constraints. An additional continuity condition is that

$$S_{n-1}(x_n) = y_n. \quad (\text{B.3})$$

Next there are smoothness conditions requiring the derivatives to be continuous as well

$$S'_i(x_{i+1}) = S'_{i+1}(x_{i+1}) \quad (\text{B.4})$$

$$S''_i(x_{i+1}) = S''_{i+1}(x_{i+1}), \quad (\text{B.5})$$

at each interior point. These produce $n - 2$ further constraints each. In total this makes $3n - 5$ constraints. The final two constraints can be derived in a few different ways. One option is for the user to define what the second derivative is at the end points. Another option, known as the ‘natural’ spline, is to set the second derivative equal to zero at the end points.

For this thesis work we used a cubic spline to interpolate a table of stopping powers obtained from a SRIM calculation. Since we were only interested in values far from the endpoints of the table a ‘natural’ spline was used.

Appendix C

Relativistic Kinematics Code

```
/*Class file containing functions for running kinematic
calculations*/
#include <math.h>
#include <stdlib.h>
#include <fstream>
#include <iostream>
#include <iomanip>
#include <string>

/*Data structures for storing Centre of Mass(com) and
* Lab(lab) related information. The first label denotes
* masses, energies, momenta and scattering angles in that
* order with the second label being used to identify each
* particle. eg. lab[1][2] is the energy for particle 3 in
* the lab frame (zero subscripting)*/
double lab[4][4];
double com[4][4];
```



```

double Elab, Ecom, Ebeam, Eth, Qgs, Q, alpha, beta, gam,
temp, pz, pPerp, altE, altTheta, altP;
const double pi = 3.14159265359;
//char str[100];
/*Array for scattering angles for particle 3. The first
 * label is CoM angle, Lab equivalent, E3 and E4. The
 * second label goes from CoM angle 1 to 180 in degrees.*/
double angles[4][180];

//std::setprecision(9);
/*Function to set all data values to zero*/
void clearKin()
{
for(int i = 0 ; i < 4; i++)
{
for(int j = 0; j < 4; j++)
{
lab[i][j] = com[i][j] = 0;
}
}

for(int i = 0; i < 180; i++)
{
angles[0][i] = i + 1;
angles[1][i] = angles[2][i] = angles[3][i] = 0;
}

Elab = Ecom = Ebeam = Qgs = Q = altE = 0;

```

```

}

/*Function to set masses for the 4 particles, the beam
 * energy, scattering angle and Q-value of the reaction.
 * Performs a check to see if the Q-value is valid,
 * converts the scattering angle to radians and performs
 * some other intial calculation.*/
void readKin1()
{
for(int i = 0; i < 4; i++)
{
std::cout << "Enter mass of particle " << i + 1
<< " in MeV:\t";
std::cin >> lab[0][i];
printf("%10.8f",lab[0][i]);
com[0][i] = lab[0][i];
}
Qgs = lab[0][0] + lab[0][1] - lab[0][2] - lab[0][3];
std::cout << Qgs;

std::cout << "Enter the Q-value:\t";
std::cin >> Q;
std::cout << Q;

if (Q - Qgs > 1e-9)
{
std::cout << "Invalid Q-value. Program crashed.

```



```

Press enter and start over.";
std::cin >> Q;
exit(0);
}
//Find threshold energy
Eth = lab[0][0] - Q*(lab[0][0] + lab[0][1]
+ lab[0][2] + lab[0][3])/(2*lab[0][1]);

//add the excitation energy (Qgs - Q) to the mass of
//particle 4
com[0][3] = lab[0][3] + Qgs - Q;

std::cout << "Enter the beam energy:\t";
std::cin >> Ebeam;

std::cout << "Enter the lab scattering angle for
particle 3:\t";
std::cin >> lab[3][2];
lab[3][2] = lab[3][2]*pi/180;
}

/*Does the same as readKin1, except it takes all the data
* in as arguments rather than input from the keyboard.*/
void readKin2(double m1, double m2, double m3, double m4,
double Qv, double beam, double theta)
{

```

```

com[0][0] = lab[0][0] = m1;
com[0][1] = lab[0][1] = m2;
com[0][2] = lab[0][2] = m3;
com[0][3] = lab[0][3] = m4;

Qgs = lab[0][0] + lab[0][1] - lab[0][2] - lab[0][3];

Q = Qv; // printf("%7.6f \n", Q);

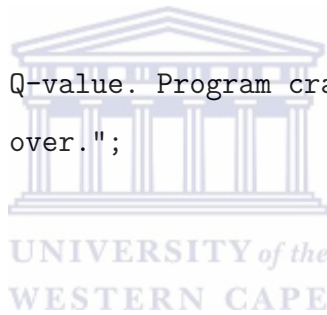
if (Q - Qgs > 1e-9)
{
std::cout << "Invalid Q-value. Program crashed.
Press enter and start over.";
std::cin >> Q;
exit(0);
}

//Find threshold energy
Eth = lab[0][0] - Q*(lab[0][0] + lab[0][1] + lab[0][2]
+ lab[0][3])/(2*lab[0][1]);

/*add the excitation energy (Qgs - Q) to the mass of
*particle 4*/
com[0][3] = lab[0][3] = lab[0][3] + Qgs - Q;

// std::cout << "Enter the beam energy:\t";
Ebeam = beam;

```



```

lab[3][2] = theta;
// lab[3][2] = lab[3][2]*pi/180;

}

/*Does the same as readKin1, except it takes all the data
 * in as arguments rather than input from the keyboard.*/
void readKin3(double m1, double m2, double m3, double m4,
double Qv, double beam, double theta)
{

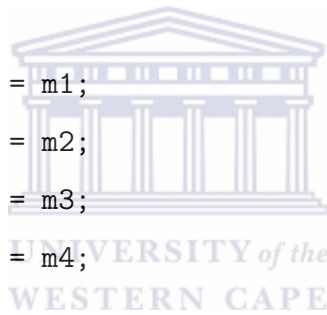
com[0][0] = lab[0][0] = m1;
com[0][1] = lab[0][1] = m2;
com[0][2] = lab[0][2] = m3;
com[0][3] = lab[0][3] = m4;

Qgs = lab[0][0] + lab[0][1] - lab[0][2] - lab[0][3];

Q = Qv; // printf("%7.6f \n", Q);

if (Q - Qgs > 1e-9)
{
std::cout << "Invalid Q-value. Program crashed.
Press enter and start over.";
std::cin >> Q;
exit(0);
}

```



```

//Find threshold energy
Eth = lab[0][0] - Q*(lab[0][0] + lab[0][1] + lab[0][2]
+ lab[0][3])/(2*lab[0][1]);

/*add the excitation energy (Qgs - Q) to the mass
*of particle 4*/
com[0][3] = lab[0][3] = lab[0][3] + Qgs - Q;

// std::cout << "Enter the beam energy:\t";
Ebeam = beam;

com[3][2] = theta;
// lab[3][2] = lab[3][2]*pi/180;
}

//Prints out the data.
void printKin()
{
std::cout << "1\t2\t3\t4\n";
for(int i = 0 ;i < 4; i++)
{
for(int j = 0; j < 4; j++)
{
std::cout << lab[i][j] << "\t";
}
}
std::cout << "\n";

```



```

}

std::cout << "The ejectile energy is "
<< std::setprecision(10) <<lab[1][2] - lab[0][2];
std::cout << "Enter to continue";
std::cin >> temp;
}

/*Prints only the E3 (energy of the scattered particle)
 *value. Really just for debugging*/
double getE3()
{
return (lab[1][2] - lab[0][2]);
}

/**/
double getE(int a)
{
return (lab[1][a-1] - lab[0][a-1]);
}

/**/
double getTheta(int a)
{
return lab[3][a-1];
}

/**/

```



```

double getAltTheta()
{
return altTheta;
}

/**/
double getThetaCom(int a)
{
return com[3][a-1];
}

/**/
double getP(int a)
{
return lab[2][a-1];
}

/*Does the main work of the kinematics code.*/
void calc1()
{
lab[1][0] = lab[0][0] + Ebeam;
lab[1][1] = lab[0][1];

lab[2][0] = sqrt(lab[1][0]*lab[1][0]
- lab[0][0]*lab[0][0]);

Elab = lab[1][0] + lab[1][1];

```



```

Ecom = sqrt(lab[0][0]*lab[0][0]
+ lab[0][1]*lab[0][1] + 2*lab[0][1]*lab[1][0]);

com[1][0] = (lab[0][0]*lab[0][0]
+ lab[0][1]*lab[1][0])/Ecom;
com[1][1] = (lab[0][1]*lab[0][1]
+ lab[0][1]*lab[1][0])/Ecom;
com[1][2] = (Ecom*Ecom + lab[0][2]*lab[0][2]
- lab[0][3]*lab[0][3])/(Ecom*2);
com[1][3] = (Ecom*Ecom + lab[0][3]*lab[0][3]
- lab[0][2]*lab[0][2])/(Ecom*2);

com[2][0] = com[2][1] = lab[2][0]*lab[0][1]/Ecom;
com[2][2] = sqrt(com[1][2]*com[1][2]
- com[0][2]*com[0][2]);
com[2][3] = com[2][2];

alpha = lab[2][0]/Elab;
alpha = alpha*(1 + (lab[0][2]*lab[0][2]
- lab[0][3]*lab[0][3])/(Ecom*Ecom));
alpha = alpha/sqrt((1 - ((lab[0][2]+lab[0][3])/Ecom)
*((lab[0][2]+lab[0][3])/Ecom))
*(1 - ((lab[0][2]-lab[0][3])/Ecom)
*((lab[0][2]-lab[0][3])/Ecom)));

if(alpha > 1){
std::cout << "alpha:\t" << alpha << "\n";

```

```

altE = lab[0][1]*lab[1][0] + (lab[0][0]*lab[0][0]
+ lab[0][1]*lab[0][1] - lab[0][2]*lab[0][2]
- lab[0][3]*lab[0][3])/2;
altE = altE*altE - lab[0][2]*lab[0][2]
* lab[0][3]*lab[0][3] - lab[2][0]*lab[2][0]
* lab[0][2]*lab[0][2]
* sin(lab[3][2])*sin(lab[3][2]);
altE = Elab*(lab[0][1]*lab[1][0]
+ (lab[0][0]*lab[0][0] + lab[0][1]*lab[0][1]
+ lab[0][2]*lab[0][2] - lab[0][3]*lab[0][3])/2)
- lab[2][0]*cos(lab[3][2])*sqrt(altE);
altE = altE/(Elab*Elab - lab[2][0]*lab[2][0]
*cos(lab[3][2])*cos(lab[3][2]));
}
lab[1][2] = lab[0][1]*lab[1][0] + (lab[0][0]*lab[0][0]
+ lab[0][1]*lab[0][1] - lab[0][2]*lab[0][2]
- lab[0][3]*lab[0][3])/2;
lab[1][2] = lab[1][2]*lab[1][2] - lab[0][2]*lab[0][2]
* lab[0][3]*lab[0][3] - lab[2][0]*lab[2][0]
* lab[0][2]*lab[0][2] * sin(lab[3][2])
*sin(lab[3][2]);
// lab[1][2] = lab[2][0]*cos(lab[3][2])*sqrt(lab[1][2]);
lab[1][2] = Elab*(lab[0][1]*lab[1][0]
+ (lab[0][0]*lab[0][0] + lab[0][1]*lab[0][1]
+ lab[0][2]*lab[0][2] - lab[0][3]*lab[0][3])/2)
+ lab[2][0]*cos(lab[3][2])*sqrt(lab[1][2]);

```



```
lab[1][2] = lab[1][2]/(Elab*Elab - lab[2][0]*lab[2][0]
*cos(lab[3][2])*cos(lab[3][2]));
```

```
std::cout << "E:\t" << lab[1][2] << "\t"
<< "altE:\t" << altE << "\n";
```

```
lab[1][3] = Elab - lab[1][2];
```

```
lab[2][2] = sqrt(lab[1][2]*lab[1][2]
- lab[0][2]*lab[0][2]);
altP = sqrt(altE*altE - lab[0][2]*lab[0][2]);
lab[2][3] = sqrt(lab[1][3]*lab[1][3]
- lab[0][3]*lab[0][3]);
```

```
beta = lab[2][0]/Elab;
gam = Elab/Ecom;
```

```
pPerp = lab[2][2]*sin(lab[3][2])/com[2][2];
pz = gam*(lab[2][2]*cos(lab[3][2])
+ beta*lab[1][3])/com[2][2];
com[3][2] = atan(pPerp/pz);
if(pz < 0) com[3][2] = pi + com[3][2];
```

```
pPerp = altP*sin(lab[3][2])/com[2][2];
pz = gam*(altP*cos(lab[3][2])
- beta*lab[1][3])/com[2][2];
altTheta = atan(pPerp/pz);
```

```

if(pz < 0) altTheta = pi + altTheta;

com[3][3] = pi - com[3][2];
lab[3][3] = atan(lab[2][2]*sin(lab[3][2])
/(lab[2][0] - lab[2][2]*cos(lab[3][2])));
if(cos(lab[3][2]) < 0)
{
lab[3][3] = lab[3][3] + pi;
}
//std::cout << atan(pPerp/pz)+pi << "\n";
//std::cout << com[3][2] << "\n";
}

void calc2()
{
/*Set lab (total) energies for particles
*1 and 2*/
//E1 = m1 + Ebeam
lab[1][0] = lab[0][0] + Ebeam;
//E2 = m2
lab[1][1] = lab[0][1];

/*Calculate lab momentum of particle 1*/
//p1 = (E1**2 + m1**2)**0.5
lab[2][0] = sqrt(lab[1][0]*lab[1][0]
- lab[0][0]*lab[0][0]);

```



```

/*Calculate total lab energy and convert
  *to CoM frame*/
//Elab = E1 + E2
Elab = lab[1][0] + lab[1][1];
//Ecom = (m1**2 + m2**2 + 2*m2*E1)**0.5
Ecom = sqrt(lab[0][0]*lab[0][0]
+ lab[0][1]*lab[0][1]
+ 2*lab[0][1]*lab[1][0]);

/*Calculate the CoM energies for
  *all particles*/
//E'1 = (m1**2 + m2*E1)/Ecom
com[1][0] = (lab[0][0]*lab[0][0]
+ lab[0][1]*lab[1][0])/Ecom;
//E'2 = (m2**2 + m2*E1)/Ecom
com[1][1] = (lab[0][1]*lab[0][1]
+ lab[0][1]*lab[1][0])/Ecom;
//E'3 = (Ecom**2 + m3**2 - m4**2)/(2*Ecom)
com[1][2] = (Ecom*Ecom + lab[0][2]*lab[0][2]
- lab[0][3]*lab[0][3])/(Ecom*2);
//E'4 = (Ecom**2 + m4**2 - m3**2)/(2*Ecom)
com[1][3] = (Ecom*Ecom + lab[0][3]*lab[0][3]
- lab[0][2]*lab[0][2])/(Ecom*2);

/*Calculate CoM momenta*/
//p'1 = p'2 = p1*m2/Ecom
com[2][0] = com[2][1] = lab[2][0]*lab[0][1]/Ecom;

```

```

//p'3 = (E'3**2 - m3**2)**0.5
com[2][2] = sqrt(com[1][2]*com[1][2]
- com[0][2]*com[0][2]);
//p'4 = p'3
com[2][3] = com[2][2];

/*Calculate beta for the CoM and
 *check that beta < 1*/
//beta = p1/Elab
beta = lab[2][0]/Elab;
if(beta >= 1)
{
std::cout << "Error invalid beta value";
exit(0);
}

/*Calculate gamma from beta*/
gam = 1/sqrt(1 - beta*beta);

/*Calculate the lab momentum for particle 3
 * First relsolve the CoM momentum of particle
 * 3 into a component along the z-axis(pz) and
 * one in the xy-plane(pPerp)
 * Apply a Lorentz transformation to take pz
 * into the lab frame (The Lorentz transformation
 * does not change pPerp)
 * Finally recostruct the momentum of particle 3

```



```

    * in the lab frame and calculate the scattering
    * angle from there.*/
pz = gam*(com[2][2]*cos(com[3][2])
- beta*com[1][2]);
pPerp = com[2][2]*sin(com[3][2]);
lab[2][2] = sqrt(pz*pz + pPerp*pPerp);
//std::cout << pPerp << "\t" << pz << "\n";
//std::cout << pPerp/lab[2][2] << "\n";
lab[3][2] = asin(pPerp/lab[2][2]);
//std::cout << lab[3][2] << "\n";

/*Calculate lab energies for particles 3 and 4*/
lab[1][2] = sqrt(lab[2][2]*lab[2][2]
+ lab[0][2]*lab[0][2]);
lab[1][3] = Elab - lab[1][2];

/*Calculate lab momentum for particle 4*/
lab[2][3] = sqrt(lab[1][3]*lab[1][3]
- lab[0][3]*lab[0][3]);

/*Calculate lab scattering angle for particle 4*/
lab[3][3] = atan(lab[2][2]*sin(lab[3][2])/(lab[2][0]
- lab[2][2]*cos(lab[3][2])));
if(cos(lab[3][2]) < 0) lab[3][3] = lab[3][3] + pi;

}

```

Appendix D

Monte Carlo Doppler Shift Code



```
#include "kinematics.cpp"
#include "MassData.cpp"
#include <fstream>
#include "Monte.cpp"

double getQ(double, double, double, double, double);
double energyLoss(double, double, double, double);

int main()
{

readMassTable();
readStopTable();
//srand(time(NULL));
std::fstream specOut;
```

```

specOut.open("SpectrumOfs0d.txt");

double m1, m2, m3, m4, beam, t, dt, tau, thetaR,
       thetaP, Q, phiR, thetaG, phiG, EG, ED, prx,
       pry, prz, pgx, pgy, pgz, cosThetaD, beta,
       cosLow, cosHi, betaLow, betaHi, ELow, EHi,
       rotAng, temp1, temp2;
double spec[1000];

int bin = 0;
m1 = getMass(16, 8);
m2 = getMass(3, 2);
m3 = getMass(4, 2);
m4 = getMass(15, 8);
beam = 50;
ELow = 7.2;
EHi = 1;
EG = 6.791;
Q = getQ(m1, m2, m3, m4, EG);
rotAng = 0;
dt = 0.001;
tau = 0.0000000000000001;

clearKin();
for(int i = 0; i < 1000; i++) spec[i] = 0;

for(int i = 0; i < 10000; i++)

```



```

{
/*this is where the theta angle (scattering angle)
 * for m3 is generated
 * the function randomTheta takes a double argument
 * which represents the maximum
 * allowable scattering angle in the lab frame.*/
thetaP = randomTheta(0.26005);
readKin2(m1, m2, m3, m4, Q, beam, thetaP);
calc1();
/*this is where the time of the decay is randomly
 * generated. Importantly the function requires a
 * guess of the meanlife. */
t = randomTime(tau);
thetaR = getTheta(4);
phiR = randomPhi();
thetaG = randomTheta(0.18849);
phiG = randomPhi();
prx = getP(4)*sin(thetaR)*cos(phiR);
pry = getP(4)*sin(thetaR)*sin(phiR);
prz = getP(4)*cos(thetaR);
pgx = EG*sin(thetaG)*cos(phiG);
pgy = EG*sin(thetaG)*sin(phiG);
pgz = EG*cos(thetaG);
temp1 = pgy*cos(rotAng) + pgz*sin(rotAng);
temp2 = pgz*cos(rotAng) - pgy*sin(rotAng);
pgy = temp1;
pgz = temp2;

```



```

cosThetaD = (prx*pgx + pry*pgy + prz*pgz)/(getP(4)*EG);
beta = energyLoss(getE(4), (m4 + EG), dt, t);
beta = sqrt(2*m4*beta + beta*beta)/m4;
ED = EG*(1 + beta*cosThetaD);
bin = (int) 10000*ED;
if (bin%10 > 4) bin = bin + 10;
bin = bin/10;
spec[bin - 6290]++;
//std::cout << "Done with gamma " << ED << ".\n";
}
//printKin();
for(int i = 0; i < 1000; i++) specOut << i+6290 << "\t"
<< spec[i] << "\n";
/*std::cout << cosLow << "\t" << betaLow << "\n" << cosHi
<< "\t" << betaHi << "\n";
readKin2(m1, m2, m3, m4, Q, beam, 0.26005);
calc1();
std::cout << (getP(4)/m4) << "\t" << getTheta(4);*/
return 0;
}

double getQ(double m1, double m2, double m3, double m4, double EG)
{
double gs = m1+m2-m3-m4;
return (gs - EG);
}

```

```
double energyLoss(double energy, double m, double dt, double t)
{
double v = sqrt(2*m*energy + energy*energy)/m;
//std::cout << energy << "\n";
for(double time = 0; time < t; time = time+dt)
{
energy = energy - getStop(energy)*v*dt*3;
v = sqrt(2*m*energy + energy*energy)/m;
}
//std::cout << energy << "\n";
return energy;
}
```



Appendix E

The Primary Action Generator from the Geant Code



```
#include "G4RunManager.hh"  
#include "G4Event.hh"  
#include "G4ParticleGun.hh"  
#include "G4ParticleTable.hh"  
#include "G4NuclideTable.hh"  
#include "G4VIsotopeTable.hh"  
#include "G4RIsotopeTable.hh"  
#include "G4IonTable.hh"  
#include "G4ParticleDefinition.hh"  
#include "G4Ions.hh"  
#include "G4PhaseSpaceDecayChannel.hh"  
#include "G4VDecayChannel.hh"  
#include "G4DecayTable.hh"  
#include "G4ChargedGeantino.hh"  
#include "G4SystemOfUnits.hh"
```

```

#include "Randomize.hh"
#include "kinematics.hh"
//#include "gasdev.hh"
//#include "nr.hh"
//#include "ran1.hh"
#include <time.h>
#include <stdio.h>
#include <stdlib.h>
//....ooo00000ooo.....ooo00000ooo.....ooo00000ooo....

extern G4double tau;

B3PrimaryGeneratorAction::B3PrimaryGeneratorAction()
: G4VUserPrimaryGeneratorAction(),
  ejectileGun(0),
  recoilGun(0)
{
  G4int n_particle = 1;
  ejectileGun = new G4ParticleGun(n_particle);
  recoilGun = new G4ParticleGun(n_particle);

  G4ParticleTable* particleTable = G4ParticleTable::GetParticleTable();
  G4ParticleDefinition* particle
      = particleTable->FindParticle("chargedgeantino");
  ejectileGun->SetParticleDefinition(particle);
  ejectileGun->SetParticlePosition(G4ThreeVector(0.,0.,0.));
  ejectileGun->SetParticleEnergy(25*MeV);

```

```

ejectileGun->SetParticleMomentumDirection(G4ThreeVector(1.,0.,0.));

recoilGun->SetParticleDefinition(particle);
recoilGun->SetParticlePosition(G4ThreeVector(0.,0.,0.));
recoilGun->SetParticleEnergy(25*MeV);
recoilGun->SetParticleMomentumDirection(G4ThreeVector(1.,0.,0.));
}

//....ooo00000ooo.....ooo00000ooo.....ooo00000ooo....

B3PrimaryGeneratorAction::~B3PrimaryGeneratorAction()
{
    delete ejectileGun;
    delete recoilGun;
}

//....ooo00000ooo.....ooo00000ooo.....ooo00000ooo....

void B3PrimaryGeneratorAction::GeneratePrimaries(G4Event* anEvent)
{
    srand(time(NULL));
    G4ParticleDefinition* particle = ejectileGun->GetParticleDefinition();
    if (particle == G4ChargedGeantino::ChargedGeantino())
    {
        //This is where the particles are selected.
        G4int Z = 2, A = 4;
        G4double ionCharge = 2.*eplus;
    }
}

```

```

G4double excitEnergy = 0.*keV;

G4ParticleDefinition* ion
    = G4IonTable::GetIonTable()->GetIon(Z,A,excitEnergy);
ejectileGun->SetParticleDefinition(ion);
ejectileGun->SetParticleCharge(ionCharge);
mass3 = ion->GetPDGMass()/MeV - Z*0.511;

Z = 8, A = 15;
ionCharge    = 2.*eplus;
excitEnergy = 6791.*keV;

ion = G4IonTable::GetIonTable()->GetIon(Z, A, excitEnergy);

//std::cout << ion->GetParticleName() << "|\n";
//ion->SetDecayTable(table);
recoilGun->SetParticleDefinition(ion);
recoilGun->SetParticleCharge(ionCharge);
mass4 = ion->GetPDGMass() - Z*511*keV;

Z = 8, A = 16;
excitEnergy = 0.*keV;
ion = G4IonTable::GetIonTable()->GetIon(Z,A,excitEnergy);
mass1 = ion->GetPDGMass() - Z*511*keV;

Z = 2, A = 3;
excitEnergy = 0.*keV;

```

```

    ion = G4IonTable::GetIonTable()->GetIon(Z,A,excitEnergy);
    mass2 = ion->GetPDGMass() - Z*511*keV;
}

// randomized position
//
double gunR, gunPhi, gunX, gunY, gunZ;
gunR = 1.5*((double) rand()/RAND_MAX);
gunPhi = 2*pi*((double) rand()/RAND_MAX);
gunX = sqrt(gunR)*cos(gunPhi);
gunY = sqrt(gunR)*sin(gunPhi);
gunZ = -1.0;
while(gunZ < 0)
{
    gunZ = gauss()*390+808;
}

///G4double x0 = 0*cm, y0 = 0*cm, z0 = 0*cm;
///G4double dx0 = 0*cm, dy0 = 0*cm, dz0 = 0*cm;
G4double x0 = gunX*mm, y0 = gunY*mm, z0 = (gunZ/10)*nm;
//G4double dx0 = 3*mm, dy0 = 3*mm, dz0 = 3*mm;
//x0 += dx0*(G4UniformRand()-0.5);
//y0 += dy0*(G4UniformRand()-0.5);
//z0 += dz0*(G4UniformRand()-0.5);
double Qvalue = mass1/MeV+mass2/MeV-mass3/MeV-mass4/MeV;
double beamEnergy = 50;
/*

```



```

int Z, A;
G4double ionCharge, excitEnergy;

Z = 2;
A = 4;
ionCharge = 2.*eplus;
excitEnergy = 0.*keV;
*/
double phiEjectile, thetaEjectile;
G4ThreeVector *pEjectile = new G4ThreeVector(0., 0., 1.);
G4ThreeVector *pRecoil = new G4ThreeVector(0., 0., 1.);

thetaEjectile = acos(1 + (cos(0.26) - 1)*(G4UniformRand()));
phiEjectile = (G4UniformRand())*2*pi;
tau = -log(G4UniformRand())*1e-6*ns;
pEjectile->rotate(0., thetaEjectile, phiEjectile);

clearKin();
readKin2(mass1,mass2,mass3,mass4,Qvalue,beamEnergy,thetaEjectile);
calc1();
pRecoil->rotate(0., getTheta(4), phiEjectile+pi);

ejectileGun->SetParticlePosition(G4ThreeVector(x0,y0,z0));
ejectileGun->SetParticleMomentumDirection(*pEjectile);
ejectileGun->SetParticleEnergy(getE(3)*MeV);

recoilGun->SetParticlePosition(G4ThreeVector(x0,y0,z0));

```



```

recoilGun->SetParticleMomentumDirection(*pRecoil);
recoilGun->SetParticleEnergy(getE(4)*MeV);

//create vertex
//
ejectileGun->GeneratePrimaryVertex(anEvent);
recoilGun->GeneratePrimaryVertex(anEvent);
delete pEjectile;
delete pRecoil;
}

//.....ooo00000ooo.....ooo00000ooo.....ooo00000ooo.....
double B3PrimaryGeneratorAction::gauss()
{
double v1, v2, res;
v1 = 2.0*((double) rand()/RAND_MAX)-1.0;
v2 = 2.0*((double) rand()/RAND_MAX)-1.0;
res = v1*v1+v2*v2;
return v2*sqrt(-2.0*log(res)/res);
}

```

Bibliography

- [1] J. Heese *et al.* Lifetime measurements in ^{70}Se and ^{72}Se . *Z. Phys. A.*, **325**, 45, (1986).
- [2] A.M. Hurst *et al.* Measurement of the Sign of the Spectroscopic Quadrupole Moment for the 2_1^+ State in ^{70}Se : No Evidence for Oblate Shape. *Phys. Rev. Lett.*, **98**, 072501, (2007).
- [3] C. Iliadis. *Nuclear Physics of Stars*. Wiley-VCH., (2007).
- [4] M. Marta. Precision study of ground state capture in the $^{14}\text{N}(p, \gamma)^{15}\text{O}$ reaction. *Phys. Rev. C*, **78**, 022802, (2008).
- [5] A. Formicola *et al.* Astrophysical S-factor of $^{14}\text{N}(p, \gamma)^{15}\text{O}$. *Phys. Lett. B*, **591**, 61, (2004).
- [6] N. Galinski *et al.* Lifetime measurements of states in ^{15}O . *Phys. Rev. C*, **90**, 035803, (2014).
- [7] W. Gill *et al.* Lifetime measurements in mass-15 nuclei. *Nucl. Phys. A*, **121**, 209, (1968).
- [8] P.F. Bertone *et al.* Lifetime of the 6793-keV state in ^{15}O . *Phys. Rev. Lett.*, **87**, 152501, (2001).

- [9] D. Schürmann *et al.* Lifetime measurement of the 6792 keV state in ^{15}O , important of the astrophysical S factor extrapolation in $^{14}\text{N}(p, \gamma)^{15}\text{O}$. *Phys. Rev. C*, **77**, 055803, (2008).
- [10] R.M. Eisberg. *Fundamentals of Modern Physics*. John Wiley & Sons, Inc., New York, (1961).
- [11] Ashby & Miller. *Principles of Modern Physics*. Holden-Day, Inc., 500 Sansome Street, San Francisco, California, (1970).
- [12] S.G. Nilsson and I. Ragnarsson. *Shapes and Shells in Nuclear Structure*. John Wiley & Sons, Inc., New York, (1961).
- [13] R Hall. Ionization energies of neutral elements, in units of ev. (2008).
- [14] D.J. Rowe and J.L Wood. *Fundamentals of Nuclear Models*. World Scientific, (2010).
- [15] J Pearson. *Nuclear Physics*. Unpublished manuscript, (2008).
- [16] B. A. Brown. *Lecture Notes in Nuclear Structure Physics*. unpublished, (2011).
- [17] D.J. Rowe. *Nuclear Collective Motion: Models and Theory*. Methuen and co. ltd., (1970).
- [18] H Oba *et al.* Continuum Hartree-Fock-Bogoliubov theory for weakly bound deformed nuclei using coordinate-space Green's function method. *Phys. Rev. C*, **80**, 024301, (2009).
- [19] S.S.M. Wong. *Introductory Nuclear Physics*. Wiley-VCH., (2004).
- [20] K. Alder and A. Winther. *Electromagnetic Excitation*. North-Holland Publishing Company, Amsterdam, 1975.

- [21] Jorrit de Boer and Jörg Eichler. *The Reorientation Effect*, pages 1–65. Springer US, Boston, MA, 1968.
- [22] D. Cline *et al.* *Gosia manual for simulation and analysis of Coulomb excitation experiments*. (2012).
- [23] C.E. Rolfs and W.S. Rodney. *Cauldrons in the Cosmos*. University of Chicargo Press, (2005).
- [24] R. Powell. *Hertzsprung–Russell Diagram*. Website, <http://www.atlasoftheuniverse.com/hr.html>, (2006).
- [25] M. Schwarzschild. *The Structure and Evolution of the Stars*. Princeton University Press, (1958).
- [26] W.A. Fowler and F. Hoyle. *Ap. J. Suppl.*, **201**, 9, (1964).
- [27] J.M. Blatt and V.F. Weisskopf. *Theoretical Nuclear Physics*. Wiley, (1952).
- [28] E. G. Adelberger *et al.* Solar fusion cross sections. II. the *pp* chain and CNO cycles. *Rev. Mod. Phys.*, **83**, 195, (2011).
- [29] W. C. Haxton and A. M. Serenelli. CN Cycle Solar Neutrinos and the Sun’s Primordial Core Metallicity. *ApJ*, **687**, 678, (2008).
- [30] K. Yamada *et al.* E1 strength of the subthreshold $\frac{3}{2}^+$ state in ^{15}O studied by Coulomb excitation. *Phys. Lett. B*, **579**, 265, (2004).
- [31] U. Schröder *et al.* Stellar reaction rate of $^{14}\text{N}(p, \gamma)^{15}\text{O}$. *Nucl. Phys. A*, **467**, 240, (1987).

- [32] N. Galinski. *Lifetime Measurement of the 6.79 MeV Excited state of ^{15}O to Help Constrain the $^{14}\text{N}(p, \gamma)^{15}\text{O}$ Reaction Rate*. PhD thesis, Simon Fraser University, (2013).
- [33] N. Paetz. *Nuclear Reaction Theory*. Wiley, (2011).
- [34] Norman K. Glendenning. *Direct Nuclear Reaction*. Academic Press Inc., 111 Fifth Avenue, New York, New York, (1983).
- [35] P. Kunz. *Documentation for use of DWUCK5*. Website, <http://spot.colorado.edu/~kunz/DWBA.html>, (2006).
- [36] G.R. Satchler. *Introduction to Nuclear Reactions*. Macmillan Education ltd, Houndmills, Basingstoke, Hampshire RG21 2XS, (1990).
- [37] C. Herlitzius. *The Doppler Shift Attenuation Method Facility: Its Design, Setup and Commissioning with the $^{32}\text{S}(^3\text{He}, ^4\text{He})^{31}\text{S}$ Reaction*. PhD thesis, Technische Universitat Munchen, (2013).
- [38] G. C. Ball, W. G. Davies, J. S. Forster, A. N. James, and D. Ward. Lifetimes of levels in ^{38}Ar . *Nuclear Physics A*, **182**, 529, (1972).
- [39] William H. Press, Brian P. Flannery, Saul A. Teukolsky, and William T. Vetterling. *Numerical Recipes in C: The Art of Scientific Computing*. Cambridge University Press, New York, NY, USA, (1988).
- [40] D. J. Griffiths. *Introduction to Electrodynamics*. Prentice Hall, Upper Saddle River, New Jersey, (1981).
- [41] G. Audi, F.G. Kondev, M. Wang, B. Pfeiffer, X. Sun, J. Blachot, and M. MacCormick. The nubase2012 evaluation of nuclear properties. *Chinese Physics C*, **36**, 1157, (2012).

- [42] James F. Ziegler, M.D. Ziegler, and J.P. Biersack. SRIM the stopping and range of ions in matter (2010). *Nuclear Instruments and Methods in Physics Research B*, **268**, 1818, (2010).
- [43] Geant Collaboration. *Geant4 User's Guide for Application Developers*. Website, (2014).

